Astronomy & Astrophysics

Dust spectral energy distributions of nearby galaxies: an insight from the *Herschel*[⋆] Reference Survey[⋆⋆]

L. Ciesla[1,2], M. Boquien[2,3], A. Boselli[2], V. Buat[2], L. Cortese[4], G. J. Bendo[5], S. Heinis[6], M. Galametz[7], S. Eales[8], M. W. L. Smith[8], M. Baes[9], S. Bianchi[10], I. de Looze[9], S. di Serego Alighieri[10], F. Galliano[11], T. M. Hughes[9], S. C. Madden[11], D. Pierini[12], A. Rémy-Ruyer[11], L. Spinoglio[13], M. Vaccari[14], S. Viaene[9], and C. Vlahakis[15]

[1] University of Crete, Department of Physics, 71003 Heraklion, Greece
e-mail: ciesla@physics.uoc.gr
[2] Aix-Marseille Université, CNRS, LAM (Laboratoire d'Astrophysique de Marseille) UMR 7326, 13388 Marseille, France
[3] Institute of Astronomy, University of Cambridge, Madingley Road, Cambridge CB3 0HA, UK
[4] Centre for Astrophysics & Supercomputing, Swinburne University of Technology, Mail H30 − PO Box 218, VIC 3122 Hawthorn, Australia
[5] UK ALMA Regional Centre Node, Jodrell Bank Centre for Astrophysics, School of Physics and Astronomy, University of Manchester, Oxford Road, Manchester M13 9PL, UK
[6] Department of Astronomy, University of Maryland, College Park MD 20742-2421, USA
[7] European Southern Observatory, Karl Schwarzschild Str. 2, 85748 Garching bei München, Germany
[8] School of Physics and Astronomy, Cardiff University, Queens Buildings The Parade, Cardiff CF24 3AA, UK
[9] Sterrenkundig Observatorium, Universiteit Gent, Krijgslaan 281 S9, 9000 Gent, Belgium
[10] INAF − Osservatorio Astrofisico di Arcetri, Largo Enrico Fermi 5, 50125 Firenze, Italy
[11] CEA/DSM/IRFU/Service d'Astrophysique, CEA, Saclay, Orme des Merisiers, Bâtiment 709, 91191 Gif-sur-Yvette, France
[12] Max-Planck-Institut für extraterrestrische Physik (MPE), Giessenbachstrasse, 85748 Garching, Germany
[13] Istituto di Fisica dello Spazio Interplanetario, INAF, via Fosso del Cavaliere 100, 00133 Roma, Italy
[14] Astrophysics Group, Physics Department, University of the Western Cape, Private Bag X17, 7535 Bellville, Cape Town, South Africa
[15] Joint ALMA Observatory/European Southern Observatory, Alonso de Córdova 3107, Casilla 19001 Vitacura, Santiago, Chile

ABSTRACT

Although it accounts only for a small fraction of the baryonic mass, dust has a profound impact on the physical processes at play in galaxies. Thus, to understand the evolution of galaxies, it is essential not only to characterize dust properties per se, but also in relation to global galaxy properties. To do so, we derive the dust properties of galaxies in a volume limited, K-band selected sample, the *Herschel* Reference Survey (HRS).

We gather infrared photometric data from $8\,\mu$m to $500\,\mu$m from *Spitzer*, WISE, IRAS, and *Herschel* for all of the HRS galaxies. Draine & Li (2007, ApJ, 663, 866) models are fit to the data from which the stellar contribution has been carefully removed. We find that our photometric coverage is sufficient to constrain all of the parameters of the Draine & Li models and that a strong constraint on the $20-60\,\mu$m range is mandatory to estimate the relative contribution of the photo-dissociation regions to the infrared spectral energy distribution (SED). The SED models tend to systematically underestimate the observed $500\,\mu$m flux densities, especially for low-mass systems. We provide the output parameters for all of the galaxies, i.e., the minimum intensity of the interstellar radiation field, the fraction of polycyclic aromatic hydrocarbon (PAH), the relative contribution of PDR and evolved stellar population to the dust heating, the dust mass, and the infrared luminosity. For a subsample of gas-rich galaxies, we analyze the relations between these parameters and the main integrated properties of galaxies, such as stellar mass, star formation rate, infrared luminosity, metallicity, Hα and H-band surface brightness, and the far-ultraviolet attenuation. A good correlation between the fraction of PAH and the metallicity is found, implying a weakening of the PAH emission in galaxies with low metallicities and, thus, low stellar masses. The intensity of the diffuse interstellar radiation field and the H-band and Hα surface brightnesses are correlated, suggesting that the diffuse dust component is heated by both the young stars in star-forming regions and the diffuse evolved population.

We use these results to provide a new set of infrared templates calibrated with *Herschel* observations on nearby galaxies and a mean SED template to provide the $z = 0$ reference for cosmological studies. For the same purpose, we place our sample on the $SFR-M_*$ diagram. The templates are compared to the most popular infrared SED libraries, enlightening a large discrepancy between all of them in the $20-100\,\mu$m range.

Key words. galaxies: ISM – infrared: galaxies – dust, extinction

---

1. Introduction

In the interstellar medium (ISM), dust holds a major role: a) it acts as a catalyst in the transformation of atomic hydrogen into molecular hydrogen from which stars form (Wolfire et al. 1995);

b) it allows gas to cool and condense to form new stars by absorbing the ultraviolet (UV) emission of surrounding young stars (Draine 1978; Dwek 1986; Hollenbach & Tielens 1997); and c) it reemits the absorbed energy in the infrared domain (IR), where the thermal emission by dust grains dominates the spectral energy distribution (SED) of galaxies between ≈ 10 and $1000\,\mu m$. Dust is thus an important tracer of star formation activity. Formed by the aggregation of metals injected into the ISM by stars through stellar winds and supernovae explosions, its composition still remains uncertain. The most popular models assume that dust consists of a mixture of silicate and graphite grains (Mathis et al. 1977; Draine & Lee 1984; Kim et al. 1994), and are extended by adding the contribution of the polycyclic aromatic hydrocarbons (PAH), producing the broad spectral features seen in the mid-IR (MIR), such as in models by Siebenmorgen & Kruegel (1992), Li & Draine (2001), Weingartner & Draine (2001), and Draine & Li (2007).

Because of the important role of dust in the ISM and its tight link with the other components of galaxies, the study of dust emission is mandatory to have a better understanding of all of the processes at play. IRAS (Infrared Astronomical Satellite, Neugebauer et al. 1984), COBE (Cosmic Background Explorer, 1989), ISO (Infrared Space Observatory, Kessler et al. 1996), *Spitzer* (Werner et al. 2004), and AKARI (Murakami 2008) allowed us to study dust emission up to $240\,\mu m$. While these telescopes sampled well the dust properties from the MIR to around the peak of the dust SED, going to longer submillimeter (submm) wavelengths, well beyond the peak, is crucial for modeling the distribution of the dust size, temperature, and composition. In this way, the inventory of the bulk of the dust mass in galaxies, manifested in the submm, is also not missed (Devereux & Young 1990; Gordon et al. 2010). Ground-based facilities, such as SCUBA (Submillimeter Common-User Bolometer Array, Holland et al. 1999), provide us with submm data, but observations of large samples of normal galaxies are still prohibitive due to the long integration times needed for these instruments, which suffer from limited sensitivity.. Furthermore, a large part of the far-IR (FIR) and submm domains are not accessible from the ground. The *Herschel* Space Observatory (Pilbratt et al. 2010) opened a new window on the FIR/submm spectral domain (55 to $672\,\mu m$), allowing us to probe the cold dust component in a large number of nearby objects.

We now have a global view of the emission from all of thermal dust components, covering a broad range of temperatures and the different heating mechanisms for these components. Before *Herschel*, it was already evident that a significant part of the IR SEDs of galaxies potentially includes cold (17 to 20 K) diffuse cirrus components heated by the diffuse interstellar radiation field from the total stellar population, and not just the light from star forming regions (e.g., Helou 1986; Xu & Helou 1996; Li & Draine 2002; Boselli et al. 2004; Komugi et al. 2011; Totani et al. 2011). However, the emission for these colder components often appears intermixed with emission from warmer dust heated by star forming regions at λ lower than $\approx 240\,\mu m$, and in many cases, the emission is poorly constrained. Multiple authors using *Herschel*, including Bendo et al. (2010, 2012b), Boquien et al. (2011), Groves et al. (2012), and Smith et al. (2012b), have used comparisons of FIR colors to NIR emission from the evolved stellar population to demonstrate that the cirrus component is often the primary source of $>250\,\mu m$ emission and also contributes at shorter wavelengths.

Understanding the heating processes of the dust is of paramount importance to provide physical models than can reproduce the FIR/submm SED of galaxies. Multiwavelength radiative transfer modeling of galaxies is a powerful tool to analyze the properties of dust in galaxies in a self-consistent way (e.g., Xilouris et al. 1999; Popescu et al. 2000, 2011; de Looze et al. 2012b; Alton et al. 2004; Bianchi 2008; Baes et al. 2010; MacLachlan et al. 2011; de Looze et al. 2012a). However, assumptions regarding the geometry of the dust need to be made, and these codes require large computational resources, especially for a large sample of galaxies. Therefore, models, as well as empirical templates, are widely used to extract information about galaxies from their IR SED (Chary & Elbaz 2001; Dale & Helou 2002; Boselli et al. 2003a; Draine & Li 2007, hereafter CE01, DH02, B03, and DL07). The pre-*Herschel* empirical libraries of templates (CE01, DH02) were calibrated on FIR observations and detections of galaxies up to $\approx 200\,\mu m$, and were constructed from local normal and IR luminous star forming galaxies. Recent studies, making use of the new *Herschel* data, provided new IR templates for low- and high-redshift objects (Elbaz et al. 2011; Smith et al. 2012a; Magdis et al. 2012). However, there is a lack of templates representative of the broad variety of nearby normal galaxies, reference of the $z = 0$ Universe.

The *Herschel* Reference Survey (HRS, Boselli et al. 2010b) is composed of 322 nearby galaxies spanning the entire range of morphological types and environment. The aim of this volume-limited, K-band selected sample is to investigate the dust properties of galaxies for which a wealth of ancillary data are available, both photometric (from UV to radio, Bendo et al. 2012a; Boselli et al. 2010b, 2011; Ciesla et al. 2012; Cortese et al. 2012b, 2014) as well as spectroscopic (Boselli et al. 2013, 2014; Hughes et al. 2013). With this set of data, the HRS is one of the best samples to study the dust properties of nearby galaxies versus parameters such as the stellar mass, the metallicity, the star formation rate (SFR), etc., giving us a better understanding of its role in the ISM and the interplay with the stellar radiation field.

In this work, we derive the physical properties of the dust by fitting the integrated IR SED of the HRS galaxies with the models of DL07. Although these models are physical, they have been mainly tested on FIR data (Draine et al. 2007), and recently, using *Herschel* data (Dale et al. 2012; Aniano et al. 2012; Draine et al. 2014). We thus discuss the ability of these models to reproduce the submm observations of our galaxies. For a subsample of gas-rich galaxies, we then investigate the relations between the derived output parameters and the integrated galaxy properties (stellar mass, SFR, birthrate parameter, metallicity, FUV attenuation, Hα surface brightness, and H-band effective surface brightness). Based on this analysis, we derive a set of SED templates, binned according to those parameters that better characterize the shapes of the SED, and compare them with libraries available in the literature.

This paper is organized as follows: in Sect. 2, we describe the HRS and define a gas-rich subsample on which we will focus our analysis. The ancillary data associated with this subsample are presented in Sect. 3. We present the procedure used to perform the fitting, analyze our ability to constrain the models with the data and present the results in Sect. 4. For the gas-rich galaxy subsample, we outline the most interesting relations between the output from the fitting and galaxy parameters in Sect. 5. The derivation and discussion of the new IR library is presented in Sect. 6. In Appendix A, we present the MIR photometry of all of the HRS galaxies at 8, 12, and $22\,\mu m$, which are important constraints for the SED modeling. In Appendix B, we explain the method derived to remove the stellar contribution from our data and provide new coefficients useful for future works. For completeness, in Appendix C, we give the output parameters

from the SED fitting for the galaxies that are not discussed in the main part of this work (early-type galaxies and HI-deficient galaxies). Finally, all of the relations between the output of DL07 models and the properties of the gas-rich sample are presented and discussed in Appendix D.

2. Sample

The HRS galaxies are selected according to three criteria fully described in Boselli et al. (2010b). The HRS is a volume limited sample composed of galaxies lying at a distance between 15 and 25 Mpc. The galaxies are then selected according to their K-band magnitude, the luminosity of which is a proxy for the total stellar mass (Gavazzi et al. 1996). Based on optical extinction studies and FIR observations at wavelengths shorter than $200\,\mu$m, we expect late-type galaxies to have a larger content of dust than early-types (Sauvage & Thuan 1994). Thus, two different K_{mag} limits have been adopted: $K_{\mathrm{mag}} \leq 12$ for late-types and $K_{\mathrm{mag}} \leq 8.7$ for early-types (in Vega magnitudes). Finally, to limit the contamination from Galactic cirrus, galaxies are selected at high Galactic latitude ($b > +55$ deg) and in low Galactic extinction regions ($A_B < 0.2$, Schlegel et al. 1998). The final sample contains 322[1] galaxies, among which are 62 early-types and 260 late-types. The HRS covers all morphological types and contains field galaxies as well as objects in high-density regions such as the Virgo cluster. We use the morphological classification presented in Cortese et al. (2012a).

Even if we present the NIR photometry and perform the SED fitting of all of the HRS galaxies, the paper focuses on the study of a subsample of 146 gas-rich galaxies. From the whole HRS sample, we remove early-type galaxies (E-S0-S0/Sa) from the analysis as the dust properties and the dust heating sources of elliptical and lenticular galaxies are different from late-type galaxies (e.g., Boselli et al. 2010a; Smith et al. 2012b). Indeed, the relative contribution of X-ray heating, stochastic heating, heating from fast electrons in the hot gas, and the size-distribution of dust grains in these environments with low-density ISM might differ from that of late-types and thus need further investigation (Wolfire et al. 1995). Furthermore, only 32% of the elliptical galaxies and 60% of the lenticulars are detected at $250\,\mu$m (Ciesla et al. 2012), yielding an incomplete photometric coverage of the IR-submm domain. Finally, some of the physical properties used in this work (birthrate parameter, Hα surface brightness, and metallicity) are not available for all of the early-type galaxies. Furthermore, a number of late-type galaxies of the HRS lie in the very dense environment of the Virgo cluster. These galaxies have their gas content stripped by the environment (Boselli & Gavazzi 2006). *Herschel* observations have recently shown that the dust component of HI-deficient[2] galaxies is also affected by the cluster environment (Cortese et al. 2010, 2012b). In the following, we define as "gas-rich" galaxies those with HI$-$def ≤ 0.4, and "HI-deficient" those with HI$-$def > 0.4, to be consistent with Boselli et al. (2012). We decide to not consider HI-deficient galaxies in our analysis to remove the effects of the environment as a free parameter that could bias the interpretation of the results. The study of the ef-

Table 1. Completeness of the photometric coverage of the 146 gas-rich galaxies.

Band	$\lambda\,(\mu$m)	Mean error (%)	Number of galaxies
Spitzer/IRAC	8	15	56
WISE	12	6	146
WISE	22	13	141
Spitzer/MIPS	24	4	68
IRAS	60	15	128
Spitzer/MIPS	70	10	47
Herschel/PACS	100	16	146
Herschel/PACS	160	12	146
Herschel/SPIRE	250	6	146
Herschel/SPIRE	350	8	146
Herschel/SPIRE	500	11	146

Notes. Only detections are considered.

fect of the environment on the dust properties of galaxies will be presented in a future work.

The main part of this paper is focused on the data, the SED fitting, and the analysis of the gas-rich late-type sample. The NIR photometry of all of the HRS galaxies, and the output parameters from the SED fitting obtained for the early-type galaxies and the HI-deficient galaxies are presented in Appendix A and Appendix C, respectively.

3. Data

In order to compute the IR SEDs of the HRS galaxies, we use data from 8 to $500\,\mu$m performing the photometry on *Spitzer*/IRAC and WISE images and using measurements available in the literature from *Spitzer*/MIPS, *Herschel*/PACS, *Herschel*/SPIRE, and IRAS. These data are publicly available through the Hedam database[3].

3.1. Mid-infrared: Spitzer/IRAC and WISE

For the purpose of this work, we perform the photometry of 56 out of the 146 galaxies of our subsample for which observations at $8\,\mu$m from *Spitzer*/IRAC were available in the *Spitzer* archive. The procedure is presented in Appendix A and the flux densities and associated errors are given in Table A.2. Our procedure to estimate the errors associated with the $8\,\mu$m data, based on Boselli et al. (2003a), results in a mean error of 15% (see Table 1). We also perform the WISE photometry of the gas-rich galaxies at 12 and $22\,\mu$m. As for the IRAC 8 um data, Appendix A describes the procedure we used, and gives the resulting flux densities and their associated errors. The mean errors associated with the $12\,\mu$m and the $22\,\mu$m flux densities are 6% and 13%, respectively. Comparisons between our measurements and results from the literature, as presented in Appendix A, are in good agreement. The IRAS $12\,\mu$m flux densities are available only for 15% of our galaxies, whereas all of our subsample galaxies have a $12\,\mu$m flux density from WISE. To have a homogeneous set of data, we use the WISE $12\,\mu$m flux densities.

3.2. Far-infrared: Spitzer/MIPS, IRAS, and Herschel/PACS

The reduction and photometry of MIPS data are fully described in Bendo et al. (2012a). Flux densities of 68 gas-rich galaxies are available at $24\,\mu$m, and 47 are available at $70\,\mu$m. For most of the

---

[1] With respect to the original sample given in Boselli et al. (2010b), the galaxy HRS 228 is removed from the complete sample because its updated redshift on NED indicates it as a background object.

[2] The HI-deficiency, HI$-$def, is defined as the difference, in logarithmic scale, between the HI mass expected from an isolated galaxy with the same morphological type and optical diameter and the observed HI mass (Haynes et al. 1984).

[3] http://hedam.lam.fr/HRS/

galaxies, aperture photometry was performed using an elliptical region with major and minor axes of 1.5 times the axis sizes of the D_{25} isophotes given by de Vaucouleurs et al. (1991). The same aperture was used in the two bands. In the case of HRS 20-NGC 3395 and its companion NGC 3396, the flux densities provided correspond to one of the pair as it is hard to disentangle the emission from the two galaxies within a pair. Thus, we do not use these measurements. The error calculation takes into account the calibration error, 4 and 10% at 24 and 70 μm (Engelbracht et al. 2007; Gordon et al. 2007), respectively, the uncertainty based on the error map, and the background noise. The three are added in quadrature. We should note that a transcription error was made in Bendo et al. (2012b) for the flux density of HRS 142. Its flux density at 70 μm is 8200 mJy instead of 1237 mJy. Despite the incompleteness of the MIPS 24 μm data, we choose to use them, when available, instead of the WISE 22 μm. This choice is due to the poor quality of some WISE 22 μm images resulting in a mean error of 13% in this band when the mean error of MIPS 24 μm is 4% only. The IRAS 25 μm data are also available for only a small part of our subsample (15%), we thus decided to not use these measurements to keep a homogeneous set of data from one galaxy to another.

Because of the incompleteness at 70 μm, we also use, when available, the 60 μm measurements from IRAS presented in Boselli et al. (2010b). The IRAS 60 μm flux densities of 128 galaxies of the subsample, with a typical uncertainty of 15%, are provided by multiple references in the literature and collected on NED: Sanders et al. (2003); Moshir & et al. (1990); Thuan & Sauvage (1992); Soifer et al. (1989); Young et al. (1996).

All of the gas-rich galaxies are detected by PACS at 100 and 160 μm, respectively (Cortese et al. 2014). They performed aperture photometry following the method used by Ciesla et al. (2012) to build the HRS SPIRE catalog (see Sect. 3.3). The apertures used to extract the fluxes are identical to those used for the SPIRE photometry. However, a refinement of the photometric aperture has been applied to some of the objects for various reasons (some galaxies were unresolved in SPIRE bands and resolved in PACS bands, some PACS maps were too small to encompass the SPIRE aperture, or the FIR emission of the galaxy was much less extended than the SPIRE aperture). Errors were estimated following the method described in Roussel (2013). The mean errors are 16% and 12% at 100 and 160 μm, respectively. The data reduction and the integrated photometry are described in Cortese et al. (2014).

3.3. Submillimetre: Herschel/SPIRE

In the SPIRE bands, all of the galaxies of the subsample are detected at 250, 350, and 500 μm, respectively. The SPIRE photometry is fully described in Ciesla et al. (2012). In summary, aperture photometry was performed in elliptical regions for extended galaxies. All apertures have been chosen to encompass the emission and to minimize the contamination of background sources. The stochastic error takes into account the instrumental uncertainty, the confusion uncertainty (due to the presence of faint background sources), and the background uncertainty (due to large scale structure, such as cirrus), with all three added in quadrature. Flux densities of point-like sources have been measured using PSF fitting on timeline data (Bendo et al. 2013). We take the last updates into account by applying the calibration corrections (1.0253, 1.0250, and 1.0125 at 250, 350,

and 500 μm, respectively) and the new beam areas[4] of 450, 795 and 1665 arcsec^2 at 250, 350, and 500 μm, respectively. We do not take the variations of the beam sizes into account, depending on the shape of the SED, as they are generally within the SPIRE errors. The result of these updates lowers the flux densities presented in Ciesla et al. (2012) by $\approx$5%. The mean errors are 6%, 8% and 11% at 250, 350, and 500 μm, respectively.

The photometric completeness of the gas-rich sample of galaxies is presented in Table 1. Upper limits are not taken into account in our fitting procedure and will thus correspond to an absence of data in Table 1.

4. SED fitting with the Draine & Li (2007) models

4.1. Draine & Li (2007) models

DL07 modeled the dust with a mixture of astronomical amorphous silicate and carbonaceous grains with the size distribution observed in the Milky Way (Weingartner & Draine 2001). Models of the LMC and SMC grain size distribution are also available.

The bulk of the dust present in the diffuse ISM is heated by a large number of stars responsible for the diffuse radiation. However, another part of the dust is located in regions close to very luminous O and B stars, in photodissociation regions (PDR). In PDRs, the light coming from the young stars is heating the dust and is much more intense than the emission coming from the old stars responsible for the diffuse radiation. In DL07 models, the relative dust mass fraction heated by each source, the diffuse component and the PDRs, is given by the γ parameter. Thus, the fraction $(1 - \gamma)$ of the total dust mass is heated by $U = U_{min}$, where U is the intensity of the interstellar radiation field (ISRF) and U_{min} is the intensity of the diffuse ISRF, both normalized to the intensity of the Milky Way ISRF.

Recently, Aniano et al. (2012) linked the temperature of the cold dust component to the U_{min} parameter by approximating the DL07 SED with a blackbody multiplied by a power-law opacity and obtained $T_d \approx 20\ U_{min}^{0.15}$ K. The fraction γ of the total dust mass is exposed to a range of stellar intensities following a power-law distribution from U_{min} to U_{max} with $dM/dU \propto U^{-2}$. From these three parameters, we can compute $\langle U \rangle$, the mean intensity of the ISRF, from Eq. (17) of Draine et al. (2007). A last parameter aims at characterizing the emission due to the PAH. Their abundance is quantified with the parameter q_{PAH}, which corresponds to the fraction of the total grain mass contributed by PAH containing less than 10^3 C atoms. Each model depends on the set of parameters $\{dust composition, q_{PAH}, \gamma, U_{min}, and U_{max}\}$. Finally, the dust mass is also a free parameter determined from the normalization of the model to the observations. Following the recommendations of Draine et al. (2007), we use only the Milky Way dust type and fix $U_{max} = 10^6$. Thus, the free parameters of the fit are q_{PAH}, γ, and U_{min}. The normalization of the model to the data provides us with the dust mass M_{dust}, and the integration of the model between 8 and 1000 μm gives us the infrared luminosity L_{IR}.

4.2. Fitting procedure

As DL07 model the emission of the dust from 1 μm to 1 cm, we need to remove the stellar emission that contributes to the MIR data to have only the emission from the dust. In Appendix B, we

---

[4] See http://herschel.esac.esa.int/twiki/bin/view/Public/SpirePhotometerBeamProfileAnalysis

Table 2. Ranges of parameter used in our fitting procedure.

Parameter	Values
U_{min}	from 0.10 to 25
U_{max}	10^6
q_{PAH} (%)	from 0.47 to 4.58
γ (%)	100 logarithmically-spaced values from 0.1% to 100%
L_{IR}	Integration of the model between 8 and $1000\,\mu m$
M_{dust}	Normalization of the model to the data

describe the method we use to remove the stellar contribution and provide morphological type dependent coefficients normalized to several NIR bands, and determined using the CIGALE[5] code (Code Investigating GALaxy Emission, Noll et al. 2009). The code computes modeled galaxy SEDs by using stellar population models from Maraston (2005), which are convolved with a given star formation history (SFH). We use an exponentially decreasing SFH, which we present in Appendix B. The coefficients ($S_{\nu,stellar}/S_\nu$) applied to the MIR photometry of the sample are 0.093, 0.075, 0.016, and 0.017 at 8, 12, 22, and $24\,\mu m$, respectively (see Appendix B).

The DL07 models are integrated into the filters of the corresponding photometric bands, and these modeled flux densities are compared to the observations. The ranges allowed for each parameter are presented in Table 2. For galaxies that do not have any MIPS $24\,\mu m$ observations, the fit is performed using the WISE $22\,\mu m$ flux densities as explained in Sect. 3.2.

We use a χ^2 minimization method to fit our data with the models of DL07. For each galaxy, we compute the χ^2 corresponding to every model using the equation:

$$\chi^2(a_1,...,a_i,...,a_N) = \sum_{i=1}^{M} \left[\frac{y_i - \alpha y(x_i, a_1,...,a_i,...,a_N)}{\sigma_i} \right]^2, \quad (1)$$

and the reduced χ^2 as:

$$\chi^2_{red} = \frac{\chi^2}{M-N} \quad (2)$$

where y is the model, a_i are the parameters values of this model, x_i correspond to the observations, and σ_i the errors attributed to these observations. The number of parameters is N and M the number of observed data. We obtain the normalization factor through the following equation:

$$\alpha = \frac{\sum_{i=1}^{N} y_i \times y(x_i, a_1,...,a_i,...,a_M)/\sigma_i^2}{\sum_{i=1}^{N} y(x_i, a_1,...,a_i,...,a_M)^2/\sigma_i^2}. \quad (3)$$

As the reduced χ^2 (χ^2_{red}) is calculated for each value of a parameter, we can build the probability distribution function (PDF) of this parameter. For each value of a discrete parameter, we select the corresponding minimum χ^2_{red}. Thus, we have the distribution of the minimum χ^2_{red} associated with the set of values of the parameter. From this distribution, we obtain the estimated value of the parameter, as the mean value of this distribution, and the associated error as its standard deviation, proceeding as described in Noll et al. (2009). For parameters with a large range of values, we compute bins and take the minimum χ^2_{red} corresponding to each bin. Then we build the distribution. In the following discussions, we will refer to the "best" parameter as the parameter obtained directly from the model providing the minimum χ^2_{red},

and to the "estimated" parameter as the parameter derived from the distribution of χ^2_{red}.

This SED fitting procedure is applied to all of the galaxies of the HRS. However, from now on, this work only focuses on the gas-rich galaxy subsample, and the results for the other galaxies (early-type, and late-type deficient galaxies) are presented in Appendix C.

4.3. Mock catalogs

The χ^2 fitting described in the previous section provides us with a best-fit model for each galaxy. However, we need to know if the output parameters obtained from these models are reliable, i.e., if the data we have allow us to constrain these parameters. To do so, we create mock catalogs following the procedure outlined in Giovannoli et al. (2011). We first run our χ^2 procedure on our sample to obtain the best-fitting model and the corresponding parameters for each galaxy. The resulting best SEDs are integrated in the filters adding an error randomly distributed according to a Gaussian curve. The σ of the Gaussian curve is chosen to be the median value of the error for each band. We now have a mock catalog in which the exact values of the parameters are known. As a final step, we run our fitting procedure on this mock catalog and compare the input "best" values of the parameters to the output "estimated" values. This test allows us to evaluate the ability to constrain a parameter with the photometric coverage available for our galaxies.

We note that some galaxies of our sample are lacking $8\,\mu m$, $22-24$ or $60-70\,\mu m$ measurements. To estimate the impact of the lack of data on the estimation of the parameters, we build several mock catalogs using different combinations of bands to understand the importance of every photometric band. Indeed, all of the galaxies in our sample were not observed in every band. To understand the effect of the inhomogeneity of the photometric coverage of our sample and to evaluate the impact of submm data on constraining the models, we also build a mock catalog omitting SPIRE data. We present the results from the mock catalogs for U_{min}, γ, q_{PAH}, $\log L_{IR}$, and $\log M_{dust}$ in Fig. 1 and in Fig. 2. For each parameter, we show the case where the photometric coverage is complete (Fig. 1), where there is no $8\,\mu m$ flux density, in the absence of $22-24\,\mu m$ data, the case where there are no $60-70\,\mu m$ data and, finally, in the absence of SPIRE data (Fig. 2). For each panel of Figs. 1 and 2, we provide the best linear fit, the Spearman correlation coefficient and the median value and standard deviation of the estimated to true value ratio in Table 3. We separate galaxies having a $24\,\mu m$ measurement from *Spitzer*/MIPS (blue filled points) from galaxies having a $22\,\mu m$ measurement from WISE (red empty points). This separation allows us to see the impact of the precision of the photometry on the determination of the parameters, especially for γ, as we will discuss.

A complete photometric coverage from 12 to $500\,\mu m$ is sufficient to constrain the U_{min} parameter, with a mean ratio between the estimated value to the true one of 1.07 ± 0.20 (Table 3). The absence of $8\,\mu m$ measurement does not affect the estimation of U_{min}. The lack of data at $22-24\,\mu m$ yields an underestimation of the parameter U_{min} of $\approx 14\%$, whereas the lack of $60-70\,\mu m$ yields an overestimation of 18%. The worst case is when no SPIRE data is available with an overestimation of 25%, showing the importance of submm data to properly constrain U_{min}. Indeed, as the U_{min} parameter directly probes the position of the IR peak, constraints from both parts of the peak are needed for a good estimate.
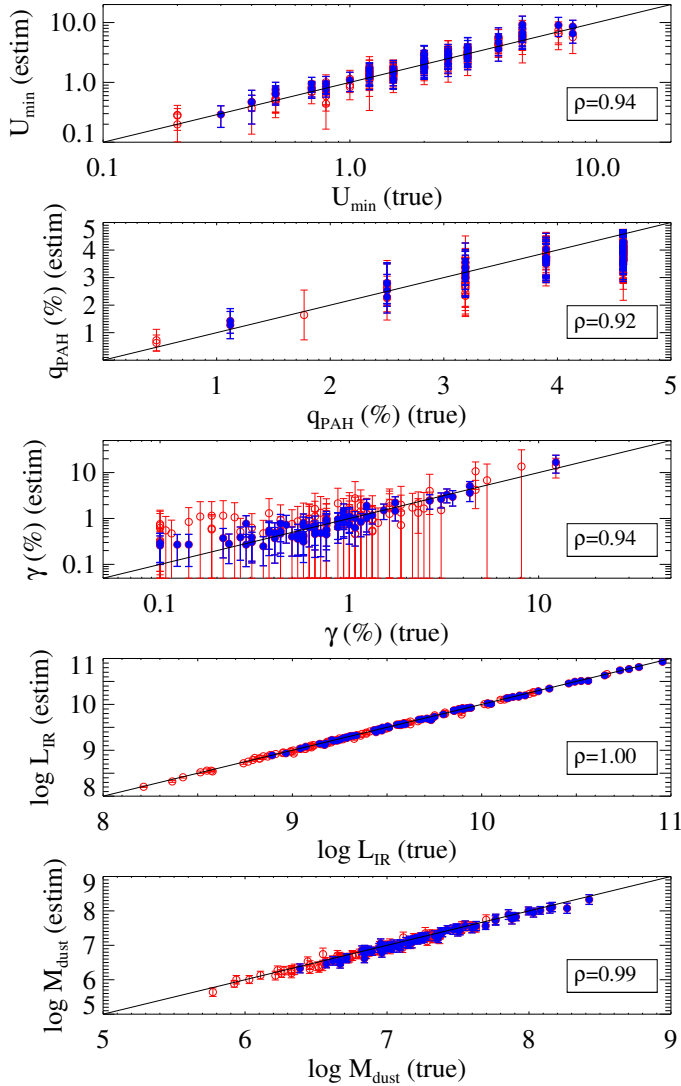
Fig. 1. Comparison between the true values of the parameters, *from top to bottom*: U_{min}, q_{PAH}, γ, $\log L_{IR}$, $\log M_{dust}$, and the mock catalogs parameters values estimated from the PDF. Blue filled dots correspond to galaxies having a $24\,\mu m$ measurement and red empty dots are galaxies with a $22\,\mu m$ measurement. The solid black line is the 1:1 relationship. The DL07 parameters are constrained, but γ needs the $24\,\mu m$ from MIPS to be properly estimated.

Considering the γ parameter, the median ratio between the estimated and true values of the parameters is 1.18. However, this median drops to 1.01 when values of γ are larger than 0.5%. With our photometric coverage, we tend to overestimate the low values of γ. The importance of the 22 and $24\,\mu m$ measurements and the associated errors is clear. When all bands are available, the precision of the MIPS 24 photometry provides good constraints on the estimate of γ, especially for values above a few percent. With a mean error of 13% on the WISE 22 photometry, there is a good correlation for values of γ above a few percent, but the errors on the estimated parameters are very large, indicating a large PDF linked to the estimation of γ. The impact of this $22-24\,\mu m$ range is confirmed in the panel where these two bands are removed, the median value of the estimated to true values ratio is 3.77 ± 6.43, and the relation is flat. When the $22-24\,\mu m$ bands are removed, the estimated gamma derived from the model is rather constant in whatever galaxy we model. The absence of $60-70\,\mu m$ or SPIRE data does not have a large

impact on the estimation of γ, but yields to a slightly more dispersed relation.

The $8\,\mu m$ band directly probes the PAH emission: in the absence of the IRAC 8 band, the Spearman correlation coefficient between the estimated q_{PAH} and the true q_{PAH} decreases from 0.92 to 0.88 and the standard deviation of the estimated to true values ratio increases from 0.11 to 0.20. Interestingly, the absence of $22-24\,\mu m$ data provides a median underestimation of the parameter of 23%, showing the importance of constraining the continuum to estimate the q_{PAH} parameter with our photometric coverage. From Fig. 1, we conclude that the presence of the $12-22-24\,\mu m$ data is sufficient to have a relatively good constraint on the fraction of PAH, q_{PAH}, provided by the DL07 models. For our sample of galaxies, the $8\,\mu m$ measurement is thus not mandatory to study q_{PAH}.

The L_{IR} and the M_{dust} are well constrained in all configurations. Even without the SPIRE bands, the M_{dust} is well constrained despite a slightly larger scatter. This constraint on M_{dust} comes from the fact that β is fixed in DL07 (to ≈ 2.06) and, as this parameter is provided by the normalization of the models to the observed data, observations at $160\,\mu m$ seem to be sufficient to constrain M_{dust}.

All the parameters are constrained with the combination of IR bands available for this study, except γ for which MIPS $24\,\mu m$ measurement is mandatory. Therefore, the discussion of γ and $\langle U \rangle$ (as $\langle U \rangle$ depends on γ) will be restricted to the galaxies having a $24\,\mu m$ flux density. However, we note that this analysis from mocks allows us only to characterize our ability to constrain the parameters of DL07 given our photometric coverage.

4.4. Results of the fits

Table 4 presents the results of the fit for the 146 galaxies: the output parameters from DL07 models, L_{IR} and M_{dust}.

4.4.1. Assessment of the quality of the fit

To have a global look at the quality of the fits, we show in Fig. 3 the ratio between the observed and the modeled flux densities for each photometric band versus the stellar mass (the calculation of M_* is described in Sect. 5), as the HRS was selected in K-band, which is a proxy for stellar mass. For each galaxy, the values predicted by the models are obtained by integrating the best SEDs resulting from the fits into the filters of every band. Points are color coded according to the χ^2_{red} value associated with the fit.

The analysis of Fig. 3 shows that:

– Fits of galaxies with $\log(M_*/M_\odot) < 10$ have a better χ^2_{red} than higher mass systems for which χ^2_{red} can reach up to 20.
– At $8\,\mu m$, the models seem to systematically overpredict the observed flux density by $\approx 7\%$ from low- to high-mass systems.
– At $12\,\mu m$, there is good agreement between both observed and modeled flux densities up to $\log(M_*/M_\odot) \approx 10$. For higher mass galaxies, the models underpredict the observed flux densities.
– There is a systematic overestimation of the $22-24\,\mu m$ by the models of 10% at $22\,\mu m$ and 5% at $24\,\mu m$. For the MIPS $24\,\mu m$, this overestimation increases with the stellar mass and can reach up to 20%. Despite this trend, with a mean ratio of 0.95 and a small dispersion 0.05, there is a good
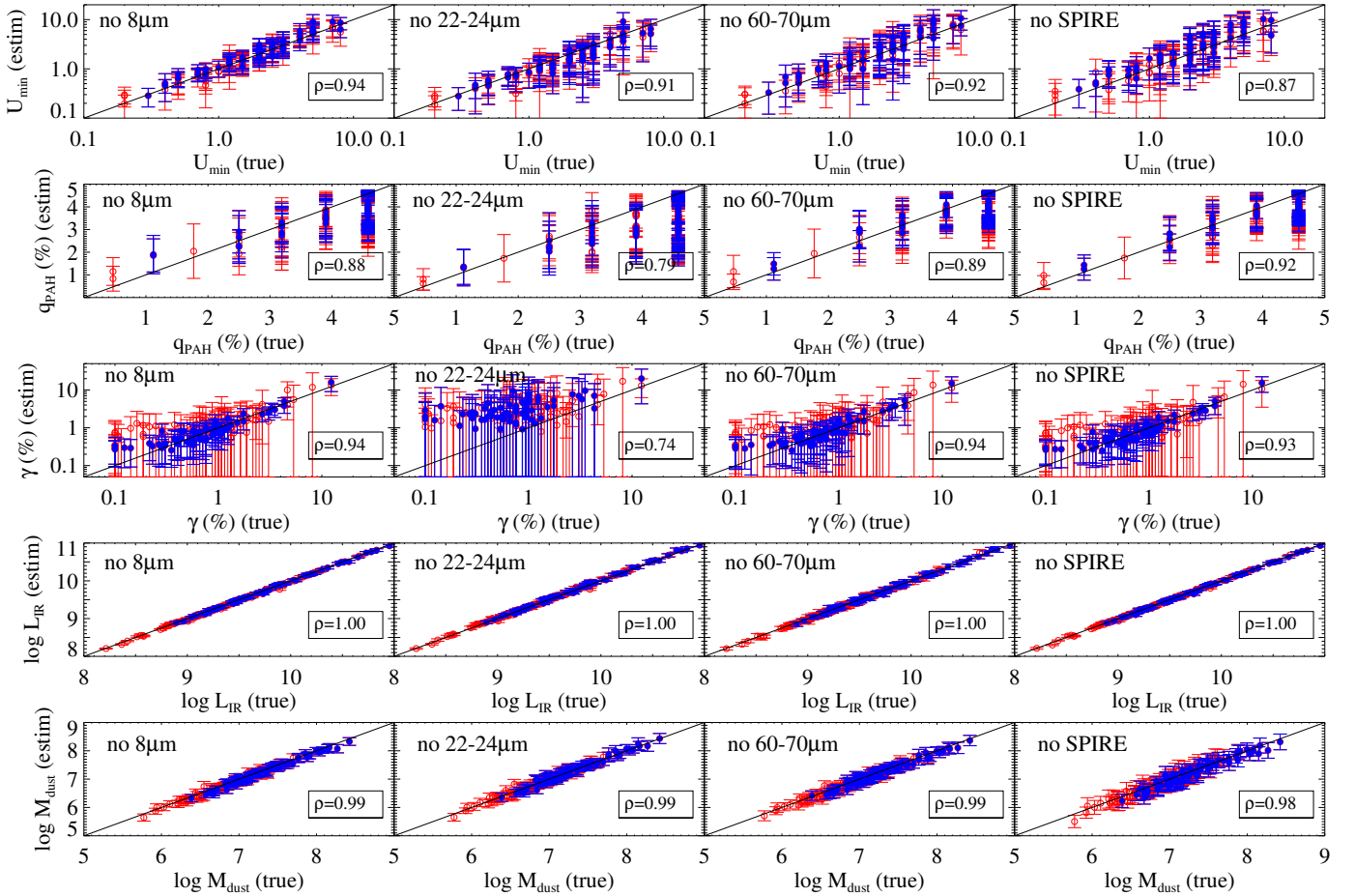
Fig. 2. Comparison between the true values of the parameters (*from top to bottom*) U_{min}, q_{PAH}, γ, $\log L_{IR}$, $\log M_{dust}$, and the mock catalogs parameters values estimated from the PDF. The different panels correspond to different observed band combinations. For each parameter and *from left to right*: all bands but the 8 μm, all bands but the 22 and 24 μm, all bands but the 60 and 70 μm, and all bands but SPIRE. Blue filled dots correspond to galaxies having a 24 μm measurement and red empty dots are galaxies with a 22 μm measurement. The solid black line is the 1:1 relationship. DL07 parameters are constrained, but γ needs the 24 μm from MIPS to be properly estimated.

agreement between the models and the observations at this wavelength.

– The 60 μm ratio is very dispersed, and the mean value of 0.96 is not representative as there is a clear trend with the stellar mass. Models underpredict the 60 μm observations of low-mass systems and overpredict them for high-mass objects. However, the mean photometric error of 15% is one of the largest of all bands and is not a strong constraint for the fit. The 70 μm observed to modeled flux density ratios follow the same trend with the stellar mass than the 60 μm, but with a smaller dispersion ($\sigma = 0.18$).

– At 100 and 160 μm, despite a large dispersion, there is a relatively good agreement between observations and models with a slight overprediction at 100 μm and underprediction at 160 μm of $\approx$3%.

– The 250 and 350 μm SPIRE bands are in average well fitted by the models, even if the 250 μm is slightly overestimated for the whole sample. A small trend is seen at 350 μm, the flux densities from the models tend to be lower than the observations for low-mass galaxies.

– At 500 μm, this trend becomes stronger. The 500 μm observations seem to be underpredicted by the models, especially for low-mass systems. Indeed, for galaxies with $\log(M_*/M_\odot) \approx 10$, there is a clear underprediction of the

500 μm data, up to $\approx$40%, that increases when the stellar mass decreases.

A submm excess, such as the one observed at 500 μm, was already noticed by previous works in low-metallicity systems (e.g., Reach et al. 1995; Galliano et al. 2003, 2005, 2011; Bot et al. 2010; Gordon et al. 2010; Boselli et al. 2010b; Galametz et al. 2011; Boselli et al. 2012). Different hypotheses have been proposed to explain this excess. A very cold dust component was proposed by Galliano et al. (2003, 2005), showing that it would need to lie in a small number of dense parsec scale clumps, but Galliano et al. (2011) showed that this hypothesis was not verified in the LMC, where they had the spatial resolution to test it. Meny et al. (2007) proposed a solid-state-based, temperature-dependent emissivity increases at long wavelength, in amorphous materials. Finally, Draine & Hensley (2012) argued that this excess could be due to ferromagnetic free-flying small grains or ferromagnetic inclusions in normal grains. Changing the FIR β slope can make the excess diminish but it is not sufficient (Galliano et al. 2011). Boselli et al. (2012) noticed that a modified blackbody with an emissivity index of $\beta = 1.5$ better represents the SPIRE data of the HRS galaxies than the DL07 models, which submm slope can be approximated by $\beta \approx 2$. However, they outlined that $\beta = 2$ is possible

Table 3. Statistics from the relations of the mock catalogs (Fig. 1).

Parameter	Bands	Linear fit: $A + Bx$		Spearman coef.	Stat of X_{est}/X_{true}	
		A	B	ρ	median	σ
U_{min}	all	0.03	1.07	0.94	1.07	0.20
	no 8 μm	0.03	1.07	0.94	1.06	0.20
	no 22−24 μm	0.08	0.81	0.91	0.86	0.19
	no 60−70 μm	0.07	1.18	0.92	1.18	0.30
	no SPIRE	0.21	1.15	0.87	1.24	0.34
γ	all	0.00	1.25	0.94	1.18	1.36
	no 8 μm	0.00	1.17	0.94	1.19	1.43
	no 22−24 μm	0.02	1.25	0.74	3.77	6.43
	no 60−70 μm	0.00	1.14	0.94	1.23	1.36
	no SPIRE	0.00	1.10	0.93	1.17	1.33
q_{PAH}	all	0.74	0.71	0.92	0.89	0.11
	no 8 μm	1.00	0.61	0.88	0.85	0.20
	no 22−24 μm	0.88	0.55	0.79	0.77	0.15
	no 60−70 μm	1.01	0.63	0.89	0.89	0.17
	no SPIRE	0.84	0.69	0.92	0.89	0.14
$\log L_{IR}$	all	0.00	1.00	1.00	1.00	0.00
	no 8 μm	0.01	1.00	1.00	1.00	0.00
	no 22−24 μm	−0.03	1.00	1.00	1.00	0.00
	no 60−70 μm	−0.09	1.01	1.00	1.00	0.00
	no SPIRE	−0.02	1.00	1.00	1.00	0.00
$\log M_{dust}$	all	−0.03	1.00	0.99	0.99	0.01
	no 8 μm	−0.04	1.00	0.99	0.99	0.01
	no 22−24 μm	−0.05	1.01	1.01	1.00	0.01
	no 60−70 μm	0.06	0.98	0.98	0.99	0.01
	no SPIRE	−0.14	1.01	1.01	0.99	0.02

Table 5. Statistics from the fitting of the 146 normal LTGs.

	Best fit from χ^2			
	median	σ	min	max
χ^2_{red}	2.25	5.33	0.10	42.72
U_{min}	2.00	1.70	0.20	8.00
q_{PAH} (%)	4.58	0.85	0.47	4.58
γ (%)	0.76	1.73	0.1	12.3
$\log(L_{IR}/L_\odot)$	9.48	0.54	8.21	10.96
$\log(M_{dust}/M_\odot)$	7.07	0.50	5.77	8.42
	Estimation from the PDF			
	median	σ	min	max
U_{min}	1.96 ± 0.47	1.76	0.26	8.58
q_{PAH} (%)	4.16 ± 0.42	0.76	1.22	4.58
γ (%)	0.75 ± 0.5	2.03	0.23	14.7
$\log(L_{IR}/L_\odot)$	9.47 ± 0.03	0.53	8.24	10.94
$\log(M_{dust}/M_\odot)$	7.02 ± 0.08	0.48	5.77	8.38

for metal-rich high-mass galaxies, confirming what we observe in Fig. 3. Rémy-Ruyer et al. (2013) showed with a sample of galaxies with metallicities ranging from 0.03 to 1 $Z_\odot$ that β obtained from modified blackbody fit shows a large spread from 0.5 to 2.5.

These disagreements between the observations and the models are difficult to interpret as they can have different origins. On the one hand, the way that errors in the photometry are computed determine the relative weights of the different bands, and thus play an important role in constraining the models, the case of the 22 and 24 μm being one illustration. On the other hand, the trend between the stellar mass and the χ^2_{red} also suggests that the models do not reproduce the observations of high-mass galaxies very well, and the 500 μm observations of low-mass systems are not reproduced by the DL07 models.

4.4.2. Statistics of the output parameters

The statistics of the fits and of the derived parameters are presented in Table 5. The median χ^2_{red} is 2.25. The median estimated value of U_{min} is 1.96 ± 0.47. If we consider the relation obtained by Aniano et al. (2012), this median U_{min} corresponds to a median temperature of the dust of 22 K. We find a median estimated q_{PAH} of 4.16 ± 0.42%. We obtain a median γ of 0.75 ± 0.5% when considering only the 24 μm sample. Finally, this late-type nondeficient sample is characterized by a median $\log(L_{IR}/L_\odot)$ of 9.47 ± 0.03 and $\log(M_{dust}/M_\odot)$ of 7.02 ± 0.08. We compare the dust masses we derive with those obtained for the same galaxies by Cortese et al. (2012b), using only SPIRE bands, and find good agreement. The median ratio between the M_{dust} of Cortese et al. (2012b) and ours is 1.02, with a standard deviation of 0.02.

The SEDs obtained from the minimum χ^2_{red} fit for each galaxy are shown in Figs. 4 and 5. They are normalized to the observed 2MASS K-band flux densities as the galaxies of our sample were selected in this band (see Boselli et al. 2010b, for a description of the K band flux densities). In each panel, we show the best-fitted SEDs, color-coded according to the estimated values of the three output parameters from the models (U_{min}, q_{PAH} and γ), plus the L_{IR} and the M_{dust} directly derived from the fits.

We notice a color gradient with U_{min}, indicating a relation with the shape of the SED. By definition, U_{min} controls the minimum and dominant equilibrium dust temperature, therefore controlling the wavelength peak of the SED, as we can see on the top panel of Fig. 4. The middle panel of Fig. 4 shows that q_{PAH} parameter impacts the shape of the SED handling the intensity of the PAH bands. However, our sample is dominated by galaxies with $q_{PAH} > 4\%$. This concerns 91 out of 146 galaxies, implying that there is a need for models with a larger range of PAH. Furthermore, the most massive galaxies, with $\log(M_*/M_\odot) > 10$, have a PAH fraction >4% and larger χ^2 values. This suggests that the lesser quality of the fit of the most massive galaxies is
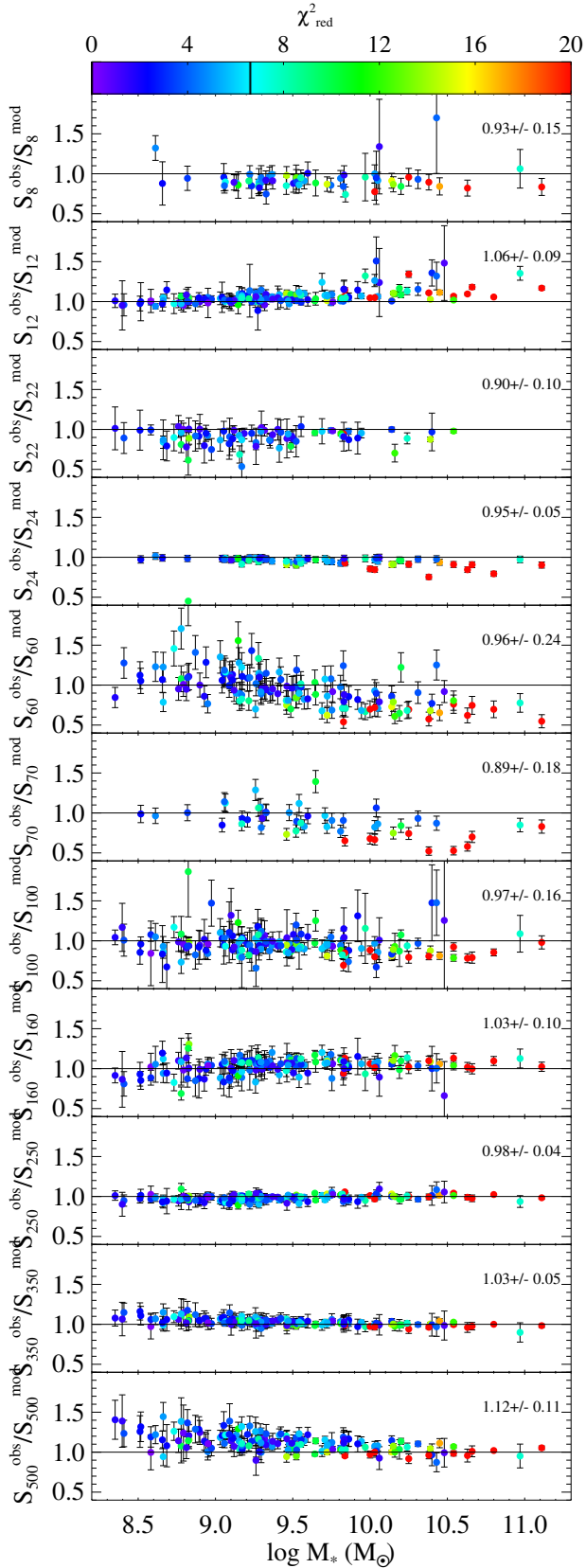
Fig. 3. Observed to modeled flux densities ratios for every photometric band (from $8\,\mu$m, *top panel*, to $500\,\mu$m, *bottom panel*) versus the stellar mass. Points are color-coded according to the reduced χ^2 associated with the fit. For each wavelength, we indicate the mean value and the standard deviation of the ratios. High-mass systems have larger χ^2. DL07 models underestimate the $500\,\mu$m observations, especially for low-mass systems.
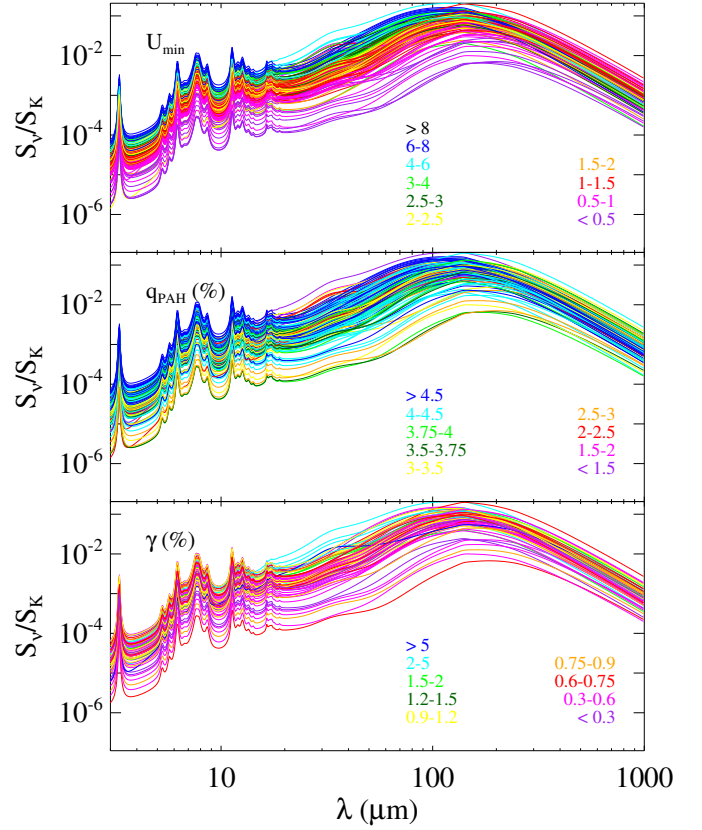
Fig. 4. Best-fit SEDs normalized to the observed *K*-band flux densities and color-coded according to the estimated value of the DL07 output parameter (*top panel*: γ, *middle panel*: $q_{\rm PAH}$, and *bottom panel*: $U_{\rm min}$).
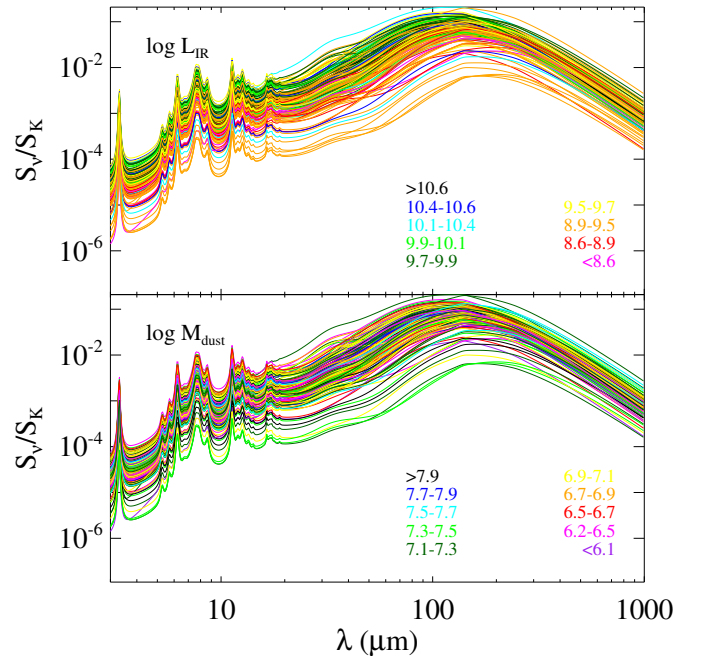
Fig. 5. Best-fit SEDs normalized to the observed *K*-band flux densities and color-coded according to the value of the resulting $\log L_{\rm IR}$ (*top panel*), and $\log M_{\rm dust}$ (*lower panel*).

due to the small range of $q_{\rm PAH}$ values available. An increase in γ translates to a bump in the $25-60\,\mu$m range, as shown in the bottom panel of Fig. 4. The lack of observational data in this

Table 6. Comparison of the outputs parameters from DL07 determined in this work, by Dale et al. (2012; KINGFISH) and by Draine et al. (2007; SINGS) for four galaxies in common.

Galaxy	Parameter	HRS	KINGFISH	SINGS
M 99	U_{min}	4.49 ± 0.50	3.0	1.5
	q_{PAH} (%)	4.58 ± 0.00^a	6.9	4.5
	γ (%)	0.73 ± 0.30	0.8	0.96
	$\log(L_{IR}/L_\odot)$	10.83 ± 0.01	10.6	10.91
	$\log(M_{dust}/M_\odot)$	7.97 ± 0.04	7.95	8.55
M 100	U_{min}	2.47 ± 0.35	2.0	1.2
	q_{PAH} (%)	4.58 ± 0.00^a	5.9	4.2
	γ (%)	0.65 ± 0.28	0.9	0.85
	$\log(L_{IR}/L_\odot)$	10.72 ± 0.01	10.5	10.82
	$\log(M_{dust}/M_\odot)$	8.12 ± 0.06	8.07	8.57
NGC 4536	U_{min}	2.58 ± 0.48	3.0	5.0
	q_{PAH} (%)	4.16 ± 0.42	4.3	3.5
	γ (%)	3.29 ± 0.87	2.7	3.31
	$\log(L_{IR}/L_\odot)$	10.45 ± 0.02	10.3	10.79
	$\log(M_{dust}/M_\odot)$	7.72 ± 0.05	7.61	7.82
NGC 4725	U_{min}	0.52 ± 0.15	0.6	0.7
	q_{PAH} (%)	4.43 ± 0.33	6.6	4.5
	γ (%)	0.39 ± 0.25	0.4	0.16
	$\log(L_{IR}/L_\odot)$	10.12 ± 0.02	9.9	10.18
	$\log(M_{dust}/M_\odot)$	8.22 ± 0.12	7.98	8.20

Notes. [a] For M 99 and M 100, the PDF of q_{PAH} is very narrow and yields to an error of 0.0. This emphasizes the need for higher fractions of PAH for these galaxies.

range can explain the difficulty in constraining γ, already outlined in Sect. 4.3.

The fitting procedure also provides us with the L_{IR} and the M_{dust} (Fig. 5). A trend between the L_{IR} and the shape of the SED is visible. Late-type galaxies are more gas-rich, and thus have a higher dust content, therefore, they form more stars. The tight link between the SFR and the L_{IR} yields to the trend observed in the top panel of Fig. 5. No particular relation is found between M_{dust} and S_ν/S_K.

4.4.3. Comparison with the literature

This sample and the SINGS/KINGFISH (Kennicutt et al. 2003, 2011) sample have four galaxies in common: M 99, M 100, NGC 4536, and NGC 4725. We compare, in Table 6, the results from the fits from our procedure with those found by Draine et al. (2007) and Dale et al. (2012) fitting DL07 models. For M 99, M 100, and NGC 4725, Draine et al. (2007) did not have any submm constraint on the SED, except for NGC 4536 for which they had a SCUBA 850 μm flux density. Dale et al. (2012) benefited from a larger set of models yielding to a larger parameter space to be explored with $0.01 < U_{min} < 30$, $3 < \log U_{max} < 8$ and $0\% < q_{PAH} < 12\%$. Despite the differences with the photometric coverage for SINGS and with the parameter ranges for KINGFISH, we find results in agreement.

5. Comparison with physical parameters

We study here the relations between the output parameters of the models and various physical variables available for our sample. In a phenomenological model independent approach, the relations between these physical properties and the FIR colors of the gas-rich late-type galaxies have been analyzed in Boselli et al. (2012) where a complete description of these variables can be

Table 7. Completeness of the integrated properties for the final sample of 146 galaxies.

Properties	Number of galaxies
M_*	146
SFR	141
b	141
$\Sigma(H\alpha)$	129
$\mu_e(H)$	146
$12 + \log(O/H)$	124
$A(FUV)$	117
L_{IR}	146
M_{dust}	146

found. Here we provide a very brief description. The number of galaxies of our sample for which ancillary data are available are given in Table 7.

Stellar masses (M_*) are estimated from H-band data, and from mass–luminosity relations, as determined by the chemo-spectrophotometric galaxy evolution models of Boissier & Prantzos (2000), using the relation given in Boselli et al. (2009). The effective surface brightness in H-band, $\mu_e(H)$, provides a measurement of the intensity of the ISRF produced by the old stellar population. The Hα surface brightness is a tracer of the intensity of the ionizing UV emission and provides us with information on the present star formation activity (Boselli et al. 2009). The SFRs are calculated using the standard calibration of Kennicutt (1998) to convert Hα and FUV luminosities corrected from dust attenuation using the Balmer decrement (Boselli et al. 2009) and the corrections of Cortese et al. (2008), respectively. The final SFR corresponds to the mean value of the SFR determined from the Hα data and the FUV data (Boselli et al. 2009).

The birthrate parameter b (Scalo 1986; Kennicutt 1998), defined as the ratio between the present star formation activity and the star formation activity averaged on the galaxy entire life, is defined by Boselli et al. (2001):

$$b = \frac{SFR}{\langle SFR \rangle} = \frac{SFR t_0 (1 - R)}{M_*}, \qquad (4)$$

with t_0 the age of the galaxy, M_* its stellar mass, and R (assumed to be 0.3) the fraction of re-injected gas into the ISM due to stellar winds. The SFR being linked to the UV or Hα fluxes and M_* to the NIR fluxes, b is thus tightly linked to the hardness of the UV radiation field. Moreover, the specific star formation rate (sSFR, Brinchmann et al. 2004) is widely used and can be linked to the birthrate parameter as:

$$sSFR = \frac{SFR}{M_*} = \frac{b}{t_0 (1 - R)}. \qquad (5)$$

Hughes et al. (2013) measured the metallicity of the galaxies in our sample with integrated spectroscopy, where different calibrations are used to derive $12 + \log(O/H)$, depending on the availability of the main emission lines. $A(FUV)$, in magnitude, is the attenuation of the nonionizing UV radiation, defined as the ratio between the FIR and the FUV (at 1539 Å) flux densities, following the recommendations of Cortese et al. (2008).

The outputs of DL07 models are compared to these integrated properties. We decompose our sample in three groups according to the morphological types of the galaxies: Sa, Sab and Sb, Sbc Sc and Scd, and Sd, Im and BCD[6]. Galaxies

---

[6] We follow the groups and symbols used in Boselli et al. (2012) to allow a better comparison between the two works.
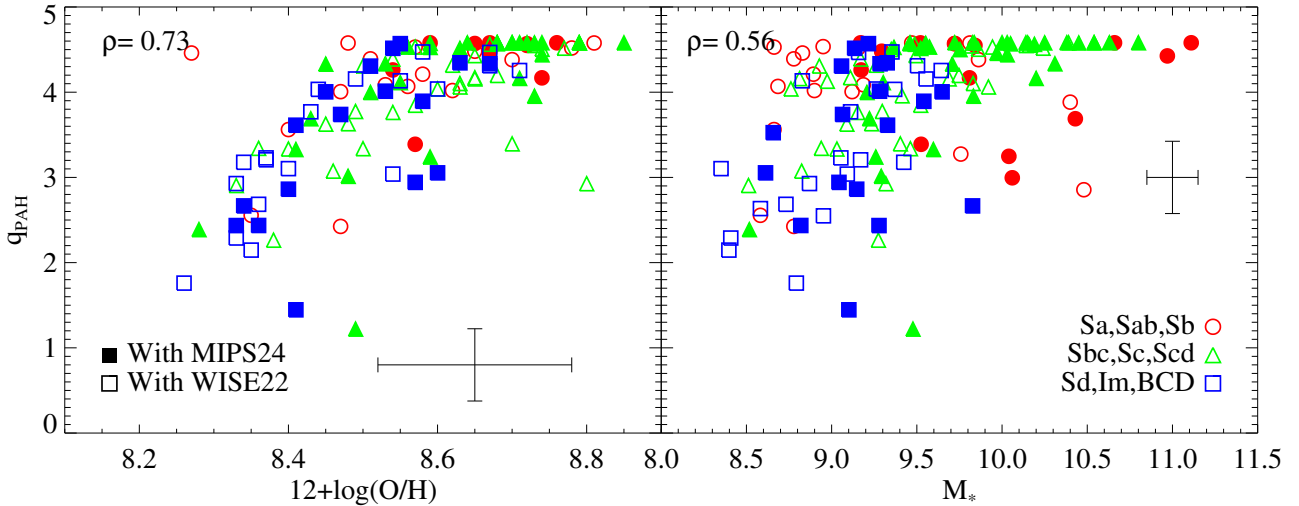
Fig. 6. Relation between the fraction of PAH and the metallicity (*left panel*) and between the fraction of PAH and the stellar mass (*right panel*). Galaxies are color-coded according to their morphological type. Red: Sa-Sb; green: Sbc-Scd; and blue: Sd-BCD. Filled symbols are for galaxies with a MIPS 24 μm observations and thus a good constraint on γ. Empty symbols are for galaxies with a WISE 22 μm observations. The Spearman correlation coefficients, ρ, are provided. The cross gives the typical error bar on the data.

with a MIPS24 measurement are represented by filled symbols whereas galaxies with WISE22 are represented by empty symbols. All the relations are presented in Fig. D.1, and discussed in Appendix D. For the total sample, we give the Spearman correlation coefficient of the relations. With a number of objects larger than 100, a correlation is expected to be real with a Spearman correlation coefficient larger than 0.40. We outline here the most interesting correlations between the properties and the DL07 output parameters.

One of the strongest trends is found between the metallicity and q_{PAH} (ρ = 0.73, Fig. 6), Metal-rich galaxies, with 12 + log(O/H) have a high fraction of PAH. The PAH are destroyed in low-metallicity environment by the UV radiation field, which propagates more easily due to the lower dust content. This was demonstrated in Galliano et al. (2003), Boselli et al. (2004), Madden et al. (2006), Engelbracht et al. (2008), and Gordon et al. (2008) for galaxies with lower metallicities. We should note that, in this work, we observe this relation for metal-rich galaxies with 8.3 < 12 + log(O/H) < 8.85. We also confirm, on a larger sample, the results of Engelbracht et al. (2005) who found a weakening of the PAH features at low metallicity from 8 to 24 μm flux density ratios, and Smith et al. (2007) who found that the strength of the PAH bands is directly linked to the metallicity from the *Spitzer*/IRS spectrum of 59 nearby galaxies. However, Galliano et al. (2008) suggested that the absence of PAH could be due to a delayed injection of carbon dust by AGB stars, and Sandstrom et al. (2012) proposed that the PAH were formed in molecular clouds, which have a lower filling factor in low-metallicity environments. A good relation is found between the stellar mass and q_{PAH} (ρ = 0.56). Indeed, massive galaxies are also more metal-rich (Tremonti et al. 2004).

A good correlation is found between the U_{min} parameter, which is the intensity of the diffuse ISRF (Draine et al. 2007; Aniano et al. 2012), and the Hα surface brightness (ρ = 0.70), and a moderate anticorrelation between U_{min} and the H-band surface brightness in AB mag arcsec^{-2} (ρ = −0.49), as shown in Fig. 7.

A similar behavior was outlined by Boselli et al. (2012) where they found relations between FIR colors sensitive to the IR emission peak (S_{60}/S_{250}, S_{60}/S_{100} and S_{100}/S_{500}) and ΣHα

and μ_e(H). This is consistent with what we observe in this work, as the U_{min} parameter regulates the position of the IR emission peak (see Fig. 4). The stars of the diffuse component emit the bulk of their radiation in NIR, which can be probed by the H-band surface brightness. It is thus expected to find a relation between U_{min} and μ_e(H). This means that the diffuse dust is heated by the old stellar component. Furthermore, a good relation is also found with ΣHα, which is the ionizing surface brightness due to the young stars. The diffuse dust component seems to be also heated by the young stars component in star forming regions. With a Spearman coefficient of −0.44, there is not a strong correlation between μ_e(H) and ΣHα that could have originated the relations with U_{min}. This result from integrated galaxies seems incompatible with works based on the analysis of resolved galaxies (Bendo et al. 2010, 2012a; Boquien et al. 2011). These studies showed that at wavelengths shorter than 160 μm, most of the dust is heated by massive stars whereas at wavelengths longer than 250 μm, the dust is primarily heated by evolved stellar populations. This discrepancy can be explained by the fact that the brightest regions of the galaxies dominate the emission measured with integrated flux densities. For late-type galaxies, in IR, the brightest regions are heated by star formation and thus are linked to the Hα emission, explaining the correlation that we observe. Therefore, enhanced star formation might increase U_{min}, in which case the interpretation of U_{min} may be that it no longer traces only the diffuse ISRF from evolved stars but just the lowest energy radiation field within the galaxies for integrated studies.

6. Infrared templates

Thanks to the wealth of photometric data and physical properties available for the HRS galaxies, the gas-rich galaxy sample studied in this work is ideal for building new, well-constrained, IR templates. The majority of star-forming galaxies are known to follow an *SFR–M_** correlation, called the main sequence (MS), and galaxies that lie above this sequence are experiencing a starburst event (Elbaz et al. 2011). Several studies have put constraints on the MS at different redshifts (e.g., Peng et al. 2010; Rodighiero et al. 2011; Heinis et al. 2014). Thanks to its design,
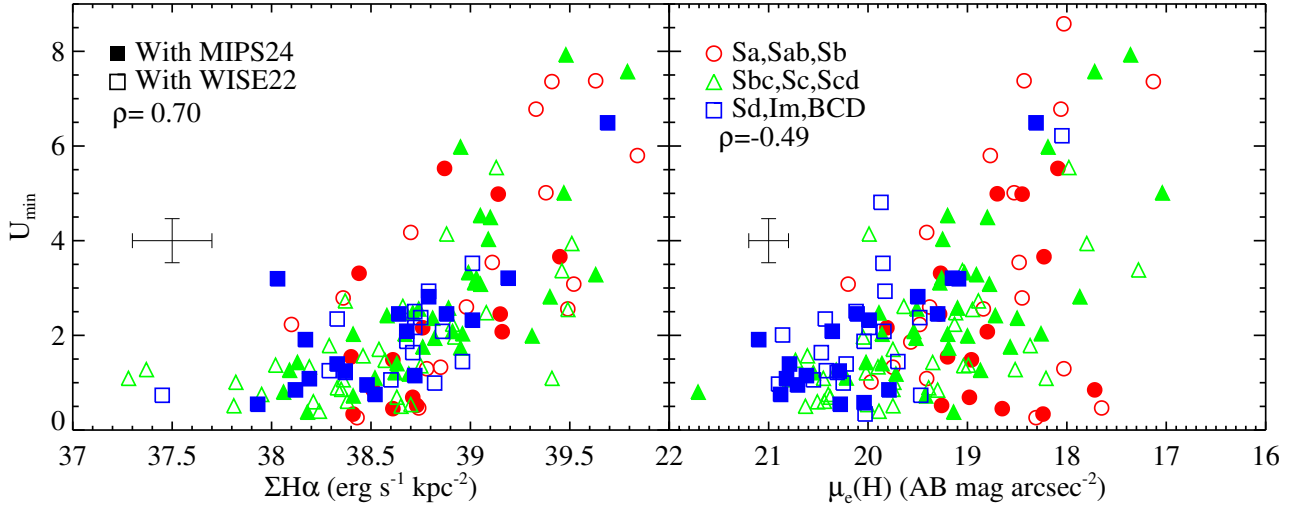
Fig. 7. Relation between U_{min}, tracer of the minimum intensity of the ISRF, the Hα and H-band surface brightness (*left panel* and *right panel*, respectively). Galaxies are color-coded according their morphological type. Red: Sa-Sb; green: Sbc-Scd; and blue: Sd-BCD. Filled symbols are for galaxies with a MIPS 24 μm observations and thus a good constraint on γ. Empty symbols are for galaxies with a WISE 22 μm observations. The Spearman correlation coefficient, ρ, is provided. The cross gives the typical error bar on the data.
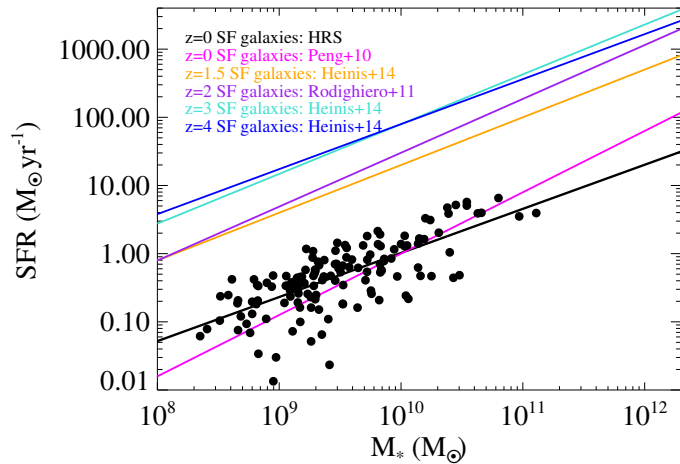
Fig. 8. HRS galaxies placed on the *SFR–M*$_*$ plot (black dots). The best linear fit is shown as a solid black line. For comparison, other MS fits estimated at different redshifts are shown. The HRS galaxies are consistent with the relation of Peng et al. (2010), however, it seems that HRS low-mass systems have higher SFRs.

Fig. 9. *Top panel*: mean SED of $z = 0$ normal star forming galaxies. The mean values of the physical parameters associated with the sample are indicated. *Bottom panel*: dispersion of the models used to compute the mean SED in all of the bands of our photometric coverage.

volume-limit, and completeness in the K-band, the HRS is well suited for providing constraints on the local MS as the results are relatively free of distance-related biases that could appear in a flux-limited sample of galaxies. Figure 8 places the late-type star-forming galaxies of our sample in an *SFR–M*$_*$ plot, along with several MS estimations. The SFRs are calculated assuming a Salpeter initial mass function (IMF) and the stellar masses are calculated assuming an IMF of Kroupa, we thus corrected the SFRs by a factor of -0.17 dex, following the results of Brinchmann et al. (2004) and Buat et al. (2014). A direct comparison can be done only with the sample of Peng et al. (2010) since it is the only one based on local galaxies. The MS local estimation of Peng et al. (2010) was built from a subsample of SDSS galaxies with $0.02 < z < 0.085$. Their selection is only complete at $z = 0.085$ above a stellar mass of $\approx 10^{10.4} M_\odot$. There is relatively good agreement with the MS local estimation of Peng et al. (2010). The observed difference in the slope may come from the different ranges of stellar masses that our sample

and the sample of Peng et al. (2010) cover. The best linear fit determined from our galaxies is:

$$\log SFR = 0.65 \times \log M_* - 6.46. \qquad (6)$$

6.1. Construction of the templates

We computed the mean SED of the whole sample of late-type nondeficient galaxies from this work to provide the typical $z = 0$ SED of nearby normal galaxies (Fig. 9). To do so, we averaged all the best-fit SEDs of the gas-rich subsample studied in the previous sections. We provide the mean values of all of the physical properties that are associated with the sample from which this mean SED originates (Fig. 9).

We then binned the best-fit models of the sample by birthrate parameter, SFR, dust mass, metallicity, stellar mass, H-band effective surface brightness, Hα surface brightness, and morphological type (Fig. 10). The bins (indicated on Fig. 10) have been chosen in order to have a consistent number of objects in each
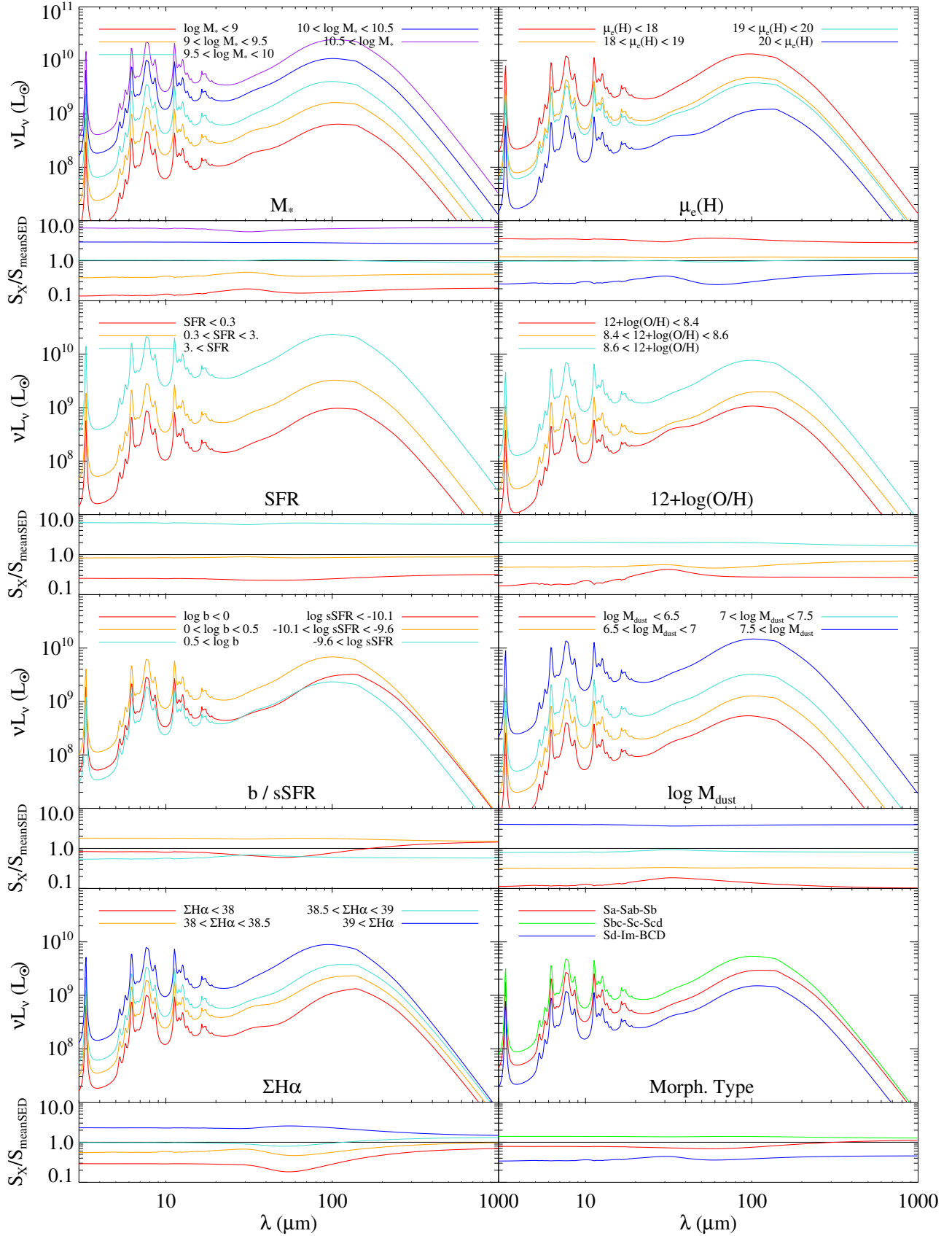
Fig. 10. Library of templates derived from the fits. SEDs are binned by (*from top to bottom and left to right*): stellar mass, SFR, birthrate parameter (sSFR), Hα surface brightness, *H*-band effective surface brightness, metallicity, dust mass, and morphological types. For each class of templates, the *lower panels* show the ratio between the different binned templates and the mean HRS SED of Fig. 9.

bin. For each bin, the best-fit models of the galaxies are averaged to provide the template corresponding.

The new set of IR templates is constrained with submm data, and they benefit from good photometric coverage of the HRS galaxies. The HRS was designed to be complete in stellar mass, and the selection criteria applied to these galaxies make our sample representative of the late-type galaxies of the local Universe. Therefore, these templates provide constraints on the dust emission in the nearby Universe. However, as these templates were built from DL07 models, we should note that they may underestimate the dust emission at $\lambda \geq 500\,\mu m$ for low-mass systems, as discussed in Sect. 4.4. The mean SED template and the binned SED templates are available to the community via the HEDAM website[7].

6.2. Comparison with the literature

We compare our templates with the most popular IR SED libraries used in the literature, i.e., CE01, DH02, Rieke et al. (2009), Elbaz et al. (2011), Magdis et al. (2012), Smith et al. (2012a) and Berta et al. (2013). These libraries are based on different physical assumptions, however, this discussion is mainly focused on the shape of the SEDs and not on the physical description of the dust. We thus give a brief description of these libraries here.

The CE01 empirical SEDs have been computed as a function of the L_{8-1000} to reproduce the ISO, IRAS, and SCUBA data of local IR luminous galaxies. They used data between 0.44 and $850\,\mu m$, however, there is a large gap of observations between 100 and $850\,\mu m$. Dale & Helou (2002) built, using a semi-empirical method, a library of galaxy SEDs following the dust mass power-law distribution as a function of the intensity of the ISRF U, i.e. $dM(U) \propto U^{-\alpha}dU$. This set of templates reproduces the IR colors of galaxies thanks to a unique parameter α linked to the S_{60}/S_{100} flux density ratio. A galaxy with $\alpha \approx 1$ is active in star formation, whereas a galaxy with $\alpha \approx 2.5$ is qualified as normal. The templates of Rieke et al. (2009) are averaged templates constructed from ISO and *Spitzer* observations of eleven local luminous IR galaxies (LIRG) and ultra luminous IR galaxies (ULIRG). However, CE01, DH02, and Rieke et al. (2009) are pre-*Herschel* libraries and did not benefit from the excellent FIR/submm coverage that we have from PACS and SPIRE. Finally, Smith et al. (2012a) used a sample of galaxies selected at $250\,\mu m$ from the H-ATLAS field (Eales et al. 2010). They used the models of da Cunha et al. (2008) and performed a panchromatic SED fitting based on energy balance. As a result of these fits, they provided median templates binned by physical parameters for galaxies up to $z = 0.5$. However, we should note that they did not have any constraint between the K band and the $100\,\mu m$ flux densities.

Recent studies using *Herschel* data computed libraries designed for higher redshift sources. Thanks to *Herschel* data, Elbaz et al. (2011) showed that the MS galaxies also verify a universal total to MIR luminosity ratio: IR8 = L_{IR}/L_8, with L_8, the rest-frame luminosity at 8 μm, suggesting that they have the same IR SED shape. In this relation, the starburst galaxies are outliers, with higher IR8. Thus, Elbaz et al. (2011) derived a single template for MS galaxies, with a single IR8 at all redshifts up to 2, and a single template for starburst galaxies with a significantly higher value of IR8. Magdis et al. (2012) adopted the same philosophy, but introduced a variation of the shape of the SED with the redshift. They fit Draine & Li (2007) models

to individual galaxies and stacked ensembles at $0.5 < z < 2$ using data from MIR to millimeter range. They derived a relation between $\langle U \rangle$ and z and used it to construct template SEDs of MS galaxies from $z = 0$ to $z = 2.5$, fixing $\gamma = 0.02$ and $q_{PAH} = 3.19\%$ for $z < 1.5$ and 2.50% for $z > 1.5$. They assume a flattening evolution of $\langle U \rangle$ beyond $z = 2.5$. For starburst galaxies, they used their best fit of GN 20, a well-studied very luminous and distant submm galaxy. Berta et al. (2013) combined UV to submm data of galaxies from large fields (GOODS-N, GOODS-S, and COSMOS) to reproduce the distribution of galaxies in ten rest-frame color spaces, using a superposition of multivariate Gaussian modes. According to this model, they classified galaxies and built the median SED of each class. Each median SED was then fitted using a modified version of the MAGPHYS code (da Cunha et al. 2008) that combines stellar light, emission from dust heated by stars, and a possible contribution from dust heated by an AGN.

We compare our templates with the one available in the literature in Fig. 11, where they have all been normalized to L_{8-1000}. The choice of this normalization comes from the fact that these libraries are essentially used to provide a measurement of the L_{IR} of the galaxies, the templates of CE01 are even calibrated to this parameter. We also divide them into two categories: in the left panel, the libraries representative of the nearby Universe, and in the right panel, the libraries developed for high-z studies.

In the left panel, we focus first on the low-z libraries, From each library, we select the templates that match the properties of our sample. For CE01, we select the templates with $\log(L_{IR}/L_\odot) < 10.9$, and we note that there is no template for $\log(L_{IR}/L_\odot)$ lower than 8.5 that could be representative of some galaxies of our sample. For DH02, based on the S_{60}/S_{100} ratios of our sample, we select templates with $\alpha > 1.5$. We should note that for 30% of our galaxies having a $60\,\mu m$ measurement, templates with $\alpha > 4$, the largest value of α available from the DH02 library, are needed to reproduce the observed S_{60}/S_{100}. For the Rieke et al. (2009) templates, we select those with $\log(L_{IR}/L_\odot) < 11$. For the Smith et al. (2012a) library, we show the templates corresponding to $\log(L_{IR}/L_\odot) < 11$. We show all of the HRS templates presented in Fig. 10. The CE01, DH02, Rieke et al. (2009), and Smith et al. (2012a) templates contain stellar emission that explain part of the differences seen at $\lambda < 10\,\mu m$ compared to ours which are purely dust emission. All the libraries here are consistent within ≈ 0.2 dex around $100\,\mu m$. Indeed, pre-*Herschel* libraries (CE01 and DH02) benefit from IRAS $100\,\mu m$ measurements, and post-*Herschel* libraries presented here can rely on PACS data at $100\,\mu m$. This part of the SED is thus well constrained by the observations. At longer wavelength, the low-z templates have consistent shapes. However, we remark in Fig. 3 that DL07 models have difficulty reproducing the $500\,\mu m$ observations, thus despite this good agreement between the different libraries, updates in the models are needed to be able to reproduce the data. At wavelength shorter than $100\,\mu m$, CE01 and DH02 templates represent dust temperatures that are significantly higher than those of Smith et al. (2012a) and this work due to selection criteria. Indeed, the IRAS selections for the normal galaxies introduce a bias toward warmer sources. The templates of Rieke et al. (2009), benefitting from the IRS (Infrared Spectrograph) spectra of *Spitzer* is in good agreement with the HRS templates. There is a particularly striking disagreement between the templates in MIR-FIR, which can reach up to two orders of magnitude. The pre-*Herschel* libraries have IR peaks that are shifted toward shorter wavelength compared to the post-*Herschel* ones, resulting in higher temperatures for the warm dust. What increases the disagreement between the libraries in
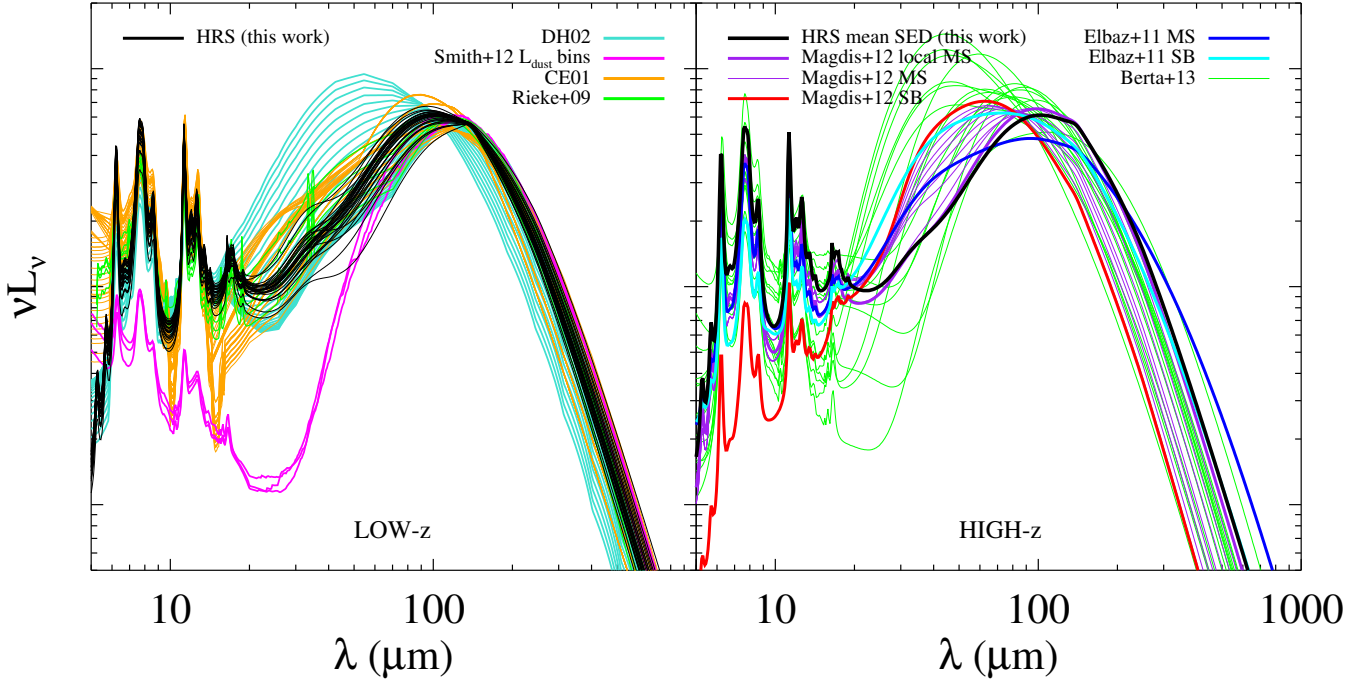
Fig. 11. Templates from this work compared to the most popular IR SED templates normalized to L_{8-1000}. *Left panel*: low-z templates. In black: all of the templates computed in this work (Fig. 10). For better comparison, we plot only the templates of the different libraries whose properties (L_{IR}, α) match those of the HRS. In turquoise: templates of Dale & Helou (2002) with α ranging from 1.5 to 4. In orange: library of Chary & Elbaz (2001) with $\log(L_{IR}/L_{\odot}) < 10.9$, in magenta: median templates of Smith et al. (2012a) binned in dust luminosity for $\log(L_{IR}/L_{\odot}) < 11$, and in green: templates of Rieke et al. (2009) with $\log(L_{IR}/L_{\odot}) < 11$. *Right panel*: high-$z$ templates. In black: mean SED from HRS (Fig. 9) as a reference for $z = 0$ galaxies. In purple: MS templates and in red the starburst template from Magdis et al. (2012). In blue: main MS template from Elbaz et al. (2011); and in cyan: starburst template from Elbaz et al. (2011). In green: selected templates from Berta et al. (2013). At low-z, there is a large discrepency between the templates between 20 and $100\,\mu$m.

this $20-100\,\mu$m range is the very low luminosity of the Smith et al. (2012a) median SEDs. This is probably due to the fact that Smith et al. (2012a) did not have any MIR and FIR data up to $100\,\mu$m to constrain their templates. Even if we do not take this library into account, the disagreement of the low-z libraries between 20 and $100\,\mu$m is very important. The emission in this range is a combination of emission from warm dust populations and stochastically heated grains. This warm dust, which peaks around $100\,\mu$m and even at shorter wavelengths, is theoretically an excellent tracer of star formation. It is unclear if the larger scatter we observe in FIR is only due to uncertainties in the way templates are built (there are few observational constraints in this range), or whether this translates to variations in the physical properties in galaxies. Indeed, based on the dust emission models of Draine & Li (2007), the relative contribution of photodissociation regions and diffuse stellar component to the heating of the dust impacts the SED in this particular range.

In the right panel, we show our mean SED as a representative SED for $z = 0$ galaxies along with templates based on the study of high-z galaxies done with *Herschel* observations. As for the low-z libraries, these templates agree relatively well around $100\,\mu$m, except for the SED of the MS galaxies from Elbaz et al. (2011). At longer wavelengths, the high-z library of Magdis et al. (2012) and of this work also have the same slope. Elbaz et al. (2011) computed their SEDs template by finding the mean of all of the SEDs of their sample galaxies, normalized to $10^{11}/L_{IR}$, resulting in a lower β for both their MS and starburst templates. The $z = 0$ main sequence template of Magdis et al. (2012) (thick purple solid line) is in good agreement with the mean SED of HRS galaxies. With the increase in redshift, Magdis et al. (2012) templates shift toward shorter wavelength,

and thus higher dust temperature. We select some templates out of the 32 available from the library of Berta et al. (2013) by removing templates with AGN components and those typical of high-z sources, such as Lyman break galaxy template. These templates show a large variety of SED shape, temperature of the dust and PAH bands intensity. The submm part of the Berta et al. (2013) templates is very similar to Magdis et al. (2012) and the mean SED of this work, however, the MIR-FIR domain show a large range of luminosities.

7. Conclusions

Thanks to the wealth of photometric ancillary data available for the HRS, we perform the NIR photometry of the HRS galaxies (see Appendix A) and compute their IR SED from 8 to $500\,\mu$m. We provide an updated method to remove the stellar contribution in NIR and MIR using different SFH according to the morphological type of the galaxies. The Draine & Li (2007) models are fit to the HRS galaxies. Even though this work focuses on the dust properties of a gas-rich galaxy subsample, we provide the results of the SED fitting of the other HRS galaxies (early-type and H I-deficient galaxies) in Appendix C. We note that a strong constraint in the $20-60\,\mu$m range, at least a reliable measurement at $24\,\mu$m, is mandatory to have a reliable estimation of the relative contribution of PDR to the total IR SED. The comparison between observed and modeled flux densities shows that Draine & Li (2007) models underestimate the $500\,\mu$m observations for low-mass systems. We also note an underestimation of the $160\,\mu$m measurements, especially for high-mass systems.

The median diffuse ISRF intensity of our late-type sample is 1.96 ± 0.47 times the ISRF intensity of the Milky Way

corresponding to a median dust temperature of 22 K, with a median contribution of the PDRs of 0.75% ± 0.5%, and a contribution of the PAH to the total dust mass of 4.16% ± 0.42. The median $\log(L_{\rm IR}/L_\odot)$ is 9.47 ± 0.03 and the median dust mass of the sample is $\log(M_{\rm dust}/M_\odot)$7.02 ± 0.08.

We compared these parameters derived from the fitting procedure to integrated properties of the galaxies. From this comparison, in agreement with Boselli et al. (2012), we confirm a good correlation between the fraction of PAH and the metallicity, implying a weakening of the emission of the PAH in galaxies with lower metallicities. We thus confirm results obtained from MIR colors studies (Boselli et al. 2004; Engelbracht et al. 2005) and spectroscopy (Smith et al. 2007). From this relation follows a good correlation between the fraction of PAH and the stellar mass, as most massive systems have higher metallicities. Moderate to good correlations are found between the minimum intensity of the ISRF and the H-band and Hα surface brightness implying that, based on integrated galaxy analysis, the diffuse dust component seems to be heated by both the young stars in star forming regions and the diffuse evolved populations. This confirms the results of Boselli et al. (2012), which were also based on an integrated study of galaxies, but is incompatible with an analysis based on resolved studies.

We placed the HRS galaxies in an SFR–M_* diagram, and compared them with fits of the MS galaxies at different redshifts. There is good agreement with the MS relation at $z = 0$ of Peng et al. (2010), even if HRS low-mass systems tend to have higher SFR. The best linear fit to the data is $\log SFR = 0.65 \times \log M_* - 6.29$. Thanks to the good photometric coverage of our sample, we are able to provide IR templates of nearby galaxies binned by the parameters that constrain the shape of the IR SED: birthrate parameter (or equivalently the $sSFR$), dust mass, metallicity, stellar mass, H-band effective surface brightness, Hα surface brightness, and morphological type. We also computed the mean SED of the subsample to provide a reference for any cosmological studies and simulations. The mean SED and the library can be found on the HEDAM website[8]. We compared this set of templates to the most popular IR pre-*Herschel* and post-*Herschel* libraries. At low-z, pre-*Herschel* libraries have a very warm dust component compared to post-*Herschel* ones, due to selection effects of IRAS galaxy samples. Compared to high-z libraries, our mean SED is in good agreement with the $z = 0$ MS template of Magdis et al. (2012). The IR peak of the MS template of Elbaz et al. (2011) is wider than the IR peak obtained in this work, and corresponds to a lower luminosity at 160 μm. In Appendix B, we provide new photometric data in the 8, 12, and 22 μm bands, taken by *Spitzer* and WISE, and used in the work. We also present in Appendix B, new coefficients to remove the stellar contribution from MIR observations.

the GOLDMine database (http://goldmine.mib.infn.it/). This publication makes use of data products from the Wide-field Infrared Survey Explorer, which is a joint project of the University of California, Los Angeles, and the Jet Propulsion Laboratory/California Institute of Technology, funded by the National Aeronautics and Space Administration.

References

Alton, P. B., Xilouris, E. M., Misiriotis, A., Dasyra, K. M., & Dumke, M. 2004, A&A, 425, 109
Aniano, G., Draine, B. T., Calzetti, D., et al. 2012, ApJ, 756, 138
Baes, M., Clemens, M., Xilouris, E. M., et al. 2010, A&A, 518, L53
Bendo, G. J., Dale, D. A., Draine, B. T., et al. 2006, ApJ, 652, 283
Bendo, G. J., Draine, B. T., Engelbracht, C. W., et al. 2008, MNRAS, 389, 629
Bendo, G. J., Wilson, C. D., Warren, B. E., et al. 2010, MNRAS, 402, 1409
Bendo, G. J., Boselli, A., Dariush, A., et al. 2012a, MNRAS, 419, 1833
Bendo, G. J., Galliano, F., & Madden, S. C. 2012b, MNRAS, 423, 197
Bendo, G. J., Griffin, M. J., Bock, J. J., et al. 2013, MNRAS, 433, 3062
Berta, S., Lutz, D., Santini, P., et al. 2013, A&A, 551, A100
Bianchi, S. 2008, A&A, 490, 461
Boissier, S., & Prantzos, N. 2000, MNRAS, 312, 398
Boquien, M., Calzetti, D., Combes, F., et al. 2011, AJ, 142, 111
Boselli, A., & Gavazzi, G. 2006, PASP, 118, 517
Boselli, A., Lequeux, J., Sauvage, M., et al. 1998, A&A, 335, 53
Boselli, A., Gavazzi, G., Donas, J., & Scodeggio, M. 2001, AJ, 121, 753
Boselli, A., Gavazzi, G., & Sanvito, G. 2003a, A&A, 402, 37
Boselli, A., Sauvage, M., Lequeux, J., Donati, A., & Gavazzi, G. 2003b, A&A, 406, 867
Boselli, A., Lequeux, J., & Gavazzi, G. 2004, A&A, 428, 409
Boselli, A., Boissier, S., Cortese, L., et al. 2009, ApJ, 706, 1527
Boselli, A., Ciesla, L., Buat, V., et al. 2010a, A&A, 518, L61
Boselli, A., Eales, S., Cortese, L., et al. 2010b, PASP, 122, 261
Boselli, A., Boissier, S., Heinis, S., et al. 2011, A&A, 528, A107
Boselli, A., Ciesla, L., Cortese, L., et al. 2012, A&A, 540, A54
Boselli, A., Hughes, T. M., Cortese, L., Gavazzi, G., & Buat, V. 2013, A&A, 550, A114
Boselli, A., Hughes, T. M., Cortese, L., Gavazzi, G., & Buat, V. 2014, A&A, 562, C3
Bot, C., Ysard, N., Paradis, D., et al. 2010, A&A, 523, A20
Brinchmann, J., Charlot, S., White, S. D. M., et al. 2004, MNRAS, 351, 1151
Buat, V., & Xu, C. 1996, A&A, 306, 61
Buat, V., Heinis, S., Boquien, M., et al. 2014, A&A, 561, A39
Calzetti, D., Kennicutt, Jr., R. C., Bianchi, L., et al. 2005, ApJ, 633, 871
Calzetti, D., Kennicutt, R. C., Engelbracht, C. W., et al. 2007, ApJ, 666, 870
Chary, R., & Elbaz, D. 2001, ApJ, 556, 562
Ciesla, L., Boselli, A., Smith, M. W. L., et al. 2012, A&A, 543, A161
Cortese, L., Boselli, A., Franzetti, P., et al. 2008, MNRAS, 386, 1157
Cortese, L., Davies, J. I., Pohlen, M., et al. 2010, A&A, 518, L49
Cortese, L., Boissier, S., Boselli, A., et al. 2012a, A&A, 544, A101
Cortese, L., Ciesla, L., Boselli, A., et al. 2012b, A&A, 540, A52
Cortese, L., Fritz, J., Bianchi, S., et al. 2014, MNRAS, accepted [arXiv:1402.4524]
da Cunha, E., Charlot, S., & Elbaz, D. 2008, MNRAS, 388, 1595
Dale, D. A., & Helou, G. 2002, ApJ, 576, 159
Dale, D. A., Gil de Paz, A., Gordon, K. D., et al. 2007, ApJ, 655, 863
Dale, D. A., Aniano, G., Engelbracht, C. W., et al. 2012, ApJ, 745, 95
de Looze, I., Baes, M., Bendo, G. J., et al. 2012a, MNRAS, 427, 2797
de Looze, I., Baes, M., Fritz, J., & Verstappen, J. 2012b, MNRAS, 419, 895
de Vaucouleurs, G., de Vaucouleurs, A., Corwin, Jr., H. G., et al. 1991, Sky and Telescope, 82, 621
Devereux, N. A., & Young, J. S. 1990, in NASA Conf. Publ. 3084, eds. D. J. Hollenbach & H. A. Thronson Jr., 92
Devereux, N. A., Jacoby, G., & Ciardullo, R. 1995, AJ, 110, 1115
Draine, B. T. 1978, ApJS, 36, 595
Draine, B. T., & Hensley, B. 2012, ApJ, 757, 103
Draine, B. T., & Lee, H. M. 1984, ApJ, 285, 89
Draine, B. T., & Li, A. 2007, ApJ, 657, 810
Draine, B. T., Dale, D. A., Bendo, G., et al. 2007, ApJ, 663, 866
Draine, B. T., Aniano, G., Krause, O., et al. 2014, ApJ, 780, 172
Dwek, E. 1986, ApJ, 302, 363
Eales, S., Dunne, L., Clements, D., et al. 2010, PASP, 122, 499
Elbaz, D., Dickinson, M., Hwang, H. S., et al. 2011, A&A, 533, A119
Engelbracht, C. W., Gordon, K. D., Rieke, G. H., et al. 2005, ApJ, 628, L29
Engelbracht, C. W., Blaylock, M., Su, K. Y. L., et al. 2007, PASP, 119, 994
Engelbracht, C. W., Rieke, G. H., Gordon, K. D., et al. 2008, ApJ, 678, 804
Fazio, G. G., Hora, J. L., Allen, L. E., et al. 2004, ApJS, 154, 10
Galametz, M., Madden, S. C., Galliano, F., et al. 2011, A&A, 532, A56

---

8   http://hedam.oamp.fr/HRS/

Galliano, F., Madden, S. C., Jones, A. P., et al. 2003, A&A, 407, 159
Galliano, F., Madden, S. C., Jones, A. P., Wilson, C. D., & Bernard, J.-P. 2005, A&A, 434, 867
Galliano, F., Dwek, E., & Chanial, P. 2008, ApJ, 672, 214
Galliano, F., Hony, S., Bernard, J.-P., et al. 2011, A&A, 536, A88
Gavazzi, G., Pierini, D., & Boselli, A. 1996, A&A, 312, 397
Giovannoli, E., Buat, V., Noll, S., Burgarella, D., & Magnelli, B. 2011, A&A, 525, A150
Gordon, K. D., Engelbracht, C. W., Fadda, D., et al. 2007, PASP, 119, 1019
Gordon, K. D., Engelbracht, C. W., Rieke, G. H., et al. 2008, ApJ, 682, 336
Gordon, K. D., Galliano, F., Hony, S., et al. 2010, A&A, 518, L89
Groves, B., Krause, O., Sandstrom, K., et al. 2012, MNRAS, 426, 892
Haynes, M. P., Magri, C. A., & Giovanelli, R. 1984, in BAAS 16, 882
Heinis, S., Buat, V., Béthermin, M., et al. 2014, MNRAS, 437, 1268
Helou, G. 1986, ApJ, 311, L33
Helou, G., Roussel, H., Appleton, P., et al. 2004, ApJS, 154, 253
Holland, W. S., Robson, E. I., Gear, W. K., et al. 1999, MNRAS, 303, 659
Hollenbach, D. J., & Tielens, A. G. G. M. 1997, ARA&A, 35, 179
Hughes, T. M., Cortese, L., Boselli, A., Gavazzi, G., & Davies, J. I. 2013, A&A, 550, A115
Jarrett, T. H., Cohen, M., Masci, F., et al. 2011, ApJ, 735, 112
Jarrett, T. H., Masci, F., Tsai, C. W., et al. 2013, AJ, 145, 6
Kennicutt, Jr., R. C. 1990, in The Interstellar Medium in Galaxies, eds. H. A. Thronson, Jr., & J. M. Shull, Astrophys. Space Sci. Lib., 161, 405
Kennicutt, Jr., R. C. 1998, ARA&A, 36, 189
Kennicutt, R. C., & Evans, N. J. 2012, ARA&A, 50, 531
Kennicutt, Jr., R. C., Armus, L., Bendo, G., et al. 2003, PASP, 115, 928
Kennicutt, Jr., R. C., Hao, C.-N., Calzetti, D., et al. 2009, ApJ, 703, 1672
Kennicutt, R. C., Calzetti, D., Aniano, G., et al. 2011, PASP, 123, 1347
Kessler, M. F., Steinz, J. A., Anderegg, M. E., et al. 1996, A&A, 315, L27
Kim, S.-H., Martin, P. G., & Hendry, P. D. 1994, ApJ, 422, 164
Komugi, S., Tosaki, T., Kohno, K., et al. 2011, PASJ, 63, 1139
Leitherer, C., Schaerer, D., Goldader, J. D., et al. 1999, ApJS, 123, 3
Li, A., & Draine, B. T. 2001, ApJ, 554, 778
Li, A., & Draine, B. T. 2002, ApJ, 572, 232
MacLachlan, J. M., Matthews, L. D., Wood, K., & Gallagher, J. S. 2011, ApJ, 741, 6
Madden, S. C., Galliano, F., Jones, A. P., & Sauvage, M. 2006, A&A, 446, 877
Magdis, G. E., Daddi, E., Béthermin, M., et al. 2012, ApJ, 760, 6
Maraston, C. 2005, MNRAS, 362, 799
Mathis, J. S., Rumpl, W., & Nordsieck, K. H. 1977, ApJ, 217, 425
Meny, C., Gromov, V., Boudet, N., et al. 2007, A&A, 468, 171
Moshir, M., et al. 1990, in IRAS Faint Source Catalogue, version 2.0
Murakami, H. 2008, in 37th COSPAR Scientific Assembly, 37, 2141

Neugebauer, G., Habing, H. J., van Duinen, R., et al. 1984, ApJ, 278, L1
Noll, S., Burgarella, D., Giovannoli, E., et al. 2009, A&A, 507, 1793
Panuzzo, P., Vega, O., Bressan, A., et al. 2007, ApJ, 656, 206
Peng, Y.-j., Lilly, S. J., Kovač, K., et al. 2010, ApJ, 721, 193
Pérez-González, P. G., Kennicutt, Jr., R. C., Gordon, K. D., et al. 2006, ApJ, 648, 987
Pilbratt, G. L., Riedinger, J. R., Passvogel, T., et al. 2010, A&A, 518, L1
Popescu, C. C., Misiriotis, A., Kylafis, N. D., Tuffs, R. J., & Fischera, J. 2000, A&A, 362, 138
Popescu, C. C., Tuffs, R. J., Dopita, M. A., et al. 2011, A&A, 527, A109
Reach, W. T., Dwek, E., Fixsen, D. J., et al. 1995, ApJ, 451, 188
Rémy-Ruyer, A., Madden, S. C., Galliano, F., et al. 2013, A&A, 557, A95
Rieke, G. H., Alonso-Herrero, A., Weiner, B. J., et al. 2009, ApJ, 692, 556
Rodighiero, G., Daddi, E., Baronchelli, I., et al. 2011, ApJ, 739, L40
Roussel, H. 2013, PASP, 125, 1126
Sanders, D. B., Mazzarella, J. M., Kim, D.-C., Surace, J. A., & Soifer, B. T. 2003, AJ, 126, 1607
Sandstrom, K. M., Bolatto, A. D., Bot, C., et al. 2012, ApJ, 744, 20
Sauvage, M., & Thuan, T. X. 1994, ApJ, 429, 153
Scalo, J. M. 1986, Fund. Cosmic Phys., 11, 1
Schlegel, D. J., Finkbeiner, D. P., & Davis, M. 1998, ApJ, 500, 525
Scoville, N., & Young, J. S. 1983, ApJ, 265, 148
Siebenmorgen, R., & Kruegel, E. 1992, A&A, 259, 614
Smith, J. D. T., Draine, B. T., Dale, D. A., et al. 2007, ApJ, 656, 770
Smith, D. J. B., Dunne, L., da Cunha, E., et al. 2012a, MNRAS, 427, 703
Smith, M. W. L., Gomez, H. L., Eales, S. A., et al. 2012b, ApJ, 748, 123
Soifer, B. T., Boehmer, L., Neugebauer, G., & Sanders, D. B. 1989, AJ, 98, 766
Thuan, T. X., & Sauvage, M. 1992, A&AS, 92, 749
Totani, T., Takeuchi, T. T., Nagashima, M., Kobayashi, M. A. R., & Makiya, R. 2011, PASJ, 63, 1181
Tremonti, C. A., Heckman, T. M., Kauffmann, G., et al. 2004, ApJ, 613, 898
Weingartner, J. C., & Draine, B. T. 2001, ApJ, 548, 296
Werner, M. W., Roellig, T. L., Low, F. J., et al. 2004, ApJS, 154, 1
Willmer, C. N. A., Rieke, G. H., Le Floc'h, E., et al. 2009, AJ, 138, 146
Wolfire, M. G., Hollenbach, D., McKee, C. F., Tielens, A. G. G. M., & Bakes, E. L. O. 1995, ApJ, 443, 152
Wright, E. L., Eisenhardt, P. R. M., Mainzer, A. K., et al. 2010, AJ, 140, 1868
Wu, H., Cao, C., Hao, C.-N., et al. 2005, ApJ, 632, L79
Xilouris, E. M., Byun, Y. I., Kylafis, N. D., Paleologou, E. V., & Papamastorakis, J. 1999, A&A, 344, 868
Xu, C., & Helou, G. 1996, ApJ, 456, 163
Young, J. S., Allen, L., Kenney, J. D. P., Lesser, A., & Rownd, B. 1996, AJ, 112, 1903
Zhu, Y.-N., Wu, H., Cao, C., & Li, H.-N. 2008, ApJ, 686, 155

Table 4. Estimated parameters.

HRS	CGCG	VCC	UGC	NGC	IC	Type	U_{min}	q_{PAH} (%)	γ (%)	$\log(L_{IR}/L_\odot)$	$\log(M_{dust}/M_\odot)$
2	124004	–	5588	–	–	Sb	5.80 ± 1.45	4.53 ± 0.18	0.51 ± 0.39	9.20 ± 0.02	6.25 ± 0.08
8	154020	–	5685	3254	–	Sbc	0.38 ± 0.10	4.46 ± 0.30	0.40 ± 0.29	9.25 ± 0.04	7.50 ± 0.09
10	183028	–	5738	–	–	Sb	2.60 ± 1.33	4.39 ± 0.35	1.39 ± 1.42	8.94 ± 0.04	6.29 ± 0.15
11	124038	–	5742	3287	–	Sd	2.09 ± 0.40	4.47 ± 0.25	0.66 ± 0.50	9.49 ± 0.02	6.97 ± 0.05
12	124041	–	–	–	–	BCD	3.52 ± 1.34	3.10 ± 0.97	1.00 ± 1.13	8.52 ± 0.05	5.77 ± 0.10
13	183030	–	5753	3294	–	Sc	3.37 ± 0.49	4.58 ± 0.01	0.45 ± 0.31	10.27 ± 0.01	7.57 ± 0.04
15	65087	–	5826	3338	–	Sc	1.18 ± 0.25	4.56 ± 0.11	0.35 ± 0.21	9.92 ± 0.02	7.67 ± 0.08
16	94116	–	5842	3346	–	Scd	1.09 ± 0.27	4.16 ± 0.60	0.80 ± 0.73	9.53 ± 0.04	7.26 ± 0.07
17	95019	–	5887	3370	–	Sc	2.42 ± 0.41	4.53 ± 0.18	0.63 ± 0.34	9.78 ± 0.02	7.19 ± 0.05
19	184016	–	5909	3381	–	pec	2.17 ± 0.71	4.31 ± 0.39	0.80 ± 0.75	9.57 ± 0.03	7.02 ± 0.10
20	184018	–	5931	3395	2613	Scd	4.03 ± 0.82	1.22 ± 0.24	4.38 ± 0.87	10.17 ± 0.03	7.26 ± 0.04
23	184028	–	5972	3424	–	Sb	3.66 ± 0.67	4.17 ± 0.33	0.97 ± 0.45	10.12 ± 0.03	7.37 ± 0.04
24	184029	–	5982	3430	–	Sc	2.02 ± 0.36	4.57 ± 0.09	0.51 ± 0.28	10.02 ± 0.02	7.52 ± 0.06
25	125013	–	5995	3437	–	Sc	5.54 ± 1.35	4.20 ± 0.43	1.76 ± 0.60	10.10 ± 0.04	7.12 ± 0.05
26	184031	–	5990	–	–	Sab	1.86 ± 0.84	3.56 ± 0.83	0.84 ± 1.03	8.77 ± 0.06	6.32 ± 0.14
27	184034	–	6001	3442	–	Sa	7.38 ± 1.53	4.53 ± 0.17	0.89 ± 0.58	9.60 ± 0.03	6.53 ± 0.07
28	155035	–	6023	3451	–	Sd	2.38 ± 0.46	4.47 ± 0.26	1.08 ± 0.66	9.39 ± 0.02	6.79 ± 0.06
29	95060	–	6026	3454	–	Sc	1.43 ± 0.50	4.04 ± 0.57	0.60 ± 0.58	8.98 ± 0.04	6.63 ± 0.11
30	95062	–	6028	3455	–	Sb	1.33 ± 0.53	4.02 ± 0.60	0.71 ± 0.77	9.07 ± 0.04	6.75 ± 0.12
31	267027	–	6024	3448	–	pec	3.20 ± 1.00	2.67 ± 0.34	2.54 ± 0.74	9.86 ± 0.04	7.09 ± 0.10
33	95085	–	6077	3485	–	Sb	2.16 ± 0.34	4.57 ± 0.09	0.62 ± 0.28	9.57 ± 0.02	7.01 ± 0.05
34	95097	–	6116	3501	–	Scd	1.28 ± 0.28	4.50 ± 0.22	0.27 ± 0.19	9.39 ± 0.03	7.10 ± 0.06
37	155051	–	6128	3512	–	Sc	3.32 ± 0.59	4.58 ± 0.03	0.34 ± 0.20	9.47 ± 0.02	6.76 ± 0.07
38	38129	–	6167	3526	–	Sc	1.21 ± 0.55	3.33 ± 0.86	1.04 ± 1.09	9.02 ± 0.07	6.74 ± 0.12
39	66115	–	6169	–	–	Sb	1.09 ± 0.52	4.21 ± 0.49	0.64 ± 0.71	8.89 ± 0.06	6.68 ± 0.13
40	67019	–	6209	3547	–	Sb	4.17 ± 1.01	4.09 ± 0.45	0.59 ± 0.43	9.55 ± 0.04	6.72 ± 0.06
41	96011	–	6267	3592	–	Sc	1.01 ± 0.35	4.13 ± 0.48	0.31 ± 0.25	8.79 ± 0.05	6.63 ± 0.09
42	96013	–	6277	3596	–	Sc	2.61 ± 0.55	4.50 ± 0.22	0.27 ± 0.17	9.86 ± 0.03	7.28 ± 0.08
44	96026	–	6320	–	–	Sb	3.08 ± 1.14	2.56 ± 0.52	3.13 ± 1.14	9.00 ± 0.05	6.23 ± 0.10
47	156064	–	6352	3629	–	Scd	1.47 ± 0.79	3.77 ± 0.67	0.64 ± 0.70	9.24 ± 0.07	6.91 ± 0.15
48	268021	–	6360	3631	–	Sc	4.14 ± 0.61	4.58 ± 0.01	0.25 ± 0.14	10.26 ± 0.01	7.47 ± 0.06
50	96037	–	6396	3655	–	Sc	7.57 ± 0.50	4.58 ± 0.01	0.27 ± 0.16	10.28 ± 0.00	7.23 ± 0.03
51	96038	–	6405	3659	–	Sm	2.45 ± 0.44	4.52 ± 0.20	0.34 ± 0.21	9.42 ± 0.02	6.83 ± 0.07
52	268030	–	6406	3657	–	Sc	3.38 ± 1.15	4.32 ± 0.38	0.33 ± 0.28	8.74 ± 0.04	6.02 ± 0.12
53	67071	–	6420	3666	–	Sc	2.36 ± 0.31	4.57 ± 0.09	0.23 ± 0.13	9.55 ± 0.01	6.99 ± 0.06
54	96045	–	6445	3681	–	Sbc	1.75 ± 0.37	4.50 ± 0.22	0.24 ± 0.14	9.15 ± 0.02	6.73 ± 0.08
55	96047	–	6453	3684	–	Sbc	2.23 ± 0.47	4.56 ± 0.11	0.69 ± 0.50	9.62 ± 0.02	7.08 ± 0.06
56	291072	–	6458	3683	–	Sc	7.92 ± 0.48	4.58 ± 0.01	0.47 ± 0.16	10.55 ± 0.01	7.46 ± 0.03
59	67084	–	6474	3692	–	Sb	1.30 ± 0.34	4.38 ± 0.35	0.46 ± 0.40	9.60 ± 0.03	7.29 ± 0.08
60	268051	–	6547	3729	–	Sa	2.45 ± 0.43	4.55 ± 0.14	1.74 ± 0.54	9.57 ± 0.02	6.93 ± 0.05
61	292009	–	6575	–	–	Scd	1.26 ± 0.62	2.90 ± 0.99	0.99 ± 1.19	8.54 ± 0.06	6.25 ± 0.15
62	186012	–	6577	3755	–	Sc	0.54 ± 0.39	2.26 ± 1.37	10.30 ± 15.12	9.37 ± 0.14	7.26 ± 0.15
63	268063	–	6579	3756	–	Sbc	0.86 ± 0.22	4.55 ± 0.14	1.22 ± 0.89	9.66 ± 0.02	7.49 ± 0.08
64	292017	–	6629	3795	–	Sc	0.84 ± 0.30	4.31 ± 0.41	0.73 ± 0.88	8.80 ± 0.04	6.69 ± 0.13
65	292019	–	6640	3794	–	Sd	1.40 ± 0.75	3.23 ± 0.81	0.55 ± 0.64	9.02 ± 0.08	6.73 ± 0.17
66	186024	–	6651	3813	–	Sb	5.01 ± 0.17	4.58 ± 0.01	0.60 ± 0.11	10.24 ± 0.01	7.36 ± 0.01
67	268076	–	6706	3846	–	Sm	0.97 ± 0.57	2.93 ± 1.00	1.27 ± 1.61	8.81 ± 0.07	6.66 ± 0.19
68	186045	–	–	–	–	Sb	8.58 ± 1.95	4.46 ± 0.27	2.23 ± 1.10	9.10 ± 0.03	5.90 ± 0.05
69	268088	–	6787	3898	–	Sab	0.47 ± 0.23	3.88 ± 0.88	1.05 ± 1.36	9.06 ± 0.05	7.23 ± 0.15
70	–	–	–	–	2969	Sbc	1.96 ± 0.71	3.34 ± 0.75	1.04 ± 0.87	9.17 ± 0.05	6.67 ± 0.10
72	–	–	–	3952	2972	Im(Im/S)	4.81 ± 3.06	1.76 ± 0.90	7.30 ± 7.28	9.37 ± 0.05	6.35 ± 0.17
73	269013	–	6870	3953	–	Sbc	1.26 ± 0.20	4.58 ± 0.03	0.38 ± 0.21	10.13 ± 0.02	7.82 ± 0.07
74	269019	–	6918	3982	–	Sb	4.98 ± 0.84	4.58 ± 0.03	1.16 ± 0.39	9.88 ± 0.02	6.96 ± 0.05
75	269020	–	6919	–	–	Sdm−Sd/S	0.34 ± 0.25	2.63 ± 1.36	6.16 ± 8.61	8.24 ± 0.11	6.43 ± 0.17
76	269022	–	6923	–	–	Im(Im/S)	1.22 ± 0.72	2.29 ± 1.13	1.54 ± 1.93	8.49 ± 0.07	6.22 ± 0.18
77	13033	–	6993	4030	–	Sbc	2.81 ± 0.25	4.58 ± 0.00	0.56 ± 0.23	10.63 ± 0.02	7.98 ± 0.03
78	98019	–	6995	4032	–	Im(Im/S)	1.45 ± 0.56	4.13 ± 0.49	0.61 ± 0.61	9.06 ± 0.03	6.70 ± 0.13
79	69024	–	7001	4019	755	Sb	2.23 ± 2.14	2.42 ± 1.02	2.70 ± 3.95	8.97 ± 0.08	6.44 ± 0.27
81	13046	–	7021	4045	–	Sa	2.79 ± 0.44	3.27 ± 0.27	1.94 ± 0.37	9.87 ± 0.03	7.18 ± 0.04
84	69036	–	7048	4067	–	Sb	2.56 ± 0.56	4.52 ± 0.20	0.74 ± 0.61	9.03 ± 0.03	6.42 ± 0.06
85	243044	–	7095	4100	–	Sbc	2.73 ± 0.38	4.55 ± 0.15	0.75 ± 0.30	10.02 ± 0.02	7.37 ± 0.04
86	41041	–	7111	4116	–	Sdm−Sd/S	1.08 ± 0.39	4.01 ± 0.53	0.74 ± 0.48	9.47 ± 0.05	7.22 ± 0.10
88	41042	–	7116	4123	–	Sc	1.06 ± 0.67	2.93 ± 1.02	12.81 ± 10.82	9.88 ± 0.04	7.40 ± 0.16
89	69088	66	7215	4178	–	Sdm−Sd/S	0.75 ± 0.17	4.00 ± 0.61	1.04 ± 0.50	9.68 ± 0.03	7.58 ± 0.07
91	98108	92	7231	4192	–	Sab	1.48 ± 0.22	4.58 ± 0.01	0.35 ± 0.18	10.22 ± 0.01	7.85 ± 0.06
92	69101	131	7255	–	3061	Sc	1.37 ± 0.47	4.17 ± 0.49	0.45 ± 0.42	8.93 ± 0.04	6.61 ± 0.10
94	69104	145	7260	4206	–	Sbc	0.51 ± 0.19	3.85 ± 0.78	0.80 ± 0.85	9.19 ± 0.05	7.29 ± 0.10
95	69107	152	7268	4207	–	Scd	5.98 ± 1.08	4.51 ± 0.20	0.30 ± 0.15	9.60 ± 0.03	6.65 ± 0.06
96	69110	157	7275	4212	–	Sc	3.11 ± 0.39	4.58 ± 0.00	0.77 ± 0.33	10.04 ± 0.01	7.34 ± 0.04
98	69119	187	7291	4222	–	Sc	0.89 ± 0.23	3.76 ± 0.77	0.81 ± 0.64	9.23 ± 0.04	7.07 ± 0.07
102	98144	307	7345	4254	–	Sc	4.49 ± 0.50	4.58 ± 0.00	0.73 ± 0.30	10.83 ± 0.01	7.97 ± 0.04
107	42033	404	7387	–	–	Sd	0.73 ± 0.45	2.55 ± 1.37	7.90 ± 14.05	8.81 ± 0.11	6.56 ± 0.14
109	42038	449	7403	4289	–	Scd	1.09 ± 0.35	3.96 ± 0.61	0.55 ± 0.55	9.07 ± 0.05	6.84 ± 0.09

Table 4. continued.

HRS	CGCG	VCC	UGC	NGC	IC	Type	$U_{\min}$	q_{PAH} (%)	γ (%)	$\log(L_{\mathrm{IR}}/L_\odot)$	$\log(M_{\mathrm{dust}}/M_\odot)$
110	70024	465	7407	4294	–	Scd	2.02 ± 0.52	3.01 ± 0.68	1.09 ± 0.44	9.47 ± 0.03	6.93 ± 0.08
111	99024	483	7412	4298	–	Sc	2.08 ± 0.19	4.58 ± 0.01	0.43 ± 0.18	9.90 ± 0.02	7.41 ± 0.02
114	42045	508	7420	4303	–	Sbc	4.53 ± 0.55	4.58 ± 0.04	0.47 ± 0.26	10.75 ± 0.02	7.89 ± 0.03
121	70035	576	7447	4316	–	Sbc	1.78 ± 0.27	4.54 ± 0.16	0.32 ± 0.23	9.72 ± 0.02	7.29 ± 0.05
122	99030	596	7450	4321	–	Sbc	2.47 ± 0.35	4.58 ± 0.00	0.65 ± 0.28	10.72 ± 0.01	8.12 ± 0.06
132	42080	699	7477	–	3268	pec	2.35 ± 1.26	3.04 ± 1.01	1.28 ± 1.70	9.08 ± 0.06	6.52 ± 0.16
133	158099	–	7483	4359	–	Sc	0.40 ± 0.27	3.07 ± 1.15	1.63 ± 1.75	8.89 ± 0.08	7.14 ± 0.16
139	42093	787	7498	4376	–	Im(Im/S)	1.91 ± 0.53	2.94 ± 1.20	0.49 ± 0.36	9.12 ± 0.04	6.65 ± 0.09
140	42092	785	7497	4378	–	Sa	0.45 ± 0.20	3.00 ± 1.32	0.89 ± 0.74	8.99 ± 0.07	7.17 ± 0.15
142	99044	801	7507	4383	–	Sa	5.53 ± 1.37	3.39 ± 0.37	4.10 ± 1.05	9.84 ± 0.03	6.80 ± 0.06
143	42095	827	7513	–	–	Scd	1.43 ± 0.24	4.33 ± 0.40	0.32 ± 0.20	9.71 ± 0.02	7.35 ± 0.05
145	70067	849	7519	4390	–	Sbc	1.21 ± 0.32	4.00 ± 0.57	0.61 ± 0.38	9.29 ± 0.03	6.99 ± 0.10
146	42098	851	7518	–	3322	Scd	1.40 ± 0.27	4.11 ± 0.55	0.29 ± 0.19	9.27 ± 0.03	6.94 ± 0.06
148	99049	865	7526	4396	–	Sd	0.95 ± 0.23	3.74 ± 0.57	0.52 ± 0.32	9.30 ± 0.04	7.12 ± 0.08
151	70076	912	7538	4413	–	Sab	1.55 ± 0.45	4.47 ± 0.26	1.19 ± 0.51	9.23 ± 0.02	6.80 ± 0.10
154	70082	939	7546	–	–	Scd	0.80 ± 0.22	3.24 ± 0.67	0.49 ± 0.29	9.25 ± 0.03	7.16 ± 0.12
157	42106	957	7549	4420	–	Sbc	3.21 ± 0.56	4.53 ± 0.19	0.44 ± 0.26	9.55 ± 0.03	6.84 ± 0.05
168	70108	1091	7590	–	–	Sbc	1.94 ± 0.67	2.39 ± 1.22	0.95 ± 0.59	8.87 ± 0.04	6.37 ± 0.11
169	99063	–	7595	–	3391	Scd	1.57 ± 0.61	4.16 ± 0.55	0.78 ± 0.86	9.18 ± 0.04	6.77 ± 0.11
177	42132	1205	7627	4470	–	Sa	3.31 ± 0.62	4.26 ± 0.45	0.45 ± 0.29	9.32 ± 0.03	6.62 ± 0.05
182	42139	1290	7647	4480	–	Sc	1.70 ± 0.45	3.39 ± 1.08	0.76 ± 0.73	9.31 ± 0.04	6.88 ± 0.06
187	42144	1375	7668	4505	–	Sm	1.40 ± 0.46	3.05 ± 0.45	1.64 ± 0.60	9.74 ± 0.04	7.35 ± 0.10
188	99075	1379	7669	4498	–	Sd	1.25 ± 0.24	4.34 ± 0.37	0.31 ± 0.20	9.33 ± 0.03	7.05 ± 0.06
194	14063	–	7694	4517	–	Scd	0.72 ± 0.10	4.33 ± 0.40	0.67 ± 0.32	10.19 ± 0.02	8.12 ± 0.04
196	70167	1508	7709	4519	–	Sd	2.09 ± 0.66	3.61 ± 0.67	3.00 ± 0.95	9.66 ± 0.03	7.04 ± 0.10
198	159016	–	7714	4525	–	Scd	0.60 ± 0.25	4.39 ± 0.35	1.13 ± 1.17	8.88 ± 0.03	6.91 ± 0.12
201	42156	1540	7721	4527	–	Sbc	3.94 ± 0.25	4.58 ± 0.01	0.68 ± 0.19	10.65 ± 0.01	7.84 ± 0.01
203	42158	1554	7726	4532	–	Im(Im/S)	3.21 ± 0.70	2.43 ± 0.35	2.96 ± 0.71	9.85 ± 0.03	7.07 ± 0.05
205	14068	1562	7732	4536	–	Sbc	2.58 ± 0.48	4.16 ± 0.42	3.29 ± 0.87	10.45 ± 0.02	7.72 ± 0.05
212	99098	–	7768	4561	–	Sdm−Sd/S	2.45 ± 0.76	2.44 ± 0.65	1.06 ± 0.45	9.19 ± 0.04	6.59 ± 0.11
213	129010	–	7772	4565	–	Sb	0.85 ± 0.11	4.58 ± 0.01	0.27 ± 0.13	10.49 ± 0.02	8.38 ± 0.04
227	14091	–	7819	4592	–	Sdm−Sd/S	0.85 ± 0.34	2.86 ± 0.85	0.90 ± 0.54	9.24 ± 0.06	7.11 ± 0.13
237	42208	1923	7871	4630	–	Im(Im/S)	2.82 ± 0.84	4.33 ± 0.34	1.66 ± 0.61	9.48 ± 0.04	6.79 ± 0.09
238	14109	–	7869	4629	–	Sm	2.01 ± 2.48	2.15 ± 1.27	4.03 ± 7.66	8.25 ± 0.18	5.95 ± 0.28
242	70230	1943	7884	4639	–	Sbc	1.99 ± 0.60	3.95 ± 0.59	0.30 ± 0.20	9.42 ± 0.04	6.96 ± 0.10
246	100004	–	7901	4651	–	Sc	2.03 ± 0.40	4.44 ± 0.30	0.40 ± 0.24	9.93 ± 0.03	7.44 ± 0.06
247	71019	1987	7902	4654	–	Scd	2.56 ± 0.32	4.58 ± 0.03	0.84 ± 0.34	10.35 ± 0.02	7.72 ± 0.04
251	15015	–	7926	4666	–	Sc	5.01 ± 0.12	4.58 ± 0.00	0.54 ± 0.10	10.94 ± 0.01	8.07 ± 0.01
252	15016	–	7931	4668	–	Sd	0.58 ± 0.41	1.45 ± 0.78	14.72 ± 7.34	9.22 ± 0.19	7.02 ± 0.19
257	71045	2070	7970	4698	–	Sab	0.34 ± 0.11	3.69 ± 1.00	0.69 ± 0.52	9.15 ± 0.04	7.42 ± 0.13
259	43034	–	7975	4701	–	Scd	1.73 ± 0.86	3.69 ± 0.76	1.02 ± 0.86	9.47 ± 0.07	7.04 ± 0.14
262	43041	–	7985	4713	–	Sd	2.50 ± 0.79	4.03 ± 0.48	0.74 ± 0.59	9.72 ± 0.05	7.11 ± 0.09
263	129027	–	7989	4725	–	Sab	0.52 ± 0.15	4.43 ± 0.33	0.39 ± 0.25	10.12 ± 0.02	8.22 ± 0.12
266	–	–	–	4731	–	Scd	0.75 ± 0.39	3.34 ± 1.06	1.63 ± 2.36	9.77 ± 0.07	7.70 ± 0.16
267	129028	–	8005	4747	–	Scd	1.33 ± 0.74	3.63 ± 0.69	2.17 ± 2.18	9.36 ± 0.07	6.99 ± 0.15
268	71060	–	8007	4746	–	Sb	3.54 ± 0.65	4.48 ± 0.24	0.73 ± 0.45	9.77 ± 0.03	7.01 ± 0.04
271	100015	–	8014	4758	–	Im(Im/S)	0.99 ± 0.35	3.77 ± 0.69	0.96 ± 0.99	9.17 ± 0.04	6.97 ± 0.11
274	15032	–	8021	4772	–	Sa	0.69 ± 0.17	3.25 ± 1.25	0.39 ± 0.33	8.93 ± 0.04	6.93 ± 0.09
275	–	–	–	4775	–	Sd	2.93 ± 0.76	4.16 ± 0.47	0.75 ± 0.67	9.90 ± 0.04	7.22 ± 0.07
279	15037	–	8041	–	–	Sd	0.54 ± 0.23	3.52 ± 0.78	0.88 ± 0.57	9.06 ± 0.06	7.15 ± 0.14
281	43068	–	8045	–	–	Im(Im/S)	1.64 ± 0.87	4.04 ± 0.65	1.22 ± 1.45	8.42 ± 0.06	5.99 ± 0.14
283	43071	–	8054	4808	–	Scd	3.08 ± 0.48	4.57 ± 0.07	0.82 ± 0.40	9.91 ± 0.02	7.20 ± 0.04
284	–	–	–	–	3908	Sd	6.22 ± 1.20	4.25 ± 0.34	0.66 ± 0.43	10.03 ± 0.03	7.04 ± 0.03
287	15055	–	8121	4904	–	Scd	2.48 ± 0.59	4.43 ± 0.30	0.97 ± 0.71	9.58 ± 0.03	6.96 ± 0.06
289	–	–	–	4981	–	Sbc	2.55 ± 0.44	4.52 ± 0.20	0.77 ± 0.51	10.11 ± 0.03	7.49 ± 0.04
290	189037	–	8271	5014	–	Sa	6.78 ± 1.95	4.01 ± 0.47	1.26 ± 0.82	9.29 ± 0.04	6.27 ± 0.08
292	218010	–	8439	5145	–	Sb	7.36 ± 0.54	4.58 ± 0.04	0.50 ± 0.25	9.90 ± 0.01	6.82 ± 0.03
293	16069	–	8443	5147	–	Sdm−Sd/S	2.32 ± 0.44	4.31 ± 0.34	0.65 ± 0.36	9.45 ± 0.02	6.89 ± 0.06
295	73054	–	8616	5248	–	Sbc	3.28 ± 0.53	4.58 ± 0.00	0.60 ± 0.34	10.52 ± 0.02	7.79 ± 0.05
297	246023	–	8711	5301	–	Sbc	1.36 ± 0.26	4.53 ± 0.18	0.45 ± 0.32	9.87 ± 0.03	7.54 ± 0.05
298	218047	–	8725	5303	–	pec	6.49 ± 1.17	4.57 ± 0.08	1.14 ± 0.48	9.69 ± 0.02	6.67 ± 0.06
299	45108	–	8727	5300	–	Sc	0.69 ± 0.28	4.10 ± 0.64	1.01 ± 1.11	9.35 ± 0.04	7.31 ± 0.13
301	17088	–	8790	5334	4338	Sc	0.50 ± 0.22	4.06 ± 0.67	1.01 ± 1.18	9.44 ± 0.05	7.57 ± 0.13
302	45137	–	8821	5348	–	Sbc	0.61 ± 0.26	3.62 ± 0.80	0.64 ± 0.77	8.94 ± 0.07	7.02 ± 0.13
309	272031	–	9036	5486	–	Sm	1.25 ± 0.61	2.68 ± 1.15	1.67 ± 1.73	8.82 ± 0.06	6.48 ± 0.14
314	19012	–	9215	–	–	Sd	1.06 ± 0.46	3.21 ± 1.05	1.73 ± 1.71	9.23 ± 0.05	6.96 ± 0.12
317	47066	–	9311	–	1022	Sb	1.01 ± 0.83	4.07 ± 0.66	1.37 ± 1.62	8.56 ± 0.06	6.41 ± 0.22
318	47070	–	9328	5645	–	Sd	1.87 ± 0.58	3.18 ± 0.88	0.79 ± 0.76	9.47 ± 0.04	7.00 ± 0.09
319	75064	–	9353	5669	–	Scd	1.10 ± 0.29	3.33 ± 0.66	0.71 ± 0.38	9.57 ± 0.04	7.32 ± 0.10
320	47090	–	9363	5668	–	Sd	1.15 ± 0.32	3.89 ± 0.56	0.51 ± 0.33	9.83 ± 0.04	7.56 ± 0.10
321	47123	–	9427	5692	–	Sb	4.99 ± 0.66	4.58 ± 0.02	0.68 ± 0.28	9.45 ± 0.01	6.54 ± 0.04
322	47127	–	9436	5701	–	Sa	0.26 ± 0.15	2.86 ± 1.35	1.36 ± 1.58	9.09 ± 0.06	7.50 ± 0.16
323	48004	–	9483	–	1048	Sb	2.08 ± 0.22	4.57 ± 0.08	0.23 ± 0.11	9.72 ± 0.02	7.20 ± 0.03

Table A.1. Statistics of the MIR photometry from IRAC and WISE.

	Spitzer/IRAC 8 μm	WISE 12 μm	WISE 22 μm
Number of galaxies	129	323	323
Detections	91%	96%	86%
Mean error	15%	6%	13%

Appendix A: MIR photometry of the HRS

For the purpose of this study, we perform MIR photometry at 8, 12, and 22 μm from *Spitzer*/IRAC and WISE data. We thus present here the flux densities at these wavelengths for all of the HRS galaxies.

A.1. Spitzer/IRAC 8 μm

One of the output results from Draine & Li (2007) models is the PAH fraction of the total dust mass of a galaxy. Because one of the largest PAH emission features is expected at 7.7 μm, we need the IRAC (Fazio et al. 2004) 8 μm images to constrain this part of the SED.

We retrieved 8 μm images available for 129 HRS galaxies from the *Spitzer* Data Archive[9]. The FWHM of the PSF of the IRAC fourth channel is 1.9″ and the maps have a pixel size of 0.6″. As a first step, we convert the images from MJy/sr to μJy/pixel, and then remove all of the problematic pixels (NaN) by replacing them by the median value of the surrounding pixels. We remove the stars and background sources visible at 8 μm using the `IRAF/imedit` task from all of the images. We then extract the flux densities using apertures adapted to each galaxies to take all of the IR emission into account, and minimize the contamination from background features. As the images have small fields of view, we do not estimate residual background emission from circular annuli (as we do for WISE and *Herschel*/SPIRE photometry) but from the mean value of multiple 10×10 pixels boxes around the galaxies. IRAC flux densities need to be corrected for aperture effects to take the diffuse scattering of incoming photons through the IRAC array[10] into account. We thus apply aperture corrections on our measurements using the parameters provided in Table 4 of Dale et al. (2007).

For the error calculation, we proceed as in Boselli et al. (2003b) using the same boxes as for the background residual estimation. We thus take two terms into account, one being the pixel-to-pixel error (the mean value of the standard deviation in all of the boxes) and the other one being the sky error due to large scale structures (the standard deviation of the mean values in all of the boxes). To this stochastic error, we add quadratically a calibration error of 10% as indicated in Dale et al. (2007). Galaxies with a signal-to-noise lower than 3 are considered as undetected, and an upper limit of 3σ is given.

In Table A.2, we give the IRAC 8 μm flux densities of the HRS galaxies. A flag is associated with the measurements with the following code: 0 for undetected galaxies, 1 for detected galaxies, and 2 for galaxies for which the measurement suffers from source blending.

To check the validity of our IRAC photometry, we search for IRAC 8 μm flux densities already available for HRS galaxies on
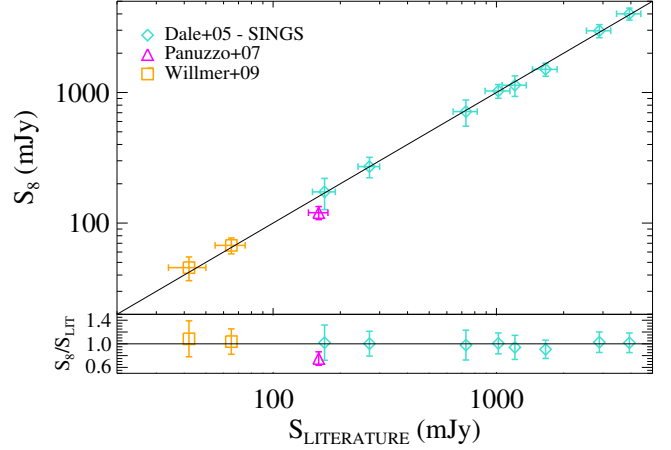
Fig. A.1. Comparison between our *Spitzer*/IRAC 8 μm flux density measurements and *Spitzer*/IRAC data from the literature. The one-to-one relationship is the solid black line. The ratios between the HRS IRAC 8 μm and the literature 8 μm flux densities are shown in the *lower panel*.

NED and make the comparison (Fig. A.1). We find eight galaxies in common with the SINGS sample (the *Spitzer* Infrared Nearby Galaxies Survey, Kennicutt et al. 2003; Dale et al. 2007), one galaxy in common with Panuzzo et al. (2007), and two galaxies to be compared with Willmer et al. (2009). The only point that deviates from the one-to-one relationship is the data point of Panuzzo et al. (2007). It corresponds to the flux density of NGC 4435, which is very close to NGC 4438. This proximity can be problematic as outlined by Panuzzo et al. (2007) and the difference in the measurement may come from how the emission from NGC 4438 is treated. This comparison shows that our measurements are consistent with the 8 μm data taken from the literature with a mean ratio of 0.93 ± 0.04.

A.2. WISE 12 and 22 μm

NASA's telescope WISE (Wright et al. 2010) performed an all sky survey in four NIR and MIR bands. For the purpose of this work, we use WISE data at 12 and 22 μm, observed with a resolution of 6.5″, and 12.0″, respectively. WISE scanned the sky with 8.8 s exposures at 12 and 22 μm (the W3 and W4 bands), each with a 47′ field of view, providing at least eight exposures per position on the ecliptic and increasing depth toward the ecliptic poles. The individual frames were combined into coadded images with a pixel size of 1.375″. WISE achieved 5σ point source sensitivities better than 1 and 6 mJy in unconfused regions on the ecliptic in the W3 and W4 bands. Sensitivity improves toward the ecliptic poles due to denser coverage and lower zodiacal background. We retrieve the images of all of the HRS galaxies at 12 and 22 μm from the WISE Science Archive[11]. We perform aperture photometry using the DS9/Funtools program "Funcnts". For each galaxy, the aperture, where the flux of the galaxy is estimated, and the background annulus, where the emission from the background is estimated, are defined "manually". They are chosen to encompass all of the emission from the galaxy and avoid any contamination from foreground/background sources.

To convert the counts extracted into Jy, we use the factors provided by the Explanatory Supplement to the WISE

---

[9] http://irsa.ipac.caltech.edu/data/SPITZER/docs/spitzerdataarchives/
[10] http://ssc.spitzer.caltech.edu/irac/calib/extcal/

[11] Science Archive: http://irsa.ipac.caltech.edu/

Table A.2. MIR photometry of the HRS galaxies.

HRS	CGCG	VCC	UGC	NGC	IC	Flag 8 μm	S_8 (mJy)	Flag 12 μm	S_{12} (mJy)	Flag 22 μm	S_{22} (mJy)	RA$_{ap}$	Dec$_{ap}$	a ('')	b ('')	PA (deg)
1	123035	–	–	–	–	0	–	1	29.47 ± 2.46	1	21.24 ± 3.56	154.41	22.81	47.9	40.1	260
2	124004	–	5588	–	–	0	–	1	89.90 ± 2.08	1	78.96 ± 7.19	155.24	25.36	40.1	37.4	130
3	94026	–	5617	3226	–	0	–	1	57.34 ± 2.01	1	42.69 ± 6.57	155.86	19.90	39.4	39.0	105
4	94028	–	5620	3227	–	1	628.01 ± 75.06	1	1145.72 ± 16.37	1	1823.09 ± 35.59	155.88	19.86	100.5	82.9	245
5	94052	–	–	–	610	0	–	1	114.02 ± 3.28	1	108.32 ± 10.98	156.62	20.23	62.8	38.2	118
6	154016	–	5662	3245	–	0	–	1	11.90 ± 2.30	1	12.32 ± 0.11	156.76	28.64	65.9	34.7	240
7	154017	–	5663	3245	–	1	103.19 ± 15.02	1	103.90 ± 3.21	1	192.48 ± 9.60	156.83	28.51	54.0	54.5	265
8	154020	–	5685	3254	–	1	110.65 ± 27.62	1	134.90 ± 7.67	1	100.72 ± 28.66	157.33	29.49	135.6	46.1	136
9	154026	–	5731	3277	–	0	–	1	92.18 ± 3.84	1	61.74 ± 12.48	158.23	28.51	56.9	55.4	115
10	183028	–	5738	–	–	0	–	1	40.00 ± 1.52	1	38.95 ± 4.88	158.62	35.26	43.3	33.5	120
11	124038	–	5742	3287	–	0	–	1	171.03 ± 4.46	1	158.96 ± 17.08	158.70	21.65	71.2	47.0	110
12	124041	–	–	–	–	0	–	1	12.44 ± 0.98	1	15.47 ± 4.05	158.93	26.13	35.7	29.1	110
13	183030	–	5753	3294	–	0	–	1	722.22 ± 5.67	1	671.16 ± 22.88	159.07	37.33	101.6	65.7	205
14	124045	–	5767	3301	–	0	–	1	38.07 ± 1.69	1	39.38 ± 5.01	159.23	21.88	37.4	35.3	145
15	65087	–	5826	3338	–	0	–	1	550.05 ± 21.26	1	417.85 ± 65.73	160.53	13.75	131.1	76.3	190
16	94116	–	5842	3346	–	0	–	1	257.84 ± 21.95	1	215.95 ± 34.43	160.91	14.87	84.2	73.9	198
17	95019	–	5887	3370	–	1	325.85 ± 34.60	1	377.74 ± 12.69	1	372.06 ± 18.61	161.77	17.27	79.0	59.5	240
18	155015	–	5906	3380	–	0	–	1	64.39 ± 2.10	1	55.91 ± 6.13	162.05	28.60	48.7	40.4	110
19	184016	–	5909	3381	–	1	119.30 ± 14.19	1	136.18 ± 15.41	1	133.80 ± 15.41	162.10	34.71	59.0	54.9	145
20	184018	–	5931	3395	2613	0	–	2	312.03 ± 5.32	2	458.75 ± 12.76	162.46	32.98	57.8	50.7	140
21	155028	–	5958	–	–	0	–	2	16.26 ± 1.44	1	8.54 ± 2.57	162.82	27.85	34.4	29.3	270
22	155029	–	5959	3414	–	1	57.57 ± 9.76	1	52.95 ± 3.02	1	33.06 ± 3.75	162.82	27.98	39.9	35.2	100
23	184028	–	5972	3424	–	1	496.51 ± 49.91	1	530.62 ± 5.31	1	686.93 ± 17.71	162.94	32.90	91.6	52.2	200
24	184029	–	5982	3430	–	1	372.70 ± 39.34	1	412.50 ± 9.27	1	385.90 ± 20.60	163.05	32.95	94.9	58.6	125
25	125013	–	5995	3437	–	1	637.14 ± 63.96	1	732.87 ± 27.04	1	998.25 ± 30.39	163.15	22.93	84.1	70.5	207
26	184031	–	5990	–	–	0	–	1	19.74 ± 1.47	1	17.20 ± 4.86	163.16	34.48	34.9	32.3	105
27	184034	–	6001	3442	–	0	–	1	131.34 ± 3.38	1	141.28 ± 8.24	163.28	33.91	55.6	47.6	268
28	155035	–	6023	3451	–	0	–	1	137.02 ± 3.39	1	148.24 ± 13.02	163.59	27.24	62.1	46.9	140
29	95060	–	6026	3454	–	0	–	1	70.40 ± 4.03	1	69.73 ± 9.14	163.62	17.34	60.5	38.8	205
30	95062	–	6028	3455	–	0	–	1	88.15 ± 5.22	1	80.88 ± 14.73	163.63	17.28	57.0	50.4	160
31	267027	–	6024	3448	–	1	205.46 ± 28.82	1	269.58 ± 4.45	1	535.31 ± 18.95	163.66	54.31	80.8	53.7	155
32	95065	–	6030	3457	–	0	–	1	14.12 ± 2.30	0	<18.07	163.70	17.62	38.2	38.2	180
33	95085	–	6077	3485	–	0	–	1	181.53 ± 5.24	1	165.91 ± 15.82	165.01	14.84	65.5	59.6	150
34	95097	–	6116	3501	–	1	171.80 ± 18.65	1	173.63 ± 3.52	1	129.93 ± 10.52	165.70	17.99	74.2	38.3	120
35	267037	–	6115	3499	–	1	15.97 ± 1.96	1	18.06 ± 0.64	1	7.31 ± 1.76	165.79	56.22	26.4	26.6	110
36	155049	–	6118	3504	–	1	876.32 ± 88.36	1	1320.21 ± 14.94	1	2981.28 ± 24.80	165.80	27.97	113.0	87.8	240
37	155051	–	6128	3512	–	1	145.32 ± 15.57	1	155.24 ± 2.90	1	131.40 ± 9.61	166.01	28.04	50.8	46.3	228
38	38129	–	6167	3526	–	0	–	1	41.72 ± 2.98	1	49.11 ± 7.79	166.74	7.17	49.5	35.8	145
39	66115	–	6169	–	–	0	–	1	31.24 ± 1.82	1	24.40 ± 4.10	166.76	12.06	41.8	32.2	270
40	67019	–	6209	3547	–	0	–	1	121.60 ± 4.09	1	138.01 ± 9.61	167.48	10.72	54.6	39.1	97
41	96011	–	6267	3592	–	0	–	1	32.45 ± 1.22	1	20.19 ± 3.57	168.62	17.26	35.7	25.3	207
42	96013	–	6277	3596	–	0	–	1	486.99 ± 11.72	1	426.93 ± 16.12	168.77	14.79	83.1	77.6	270
43	96022	–	6299	3608	–	0	<65.21	1	35.99 ± 2.05	0	<20.7	169.24	18.15	33.3	49.0	175
44	96026	–	6320	–	–	0	–	1	53.80 ± 1.87	1	112.48 ± 7.04	169.57	18.85	42.2	46.3	197
45	291054	–	6330	3619	–	0	–	1	87.58 ± 5.57	1	49.51 ± 8.25	169.84	57.76	51.0	44.1	115
46	96029	–	6343	3626	–	0	–	1	159.10 ± 4.18	1	165.43 ± 12.78	170.02	18.36	51.8	48.2	250
47	156064	–	6352	3629	–	0	–	1	60.58 ± 2.51	1	57.79 ± 11.57	170.13	26.96	51.9	47.9	155
48	268021	–	6360	3631	–	0	<165.60	1	1294.41 ± 18.17	1	1119.70 ± 32.82	170.26	53.17	141.5	130.8	208
49	39130	–	6368	3640	–	0	–	1	61.54 ± 3.57	1	30.16 ± 7.46	170.28	3.23	40.3	43.4	185
50	96037	–	6396	3655	–	1	695.99 ± 70.85	1	773.04 ± 6.39	1	755.28 ± 22.38	170.73	16.59	76.7	63.9	120
51	96038	–	6405	3659	–	1	130.83 ± 14.14	1	144.26 ± 3.41	1	128.90 ± 11.06	170.94	17.82	56.2	44.5	145
52	268030	–	6406	3657	–	0	–	1	40.93 ± 1.69	1	26.31 ± 2.67	170.98	52.92	39.7	38.0	250
53	67071	–	6420	3666	–	1	258.74 ± 31.41	1	293.81 ± 5.36	1	240.51 ± 16.30	171.11	11.34	79.4	48.6	185
54	96045	–	6445	3681	–	0	–	1	101.20 ± 3.65	1	68.98 ± 8.75	171.62	16.86	50.1	52.8	255

Table A.2. continued.

HRS	CGCG	VCC	UGC	NGC	IC	Flag 8 μm	S_8 (mJy)	Flag 12 μm	S_{12} (mJy)	Flag 22 μm	S_{22} (mJy)	RA$_{ap}$	Dec$_{ap}$	a (″)	b (″)	PA (deg)
55	96047	–	6453	3684	–	0	–	1	317.89 ± 8.41	1	267.68 ± 24.15	171.80	17.03	87.2	65.1	215
56	291072	–	6458	3683	–	1	1041.77 ± 104.20	1	1119.49 ± 7.12	1	1143.23 ± 23.61	171.88	56.88	82.3	64.9	218
57	96049	–	6460	3686	–	1	465.79 ± 49.42	1	566.00 ± 14.03	1	537.22 ± 18.94	171.93	17.22	95.6	79.1	115
58	96050	–	6464	3691	–	0	–	1	60.34 ± 3.23	1	53.52 ± 7.77	172.04	16.92	52.6	41.6	120
59	67084	–	6474	3692	–	0	–	1	135.72 ± 5.95	1	97.80 ± 14.75	172.10	9.41	80.8	42.6	185
60	268051	–	6547	3729	–	1	267.87 ± 30.22	1	361.47 ± 8.01	1	459.15 ± 18.84	173.46	53.13	88.7	72.3	105
61	292009	–	6575	–	–	0	–	1	16.57 ± 1.45	1	18.73 ± 4.67	174.11	58.19	53.4	26.5	81
62	186012	–	6577	3755	–	0	–	1	63.08 ± 16.37	0	<69.70	174.14	36.41	102.5	51.3	205
63	268063	–	6579	3756	–	0	–	1	310.17 ± 8.49	1	239.16 ± 36.62	174.20	54.29	111.5	74.0	269
64	292017	–	6629	3795	–	0	–	1	42.27 ± 1.65	1	28.35 ± 7.54	175.03	58.61	50.2	39.2	143
65	292019	–	6640	3794	–	1	39.51 ± 6.39	1	40.05 ± 3.13	1	39.55 ± 4.87	175.23	56.20	57.3	47.8	210
66	186024	–	6651	3813	–	0	–	1	772.40 ± 9.53	1	765.82 ± 19.38	175.33	36.55	96.9	68.1	175
67	268076	–	6706	3846	–	0	–	1	23.75 ± 2.01	1	28.99 ± 5.88	176.06	55.03	49.9	35.5	150
68	186045	–	–	–	–	0	–	1	65.84 ± 1.94	1	84.91 ± 7.10	176.61	34.85	41.2	40.1	155
69	268088	–	6787	3898	–	0	–	1	163.34 ± 13.39	1	92.28 ± 19.70	177.31	56.08	106.2	60.8	198
70	–	–	–	–	2969	0	–	1	42.77 ± 2.60	1	58.10 ± 6.12	178.13	-3.87	45.4	40.0	195
71	292042	–	6860	3945	–	1	124.18 ± 17.78	1	95.42 ± 7.33	1	46.52 ± 11.74	178.31	60.68	65.0	61.6	75
72	–	–	–	3952	2972	0	–	1	62.61 ± 5.30	1	183.15 ± 14.32	178.41	-4.00	57.3	49.8	169
73	269013	–	6870	3953	–	1	1140.01 ± 120.79	1	1490.57 ± 42.22	1	1177.57 ± 79.81	178.46	52.33	180.7	115.6	103
74	269019	–	6918	3982	–	0	–	1	627.85 ± 10.42	1	727.35 ± 22.11	179.12	55.12	84.0	74.3	128
75	269020	–	6919	–	–	0	–	1	10.48 ± 1.32	0	<16.49	179.16	55.63	41.8	30.9	180
76	269022	–	6923	–	–	0	–	1	17.28 ± 2.26	1	26.34 ± 5.62	179.21	53.16	40.5	37.2	260
77	13033	–	6993	4030	–	0	–	1	2004.48 ± 30.64	1	1876.06 ± 67.72	180.10	-1.10	125.2	103.7	121
78	98019	–	6995	4032	–	0	–	1	65.26 ± 2.77	1	61.28 ± 8.40	180.14	20.08	52.9	44.0	266
79	69024	–	7001	4019	755	0	–	1	27.75 ± 2.13	1	51.97 ± 7.78	180.29	14.10	47.0	37.2	235
80	69027	–	7002	4037	–	0	–	1	83.17 ± 6.49	1	95.00 ± 25.43	180.35	13.40	80.3	66.3	105
81	13046	–	7021	4045	–	0	–	1	407.52 ± 8.54	1	646.10 ± 14.16	180.67	1.98	72.6	61.3	95
82	98037	–	–	–	–	1	52.40 ± 5.62	1	55.56 ± 1.49	1	51.21 ± 4.85	180.90	16.06	40.3	36.9	195
83	41031	–	7035	–	–	0	–	1	15.49 ± 2.50	1	26.44 ± 6.47	180.92	2.64	34.6	33.9	240
84	69036	–	7048	4067	–	0	–	1	80.00 ± 2.44	1	57.28 ± 8.79	181.05	10.85	50.4	37.4	135
85	243044	–	7095	4100	–	1	164.33 ± 29.44	1	872.20 ± 14.34	1	917.06 ± 26.50	181.54	49.58	149.6	73.7	253
86	41041	–	7111	4116	–	0	–	1	187.82 ± 9.56	1	196.46 ± 27.11	181.90	2.69	85.3	63.6	253
87	69058	–	7117	4119	–	0	–	1	52.16 ± 1.75	1	41.30 ± 5.23	182.04	10.38	34.9	34.5	240
88	41042	–	7116	4123	–	1	293.33 ± 50.66	1	496.66 ± 36.95	1	1171.13 ± 84.42	182.05	2.88	116.6	103.4	195
89	69088	66	7215	4178	–	0	–	1	331.86 ± 24.43	1	369.44 ± 56.75	183.19	10.87	157.5	74.9	120
90	13104	–	7214	4179	–	0	–	1	43.10 ± 1.96	0	<18.50	183.22	1.30	38.0	33.0	235
91	98108	92	7231	4192	–	0	–	1	1297.32 ± 29.33	1	1020.42 ± 72.65	183.45	14.90	239.0	87.5	245
92	69101	131	7255	–	3061	0	–	1	55.42 ± 2.94	1	43.40 ± 6.29	183.77	14.03	52.7	37.9	210
93	187029	–	7256	4203	–	1	123.95 ± 25.96	1	108.53 ± 3.72	1	65.07 ± 8.37	183.77	33.20	46.6	43.6	270
94	69104	145	7260	4206	–	1	103.62 ± 17.73	1	113.45 ± 10.91	1	86.90 ± 19.53	183.82	13.02	104.4	41.0	270
95	69107	152	7268	4207	–	1	238.36 ± 24.04	1	259.14 ± 4.74	1	221.32 ± 13.15	183.88	9.59	69.9	44.9	210
96	69110	157	7275	4212	–	0	–	1	772.03 ± 7.99	1	744.83 ± 25.65	183.91	13.90	85.5	68.2	165
97	69112	167	7284	4216	–	0	–	1	879.32 ± 32.44	1	538.97 ± 48.61	183.98	13.15	216.9	66.6	109
98	69119	187	7291	4222	–	0	–	1	110.17 ± 9.02	1	117.75 ± 9.88	184.09	13.31	92.2	44.5	145
99	69123	213	7305	4237	3094	0	–	1	43.61 ± 1.22	1	35.43 ± 4.35	184.23	13.62	39.1	29.8	182
100	98130	226	7315	4245	–	1	282.77 ± 29.87	1	345.59 ± 5.62	1	298.23 ± 19.80	184.30	15.32	84.4	48.7	195
101	158060	–	7338	4251	–	1	61.84 ± 10.28	1	52.72 ± 1.35	1	23.32 ± 5.76	184.54	28.17	36.5	36.1	185
102	98144	307	7345	4254	–	1	4007.17 ± 424.49	1	4845.70 ± 52.14	1	4329.48 ± 131.60	184.71	14.42	190.7	160.7	150
103	42015	341	7361	4260	–	0	–	1	40.88 ± 2.62	0	<25.92	184.84	6.10	68.2	35.8	135
104	99015	–	7366	–	–	0	–	0	<4.96	0	<14.81	184.87	17.23	50.4	25.2	215
105	99014	355	7365	4262	–	1	36.89 ± 6.81	1	25.35 ± 1.54	1	9.09 ± 2.95	184.88	14.88	26.6	27.7	235
106	42032	393	7385	4276	–	0	–	1	65.74 ± 7.11	1	50.66 ± 14.96	185.03	7.69	57.9	59.1	93
107	42033	404	7387	–	–	0	–	1	38.42 ± 6.70	0	<46.09	185.07	4.20	59.1	35.5	105
108	42037	434	–	4287	–	0	–	1	28.25 ± 1.67	1	25.64 ± 5.61	185.20	5.64	33.9	32.7	160

Table A.2. continued.

HRS	CGCG	VCC	UGC	NGC	IC	Flag 8 μm	S_8 (mJy)	Flag 12 μm	S_{12} (mJy)	Flag 22 μm	S_{22} (mJy)	RA$_{ap}$	Dec$_{ap}$	a ('')	b ('')	PA (deg)
109	42038	449	7403	4289	–	0	–	1	75.08 ± 4.67	1	51.81 ± 11.69	185.26	3.72	55.8	33.6	91
110	70024	465	7407	4294	–	1	128.34 ± 15.58	1	151.43 ± 13.08	1	214.19 ± 18.98	185.32	11.51	83.6	54.9	250
111	99024	483	7412	4298	–	0	–	1	583.32 ± 14.04	1	493.12 ± 30.41	185.39	14.60	90.1	68.0	230
112	42044	492	7413	4300	–	0	–	1	25.05 ± 5.71	1	19.61 ± 5.41	185.42	5.39	46.2	20.7	130
113	99027	497	7418	4302	–	1	563.72 ± 59.41	1	638.59 ± 14.70	1	469.16 ± 29.12	185.43	14.60	156.2	49.1	267
114	42045	508	7420	4303	–	1	3304.42 ± 406.37	1	4176.90 ± 105.27	1	4077.90 ± 127.47	185.48	4.47	161.7	158.6	252
115	42047	517	7422	–	–	0	–	1	33.25 ± 4.94	1	55.84 ± 9.92	185.51	5.10	57.4	36.3	260
116	70031	522	7432	4305	–	0	–	0	<7.78	0	<19.84	185.51	12.74	43.9	31.1	115
117	70029	524	7431	4307	–	0	–	1	148.44 ± 3.76	1	125.77 ± 11.47	185.52	9.04	67.4	39.7	115
118	42053	552	7439	–	–	0	–	0	<35.78	0	<53.10	185.61	4.57	54.9	56.8	260
119	99029	559	7442	4312	–	0	–	1	251.21 ± 3.77	1	201.38 ± 9.21	185.63	15.54	67.3	48.3	260
120	70034	570	7445	4313	–	0	–	1	180.36 ± 7.16	1	124.91 ± 13.47	185.66	11.80	72.9	47.8	233
121	70035	576	7447	4316	–	0	–	1	197.76 ± 5.61	1	157.34 ± 11.26	185.68	9.33	71.2	36.5	200
122	99030	596	7450	4321	–	1	2969.25 ± 341.07	1	3779.08 ± 50.22	1	3543.76 ± 129.27	185.73	15.82	192.9	173.2	120
123	42063	613	7451	4324	–	0	–	1	78.41 ± 5.76	1	54.09 ± 7.99	185.78	5.25	48.7	38.2	143
124	70039	630	7456	4330	–	1	119.11 ± 13.48	1	132.86 ± 9.44	1	106.66 ± 17.70	185.82	11.37	87.8	46.5	154
125	42068	648	7461	4339	–	0	–	0	26.73 ± 4.79	0	<62.73	185.90	6.08	47.1	52.5	100
126	99036	654	7467	4340	–	0	–	0	18.61 ± 0.77	0	<7.77	185.90	16.72	26.0	23.5	192
127	42070	656	7465	4343	–	0	–	1	156.89 ± 6.16	1	122.24 ± 9.21	185.91	6.95	64.6	41.8	220
128	42072	667	7469	–	3259	0	–	1	33.43 ± 2.53	1	26.31 ± 7.26	185.95	7.19	46.7	35.5	105
129	99038	685	7473	4350	–	1	68.51 ± 7.56	1	62.30 ± 3.19	1	34.12 ± 7.66	185.99	16.69	49.7	41.8	118
130	70045	692	7476	4351	–	1	69.68 ± 8.19	1	70.77 ± 6.58	1	49.53 ± 8.76	186.01	12.20	47.9	41.3	160
131	42079	697	7474	–	3267	0	–	0	31.96 ± 2.11	0	<19.59	186.02	7.04	41.5	37.5	120
132	42080	699	7477	–	3268	0	–	1	34.88 ± 2.92	1	42.72 ± 10.82	186.03	6.61	47.7	45.2	112
133	158099	–	7483	4359	–	0	–	1	47.68 ± 5.06	1	37.94 ± 11.16	186.05	31.52	82.4	41.7	195
134	70048	713	7482	4356	–	0	–	1	55.23 ± 3.42	1	82.30 ± 13.24	186.06	8.54	55.1	39.1	130
135	42083	731	7488	4365	–	1	165.75 ± 50.76	1	94.12 ± 5.57	1	38.78 ± 10.67	186.12	7.32	46.5	39.2	131
136	42089	758	7492	4370	–	0	–	1	63.78 ± 2.90	1	44.94 ± 9.17	186.23	7.45	49.9	41.5	170
137	70057	759	7493	4371	–	0	<106.70	0	47.50 ± 2.52	0	18.09 ± 0.10	186.23	11.70	40.6	41.9	195
138	70058	763	7494	4374	–	1	274.64 ± 85.19	1	163.42 ± 3.85	1	76.04 ± 10.60	186.27	12.89	52.0	53.5	225
139	42093	787	7498	4376	–	0	–	1	37.99 ± 6.43	0	<44.15	186.32	5.74	45.9	41.1	225
140	42092	785	7497	4378	–	1	120.33 ± 28.03	1	105.38 ± 28.91	1	60.89 ± 19.47	186.32	4.93	75.7	58.5	250
141	70061	792	7503	4380	–	1	141.67 ± 19.40	1	166.56 ± 7.52	1	117.90 ± 29.31	186.34	10.02	100.4	52.0	245
142	99044	801	7507	4383	–	1	338.34 ± 34.42	1	428.68 ± 7.33	1	949.59 ± 28.47	186.36	16.47	85.6	79.6	110
143	42095	827	7513	–	–	0	–	1	197.76 ± 11.74	1	169.05 ± 18.07	186.43	7.22	84.2	43.0	245
144	70068	836	7520	4388	–	1	602.73 ± 63.95	1	1065.70 ± 17.01	1	2405.87 ± 63.10	186.45	12.66	108.5	92.3	180
145	70067	849	7519	4390	–	0	–	1	67.12 ± 4.35	1	63.92 ± 15.37	186.46	10.46	57.7	53.0	215
146	42098	851	7518	–	3322	0	–	1	65.99 ± 4.74	1	53.16 ± 8.87	186.48	7.55	56.5	32.4	250
147	42099	859	7522	–	–	0	–	1	81.01 ± 10.03	1	58.53 ± 14.01	186.49	3.43	73.9	37.8	220
148	99049	865	7526	4396	–	1	103.83 ± 11.77	1	111.98 ± 6.64	1	108.93 ± 22.65	186.50	15.67	81.5	49.5	215
149	70071	873	7528	4402	–	1	587.08 ± 59.30	1	678.54 ± 13.05	1	631.06 ± 30.34	186.53	13.11	108.4	63.2	180
150	70072	881	7532	4406	–	0	<262.59	0	163.85 ± 10.48	0	73.64 ± 17.56	186.55	12.94	67.0	63.4	220
151	70076	912	7538	4413	–	1	115.66 ± 16.83	1	133.77 ± 5.69	1	130.27 ± 14.34	186.63	12.61	54.1	55.1	105
152	42104	921	7536	4412	–	1	176.69 ± 18.20	1	225.69 ± 10.38	1	382.67 ± 24.93	186.65	3.96	52.6	59.5	166
153	42105	938	7541	4416	–	0	–	1	132.42 ± 8.89	1	101.17 ± 11.54	186.69	7.92	63.0	54.4	235
154	70082	939	7546	–	–	0	–	1	49.16 ± 3.38	1	40.34 ± 12.38	186.70	8.89	50.4	48.9	165
155	70080	944	7542	4417	–	0	–	1	37.45 ± 2.15	0	<23.52	186.71	9.58	73.4	26.1	139
156	99054	958	7551	4419	–	1	399.54 ± 41.43	1	658.67 ± 15.62	1	1188.63 ± 29.19	186.74	15.05	88.9	82.2	223
157	42106	957	7549	4420	–	1	234.41 ± 24.80	1	241.07 ± 6.39	1	222.49 ± 17.69	186.74	2.49	63.1	45.3	98
158	42107	971	7556	4423	–	0	–	0	<35.14	0	<37.55	186.79	5.88	60.3	41.0	110
159	70090	979	7561	4424	–	1	169.85 ± 20.87	1	189.15 ± 4.99	1	283.23 ± 13.19	186.80	9.42	58.4	53.1	190
160	42111	1002	7566	4430	–	0	–	1	181.78 ± 23.50	1	134.00 ± 15.84	186.86	6.26	59.9	53.9	210
161	70093	1003	7568	4429	–	0	–	1	172.65 ± 14.14	1	106.10 ± 9.49	186.86	11.11	44.1	45.2	189
162	70098	1030	7575	4435	–	1	120.06 ± 13.76	1	108.69 ± 3.40	1	116.69 ± 9.62	186.92	13.08	45.6	42.1	100

Table A.2. continued.

HRS	CGCG	VCC	UGC	NGC	IC	Flag 8 μm	S_8 (mJy)	Flag 12 μm	S_{12} (mJy)	Flag 22 μm	S_{22} (mJy)	RA$_{ap}$	Dec$_{ap}$	a ('')	b ('')	PA (deg)
163	70097	1043	7574	4438	–	0	<308.38	1	345.29 ± 14.30	1	229.29 ± 30.84	186.93	13.01	96.5	74.1	117
164	70099	1047	7581	4440	–	0	–	1	18.36 ± 2.72	0	<16.24	186.97	12.29	39.6	38.5	183
165	42117	1048	7579	–	–	0	–	0	<35.34	1	<24.45	186.98	5.72	48.0	32.8	220
166	70100	1062	7583	4442	–	0	<141.65	1	70.67 ± 2.26	1	34.60 ± 7.86	187.01	9.80	46.1	42.9	177
167	70104	1086	7587	4445	–	0	–	1	53.17 ± 4.39	1	35.21 ± 9.95	187.07	9.44	58.3	28.8	195
168	70108	1091	7590	–	–	0	–	1	17.93 ± 3.99	1	20.72 ± 5.30	187.08	8.73	36.2	32.7	265
169	99063	–	7595	–	3391	0	–	1	52.73 ± 3.44	1	40.95 ± 9.34	187.11	18.42	52.0	40.8	185
170	99062	1110	7594	4450	–	1	270.74 ± 48.24	1	324.31 ± 16.72	1	201.30 ± 59.92	187.12	17.08	133.9	80.4	261
171	70111	1118	7600	4451	–	0	–	1	149.23 ± 4.21	1	139.41 ± 13.55	187.17	9.26	49.8	46.4	260
172	99065	1126	7602	–	3392	1	116.73 ± 16.48	1	137.92 ± 2.73	1	110.64 ± 10.24	187.18	15.00	54.1	43.3	130
173	42124	1145	7609	4457	–	1	287.72 ± 31.39	1	372.93 ± 8.24	1	369.98 ± 27.17	187.25	3.57	71.8	72.6	165
174	70116	1154	7614	4459	–	0	–	1	178.88 ± 6.75	1	133.28 ± 12.30	187.25	13.98	58.3	52.2	195
175	70115	1158	7613	4461	–	0	–	1	31.24 ± 1.28	1	12.40 ± 3.97	187.26	13.18	32.6	28.3	95
176	70121	1190	7622	4469	–	0	–	1	93.98 ± 9.84	1	83.57 ± 12.38	187.37	8.75	46.0	42.4	175
177	42132	1205	7627	4470	–	0	–	1	147.90 ± 9.17	1	133.31 ± 8.58	187.41	7.82	53.2	43.9	270
178	42134	1226	7629	4472	–	1	397.13 ± 118.29	1	284.99 ± 13.73	1	122.54 ± 16.18	187.45	8.00	60.2	54.1	245
179	70125	1231	7631	4473	–	1	108.39 ± 27.00	1	80.02 ± 3.43	1	38.62 ± 9.72	187.45	13.43	55.1	38.7	190
180	70129	1253	7638	4477	–	0	<134.88	1	70.46 ± 3.01	1	36.00 ± 7.00	187.51	13.64	43.9	37.9	125
181	70133	1279	7645	4478	–	1	41.28 ± 8.65	1	29.46 ± 2.06	1	18.53 ± 4.81	187.57	12.33	38.6	37.3	230
182	42139	1290	7647	4480	–	0	–	1	146.62 ± 19.38	1	139.12 ± 18.43	187.61	4.25	62.4	48.8	260
183	70139	1316	7654	4486	–	1	333.49 ± 49.04	1	338.93 ± 9.19	1	219.22 ± 23.89	187.71	12.39	71.3	75.8	249
184	70140	1326	7657	4491	–	0	–	1	70.87 ± 4.39	1	268.17 ± 8.47	187.74	11.48	50.9	48.8	238
185	42141	1330	7656	4492	–	0	–	1	46.65 ± 2.74	1	25.76 ± 6.24	187.75	8.08	34.6	33.1	165
186	129005	–	7662	4494	–	1	133.63 ± 30.17	1	100.93 ± 3.51	1	53.84 ± 9.80	187.85	25.77	55.3	52.4	90
188	99075	1379	7669	4498	–	1	135.02 ± 16.00	1	150.48 ± 7.55	1	121.77 ± 0.16	187.91	16.85	88.1	57.4	215
189	99077	1393	7676	–	797	1	67.47 ± 9.39	1	72.16 ± 2.71	1	56.50 ± 9.28	187.98	15.12	48.0	45.1	198
190	99076	1401	7675	4501	–	1	2142.59 ± 234.17	1	2717.46 ± 40.03	1	2223.65 ± 76.21	188.00	14.42	164.3	109.0	230
191	99078	1410	7677	4502	–	0	–	0	12.28 ± 1.41	0	<14.16	188.01	16.69	41.5	28.1	130
192	70152	1419	7682	4506	–	0	–	1	16.57 ± 2.44	1	11.07 ± 2.39	188.04	13.42	36.1	29.1	195
193	70157	1450	7695	–	3476	0	–	2	103.59 ± 2.98	2	131.70 ± 4.72	188.17	14.05	54.7	38.5	120
194	14063	–	7694	4517	–	1	1004.60 ± 117.71	1	1186.64 ± 76.38	1	1095.90 ± 175.79	188.19	0.12	253.6	65.5	170
195	99087	1479	7703	4516	–	0	–	0	<10.39	0	<21.44	188.28	14.57	82.0	23.6	260
196	70167	1508	7709	4519	–	1	213.86 ± 34.50	1	305.53 ± 19.27	1	492.47 ± 44.16	188.38	8.65	93.7	79.1	242
197	70168	1516	7711	4522	–	1	156.03 ± 19.30	1	157.93 ± 8.49	1	133.24 ± 11.74	188.41	9.18	66.7	35.4	123
198	159016	–	7714	4525	–	0	–	1	61.05 ± 2.45	1	36.47 ± 11.59	188.46	30.28	62.1	48.6	155
199	99090	1532	7716	–	800	1	45.58 ± 7.40	1	47.94 ± 6.57	1	48.26 ± 11.45	188.49	15.35	58.9	58.2	240
200	42155	1535	7718	4526	–	1	357.12 ± 53.34	1	337.62 ± 5.33	1	313.41 ± 8.53	188.51	7.70	53.6	49.9	253
201	42156	1540	7721	4527	–	0	–	1	2966.58 ± 31.31	1	3117.49 ± 77.49	188.54	2.65	190.2	95.8	157
202	70173	1549	7728	–	3510	0	–	0	<22.33	0	<20.04	188.56	11.07	46.2	32.8	100
203	42158	1554	7726	4532	–	1	248.89 ± 25.53	1	339.28 ± 9.39	1	756.73 ± 22.81	188.58	6.47	85.7	60.5	256
204	42159	1555	7727	4535	–	0	–	1	1636.76 ± 60.13	1	1651.58 ± 143.88	188.59	8.20	179.7	135.7	270
205	14068	1562	7732	4536	–	1	1504.63 ± 173.27	1	2025.78 ± 66.83	1	3367.49 ± 88.53	188.61	2.19	255.6	141.2	50
206	42162	1575	7736	–	3521	0	–	1	185.48 ± 6.92	1	129.14 ± 16.73	188.66	7.16	64.2	49.6	108
207	99093	1588	7742	4540	–	1	484.95 ± 66.03	1	621.84 ± 39.32	1	142.12 ± 11.77	188.71	15.55	51.5	52.8	145
208	99096	1615	7753	4548	–	1	97.14 ± 16.71	1	90.53 ± 5.11	1	429.84 ± 87.98	188.86	14.49	149.5	137.2	240
209	–	1619	–	4546	–	0	–	1	20.86 ± 1.07	1	52.09 ± 14.32	188.87	−3.79	69.1	52.1	170
210	70182	1632	7757	4550	–	1	30.09 ± 9.25	1	123.10 ± 6.00	0	<8.24	188.88	12.22	22.3	20.9	270
211	70184	–	7760	4552	–	1	173.34 ± 46.49	1	46.92 ± 3.84	1	55.97 ± 11.22	188.91	12.56	52.3	48.6	90
212	99098	–	7768	4561	–	1	42.40 ± 6.24	1	–	1	70.79 ± 12.16	189.03	19.32	57.4	58.4	200
213	129010	1664	7772	4565	–	1	1852.40 ± 192.51	1	2298.49 ± 42.19	1	1679.79 ± 87.82	189.09	25.99	495.3	70.9	225
214	70186	1673	7773	4564	–	0	<68.84	1	36.94 ± 2.02	1	15.65 ± 4.49	189.11	11.44	32.9	32.4	137
215	70189	1676	7777	4567	–	0	–	2	588.65 ± 7.55	2	497.53 ± 16.37	189.14	11.26	51.5	41.3	165
216	70188	–	7776	4568	–	0	–	2	1522.07 ± 12.74	2	1485.09 ± 26.31	189.14	11.23	93.2	53.0	123
217	70192	1690	7786	4569	–	1	1027.39 ± 124.29	1	1356.93 ± 33.06	1	1432.95 ± 48.20	189.20	13.16	137.3	88.9	113

Table A.2. continued.

HRS	CGCG	VCC	UGC	NGC	IC	Flag 8 μm	S_8 (mJy)	Flag 12 μm	S_{12} (mJy)	Flag 22 μm	S_{22} (mJy)	RA_{ap}	Dec_{ap}	a ('')	b ('')	PA (deg)
218	42178	1692	7785	4570	–	1	64.12 ± 11.24	1	46.95 ± 2.27	1	21.66 ± 4.82	189.22	7.24	41.4	32.1	249
219	70195	1720	7793	4578	–	0	<72.46	1	25.60 ± 4.07	0	<42.9	189.38	9.56	51.2	48.5	120
220	70197	1727	7796	4579	–	1	714.00 ± 161.94	1	1034.71 ± 41.02	1	762.47 ± 65.92	189.43	11.82	132.7	118.8	190
221	42183	1730	7794	4580	–	1	128.10 ± 17.75	1	153.32 ± 3.48	1	131.83 ± 10.26	189.45	5.37	57.1	46.1	250
222	70199	1757	7803	4584	–	0	–	1	26.48 ± 1.72	0	<12.58	189.57	13.11	35.0	32.7	110
223	42186	1758	7802	–	–	0	–	1	10.69 ± 1.51	1	21.64 ± 5.56	189.59	7.89	38.9	26.2	145
224	42187	1760	7804	4586	–	0	–	1	73.20 ± 2.00	1	36.57 ± 9.83	189.62	4.32	52.0	38.3	205
225	70202	1778	7817	–	3611	0	–	0	<5.61	0	<10.78	189.77	13.36	33.9	30.3	205
226	42191	1780	7821	4591	–	0	–	1	60.90 ± 1.50	1	58.50 ± 3.48	189.80	6.01	49.9	38.6	130
227	14091	–	–	4592	–	1	93.14 ± 16.56	1	103.66 ± 11.47	1	112.60 ± 29.61	189.83	-0.53	93.8	49.6	185
228	–	–	–	–	3631	0	–	0	<5.35	0	<14.52	189.84	-5.66	25.5	22.4	90
229	70204	1809	7825	–	–	0	–	0	<14.63	0	<22.89	189.95	12.97	46.2	28.1	180
230	99106	1811	7826	4595	–	0	–	1	114.65 ± 5.27	1	86.29 ± 6.94	189.96	15.30	53.1	42.8	200
231	70206	1813	7828	4596	–	1	98.21 ± 30.45	1	77.64 ± 2.63	1	42.93 ± 7.26	189.98	10.18	41.4	47.4	225
232	70213	1859	7839	4606	–	1	88.57 ± 15.10	1	93.51 ± 2.23	1	71.71 ± 7.39	190.24	11.91	45.6	37.7	123
233	70216	1868	7843	4607	–	1	234.50 ± 24.66	1	237.34 ± 6.23	1	232.54 ± 13.66	190.30	11.89	86.1	46.6	94
234	70214	1869	7842	4608	–	0	–	1	31.89 ± 2.77	0	<20.19	190.30	10.16	39.9	40.3	120
235	42205	1883	7850	4612	–	1	28.99 ± 6.22	1	18.75 ± 0.82	0	<11.21	190.39	7.32	26.8	25.2	215
236	70223	1903	7858	4621	–	1	151.02 ± 39.73	1	112.92 ± 4.58	1	51.32 ± 11.79	190.51	11.65	59.4	46.0	254
237	42208	1923	7871	4630	–	1	169.57 ± 18.55	1	203.08 ± 3.88	1	274.07 ± 9.04	190.63	3.96	68.9	54.6	100
238	14109	–	7869	4629	–	0	–	1	7.52 ± 2.02	0	<20.48	190.64	-1.35	44.9	34.1	170
239	99112	1932	7875	4634	–	0	–	1	361.84 ± 8.04	1	309.15 ± 10.64	190.67	14.30	71.4	42.9	246
240	70229	1938	7880	4638	–	1	47.54 ± 7.20	1	30.74 ± 2.14	0	<14.56	190.70	11.44	33.2	30.6	210
241	43002	1939	7878	4636	–	1	149.92 ± 49.49	1	78.08 ± 5.14	1	32.30 ± 5.74	190.71	2.69	35.3	36.7	0
242	70230	1943	7884	4639	–	1	166.56 ± 17.15	1	181.53 ± 16.37	1	140.16 ± 23.84	190.72	13.26	84.1	58.3	213
243	15008	–	7895	4643	–	0	–	1	147.01 ± 17.22	0	<111.84	190.83	1.98	87.0	85.5	225
244	71015	1972	7896	4647	–	1	296.74 ± 48.48	1	739.29 ± 9.05	1	636.13 ± 25.73	190.88	11.58	84.8	71.1	195
245	71016	1973	7898	4649	–	1	586.36 ± 61.77	1	277.45 ± 5.75	1	129.57 ± 13.96	190.92	11.55	62.9	59.7	195
246	100004	–	7901	4651	–	1	1320.38 ± 138.15	1	698.80 ± 40.49	1	587.34 ± 31.65	190.93	16.39	130.7	102.6	170
247	71019	1987	7902	4654	–	0	–	1	1626.65 ± 33.91	1	1670.09 ± 94.73	190.99	13.13	150.6	91.5	218
248	71023	2000	7914	4660	–	1	40.82 ± 5.88	1	34.10 ± 2.07	1	20.24 ± 5.31	191.13	11.19	38.6	32.4	190
249	71026	2006	7920	–	3718	0	–	0	<5.92	0	<14.15	191.19	12.35	38.5	31.0	162
250	43018	–	–	4665	–	0	–	1	63.67 ± 5.95	0	<48.63	191.27	3.06	52.9	40.9	270
251	15015	–	7924	4666	–	0	–	1	3724.87 ± 35.39	1	3334.35 ± 63.00	191.29	-0.46	159.8	93.0	134
252	15016	–	7926	4668	–	0	–	1	44.55 ± 4.27	1	49.70 ± 12.83	191.38	-0.54	59.9	42.5	95
253	15019	–	7931	4684	–	0	–	1	80.97 ± 3.88	1	248.91 ± 11.12	191.82	-2.73	49.6	46.6	110
254	71043	2058	7951	4689	–	1	429.30 ± 77.25	1	550.45 ± 15.46	1	445.25 ± 39.88	191.94	13.76	101.0	89.8	254
255	43028	–	7965	4688	–	0	–	1	41.73 ± 7.27	1	118.66 ± 13.20	191.94	4.34	53.0	46.2	125
256	15023	–	7961	–	–	0	<108.06	1	875.50 ± 11.61	1	1954.50 ± 34.70	192.06	-3.33	86.3	85.2	105
257	71045	2070	7970	4698	–	1	232.60 ± 65.72	1	179.04 ± 15.85	0	<96.98	192.10	8.49	108.6	71.4	255
259	43034	–	7975	4701	–	1	185.09 ± 19.13	1	207.65 ± 58.29	1	206.69 ± 30.66	192.30	3.39	63.1	53.1	130
260	100011	–	7980	4710	–	0	–	1	291.28 ± 8.14	1	435.63 ± 18.54	192.41	15.17	87.4	56.0	117
261	43040	–	7982	–	–	0	–	1	64.04 ± 8.21	1	38.50 ± 12.03	192.46	2.85	78.9	28.4	270
262	43041	–	7985	4713	–	1	288.78 ± 31.37	1	322.59 ± 10.11	1	367.05 ± 26.95	192.49	5.31	76.0	71.4	200
263	129027	–	7989	4725	–	1	1137.15 ± 203.69	1	1290.81 ± 70.12	1	828.33 ± 210.57	192.61	25.50	277.4	173.5	125
264	15027	–	7991	–	–	0	–	1	18.55 ± 2.48	0	<29.83	192.66	1.46	57.6	36.9	260
265	–	–	–	4720	–	0	–	1	48.45 ± 3.22	1	64.15 ± 9.26	192.68	-4.16	57.7	44.5	205
266	–	–	–	4731	–	1	124.74 ± 20.66	1	239.51 ± 26.89	1	257.92 ± 70.41	192.76	-6.39	189.4	76.6	180
267	129028	–	8005	4747	–	0	–	1	148.30 ± 5.79	1	211.37 ± 22.46	192.94	25.77	90.3	56.2	120
268	71060	–	8007	4746	–	0	<149.42	1	411.09 ± 12.46	1	431.88 ± 22.87	192.98	12.08	92.6	51.9	210
269	71062	2092	8010	4754	–	0	–	1	57.21 ± 2.43	1	24.47 ± 6.47	193.07	11.31	42.3	40.1	111
270	15029	–	8009	4753	–	0	–	1	370.70 ± 17.20	1	196.26 ± 33.21	193.09	-1.20	81.6	55.9	195
271	100015	–	8014	4758	–	0	–	1	89.84 ± 5.09	1	96.77 ± 17.38	193.18	15.85	95.9	45.6	250
272	71065	2095	8016	4762	–	1	92.08 ± 17.93	1	68.85 ± 6.46	1	29.34 ± 8.97	193.23	11.23	69.9	39.5	122

Table A.2. continued.

HRS	CGCG	VCC	UGC	NGC	IC	Flag 8 μm	S_8 (mJy)	Flag 12 μm	S_{12} (mJy)	Flag 22 μm	S_{22} (mJy)	RA_{ap}	Dec_{ap}	a ('')	b ('')	PA (deg)
273	15031	–	8020	4771	–	0	–	1	195.75 ± 13.41	1	141.86 ± 26.54	193.34	1.27	98.5	54.3	225
274	15032	–	8021	4772	–	1	84.04 ± 19.12	1	106.20 ± 16.49	1	61.26 ± 19.02	193.37	2.17	117.5	44.2	235
275	–	–	–	4775	–	0	–	1	286.93 ± 9.85	1	316.08 ± 37.76	193.44	−6.62	89.9	84.0	140
276	71068	–	8022	4779	–	0	–	1	164.42 ± 5.88	1	221.90 ± 18.38	193.46	9.71	64.9	64.3	100
277	43060	–	–	4791	–	0	–	1	13.66 ± 1.54	0	<10.51	193.68	8.05	30.5	27.1	155
278	71071	–	8032	–	–	0	–	1	36.19 ± 2.15	1	25.01 ± 2.91	193.68	13.24	48.4	34.5	255
280	43066	–	8043	4799	–	0	–	1	116.81 ± 2.93	1	94.35 ± 12.05	193.82	2.90	49.8	37.5	180
281	43068	–	8045	–	–	0	–	1	19.07 ± 1.32	1	16.87 ± 4.79	193.85	7.91	38.2	30.2	195
282	43069	–	–	4803	–	0	–	1	3.89 ± 1.12	0	<9.38	193.89	8.24	31.8	22.2	105
283	43071	–	8054	4808	–	1	527.31 ± 53.25	1	585.17 ± 12.77	1	565.62 ± 98.46	193.95	4.30	74.4	49.3	217
284	–	–	–	–	3908	0	–	1	577.48 ± 10.81	1	681.22 ± 25.60	194.17	−7.56	72.7	51.2	260
285	15049	–	8078	4845	–	0	–	1	486.45 ± 13.21	1	583.24 ± 29.37	194.51	1.58	101.1	64.0	170
286	71092	–	8102	4866	–	0	–	1	52.22 ± 3.53	0	<29.67	194.86	14.17	66.2	43.8	177
287	15055	–	8121	4904	–	0	–	1	263.03 ± 7.29	1	278.61 ± 24.88	195.24	−0.03	84.1	78.2	235
288	–	–	–	4941	–	1	176.04 ± 24.22	1	334.76 ± 16.05	1	434.20 ± 27.92	196.05	−5.55	111.9	70.4	105
289	–	–	–	4981	–	0	–	1	497.42 ± 19.27	1	445.84 ± 34.21	197.20	−6.78	98.2	82.7	239
290	189037	–	8271	5014	–	1	122.15 ± 12.49	1	139.37 ± 4.03	1	186.17 ± 10.78	197.88	36.28	64.5	52.4	192
291	217031	–	8388	5103	–	0	–	1	12.03 ± 1.58	0	<12.35	200.12	43.08	37.8	35.7	230
292	218010	–	8439	5145	–	0	–	1	482.47 ± 3.25	1	511.19 ± 17.06	201.31	43.27	67.9	66.3	175
293	16069	–	8443	5147	–	1	187.70 ± 19.54	1	217.11 ± 5.30	1	246.95 ± 18.52	201.58	2.10	76.6	70.9	215
294	246017	–	8593	–	902	0	–	1	93.94 ± 2.38	1	90.33 ± 7.97	204.01	49.96	58.1	42.9	250
295	73054	–	8616	5248	–	1	1867.41 ± 242.99	1	2426.32 ± 24.98	1	2475.36 ± 104.41	204.38	8.89	208.1	116.8	230
296	190041	–	8675	5273	–	1	48.86 ± 9.55	1	62.96 ± 2.55	1	94.60 ± 9.72	205.54	35.65	56.1	56.8	95
297	246023	–	8711	5301	–	0	–	1	325.35 ± 10.43	1	283.06 ± 17.63	206.60	46.11	128.9	57.9	240
298	218047	–	8725	5303	–	1	217.18 ± 21.80	1	242.25 ± 5.01	1	283.36 ± 10.39	206.94	38.31	65.3	53.1	175
299	45108	–	8727	5300	–	0	–	1	192.18 ± 15.22	1	160.27 ± 30.99	207.07	3.95	112.6	95.5	230
300	218058	–	8756	–	–	0	–	1	29.04 ± 1.57	1	24.14 ± 4.63	207.65	42.54	44.7	42.2	175
301	17088	–	8790	5334	4338	0	–	1	174.39 ± 14.60	1	137.86 ± 30.01	208.23	−1.11	100.0	95.4	130
302	45137	–	8821	5348	–	0	–	1	36.86 ± 3.18	1	26.49 ± 6.12	208.55	5.23	88.6	35.6	267
303	295024	–	8843	5372	–	0	–	1	165.60 ± 3.55	1	205.88 ± 7.84	208.69	58.67	58.2	62.2	220
304	46001	–	8831	5356	958	0	–	1	137.95 ± 4.44	1	97.84 ± 9.54	208.74	5.33	87.4	44.5	102
305	46003	–	8838	5360	–	0	–	1	16.62 ± 1.17	0	<12.89	208.91	4.99	40.9	30.1	160
306	46007	–	8847	5363	–	1	205.98 ± 40.62	1	241.75 ± 8.69	1	143.33 ± 29.74	209.03	5.26	88.6	76.7	220
307	46009	–	8853	5364	–	0	–	1	807.04 ± 32.05	1	637.43 ± 77.44	209.05	5.02	185.6	132.7	120
308	46011	–	8857	–	–	0	–	1	5.33 ± 1.21	0	<9.82	209.11	4.40	34.0	34.0	215
309	272031	–	9036	5486	–	0	–	1	25.89 ± 3.09	1	37.00 ± 6.80	211.85	55.10	56.8	60.8	125
310	47010	–	9172	5560	–	0	–	1	179.48 ± 4.37	1	191.15 ± 19.51	215.02	3.99	81.9	54.8	205
311	47012	–	9175	5566	–	0	<74.65	1	335.13 ± 17.12	0	<196.57	215.08	3.93	174.0	94.2	125
312	47020	–	9183	5576	–	0	–	1	44.64 ± 1.61	0	<19.5	215.26	3.27	43.2	41.5	175
313	47022	–	9187	5577	–	0	–	1	108.27 ± 6.00	0	<79.21	215.30	3.44	91.7	63.0	145
314	19012	–	9215	–	–	0	–	1	77.69 ± 7.43	1	103.31 ± 16.61	215.86	1.73	69.6	57.7	255
315	220015	–	9242	–	–	0	–	0	<26.51	0	<26.27	216.34	39.54	157.6	32.0	161
316	47063	–	9308	5638	–	0	–	1	32.24 ± 2.64	1	15.92 ± 4.55	217.42	3.23	42.6	57.7	235
317	47066	–	9311	–	1022	0	–	1	14.34 ± 1.22	1	11.62 ± 2.69	217.51	3.77	39.4	36.8	255
318	47070	–	9328	5645	–	0	–	1	115.24 ± 9.30	1	137.88 ± 22.06	217.66	7.28	80.7	65.9	195
320	47090	–	9363	5668	–	1	197.87 ± 21.87	1	246.19 ± 15.81	1	251.26 ± 27.94	218.35	4.45	101.2	110.2	197
321	47123	–	9427	5692	–	0	–	1	108.36 ± 1.63	1	107.66 ± 7.62	219.58	3.41	47.4	42.2	130
322	47127	–	9436	5701	–	0	–	1	118.15 ± 26.69	0	<248.19	219.80	5.36	133.2	146.9	270
323	48004	–	9483	–	1048	0	–	1	185.42 ± 4.43	1	168.93 ± 14.39	220.74	4.89	77.5	52.4	253
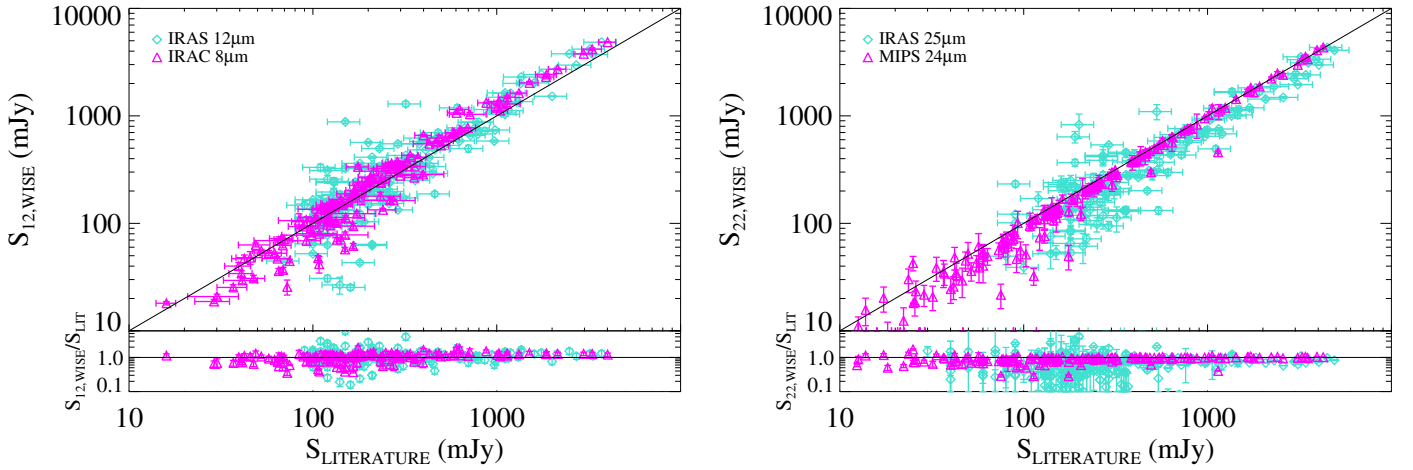
Fig. A.2. Comparison between WISE flux density measurements and NIR/MIR ancillary data available from the literature at 12 and 22 μm (*left and right panels*, respectively). The one-to-one relationship is the solid black line. The WISE to literature flux density ratios are shown in the *lower panels*.

Preliminary Data Release Products[12], Sect. II.3.f, 2.9045×10^{-6} Jy/DN and 5.2269×10^{-5} Jy/DN at 12 and 22 μm, respectively. For WISE photometry of extended sources, Jarrett et al. (2013) recommended three corrections to be applied to all measurements. The first one is an aperture correction that accounts for the WISE absolute photometric calibration method using PSF profile fitting. This correction is 0.03 mag and -0.03 mag at 12 and 22 μm, respectively. The second correction is a color correction that accounts for the spectral signature of the source convolved with WISE relative system response (RSR). Because our SED fitting method integrates the models into the filters of the bands before comparing them with the data, we do not need to apply this correction. The third correction comes from a discrepancy between the WISE photometric standard "blue" stars and "red" galaxies related to an error in the W4 RSR, as described in Wright et al. (2010) and Jarrett et al. (2011). Following Jarrett et al. (2013), we apply a correction factor of 0.92 to the 22 μm flux densities of all of the spirals and disk galaxies. This correction is thus applied to HRS galaxies with morphological type of Sa and later.

We determine the errors in the measurements following the method described for the IRAC data. However, because of a correlated noise with a typical length scale larger than 10 pixels, we use 50×50 boxes rather than 10×10 pixels. Galaxies with a signal-to-noise lower than 3 are considered as undetected, and an upper limit of 3σ is given.

In Table A.2, we give the WISE 12 and 22 μm flux densities of the HRS galaxies. As for IRAC measurements, a flag is provided with the following code: 0 for undetected galaxies, 1 for detected galaxies and 2 for galaxies for which the measurement suffer from sources blending.

To check the validity of our measurements, we compared our results to the NIR and MIR ancillary data available for the HRS galaxies in Fig. A.2. We use the *Spitzer*/IRAC 8 μm from this work and the *Spitzer*/MIPS 24 of Bendo et al. (2012b). Even if the 8 μm filter from IRAC and the 12 μm filter from WISE are not overlapping enough to make a reliable comparison, and knowing that the emission process at the two wavelengths differ, we plot the comparison to identify possible outliers and thus possible issues with the photometry. IRAS data at 12 and 25 μm

are also available for some of the HRS galaxies (Sanders et al. 2003; Moshir & et al. 1990; Thuan & Sauvage 1992; Soifer et al. 1989; Young et al. 1996). Some shifts in the relation can be due to the different wavelength of the data and the different response curve of the filters. There is a good correlation between IRAS and WISE data at 12 μm, but WISE flux densities tend to be higher than IRAS ones. The mean $S_{\mathrm{IRAS}}^{12}/S_{\mathrm{WISE}}^{12}$ is 1.11 with a standard deviation of 0.79. We note that the relation becomes very dispersed for flux densities below $\approx$80 mJy. The relation between the IRAC 8 μm and the WISE 12 μm measured in this work is good, with a standard deviation of 0.43 for the IRAC to WISE flux density ratio, and a mean value of the ratio of 1.08. There might be an effect due to the difference of wavelength, however it is difficult to quantify it as the 8 μm lies completely in the PAH emission domain.

There is good agreement between MIPS 24 μm and WISE 22 μm measurements with a mean MIPS to WISE flux density ratio of 1.22 ± 0.44. Even if very dispersed, the relation between IRAS 25 μm and WISE 22 μm flux densities is good. However, as noticed at 12 μm, the relation becomes very dispersed for $S_{25}^{\mathrm{IRAS}} < 80$ mJy.

Appendix B: Removing the stellar contribution

In global galaxies, the emission in the 2–10 μm range is due to both the old stellar population and the dust (very small grains + PAHs). The contribution of these two components varies differently with the type of the galaxies, the former being dominant in ETG, the latter in star forming systems. Given that the Draine & Li (2007) models deal only with the dust component, we have to remove the stellar contribution first. This has been historically done by considering the Rayleigh-Jeans tail of the stellar emission peaked at $\approx$1–2 μm determined using a blackbody with $T \approx 3000$ K, using the typical SED of ETG not showing any evidence of the presence of dust, or using stellar SEDs derived, for instance, from the Starburst99 models (e.g., Boselli et al. 1998; Helou et al. 2004; Draine et al. 2007). In this work, we use the CIGALE code (Noll et al. 2009), which allows us to compute the stellar SED of a galaxy using stellar population models from (Maraston 2005) convolved with a given star formation history (SFH). We refer the reader to Noll et al. (2009) for a complete description of the code.

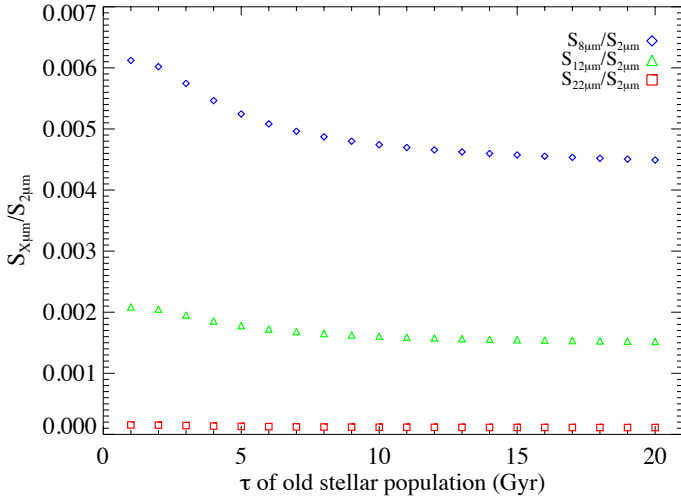[12] http://wise2.ipac.caltech.edu/docs/release/prelim/expsup/wise_prelrel_toc.html

Fig. B.1. Evolution of $S_{8\,\mu m}/S_{2\,\mu m}$, $S_{12\,\mu m}/S_{2\,\mu m}$, and $S_{22\,\mu m}/S_{2\mu m}$ flux density ratios with τ, the e-folding rate of the exponentially decreasing SFR.
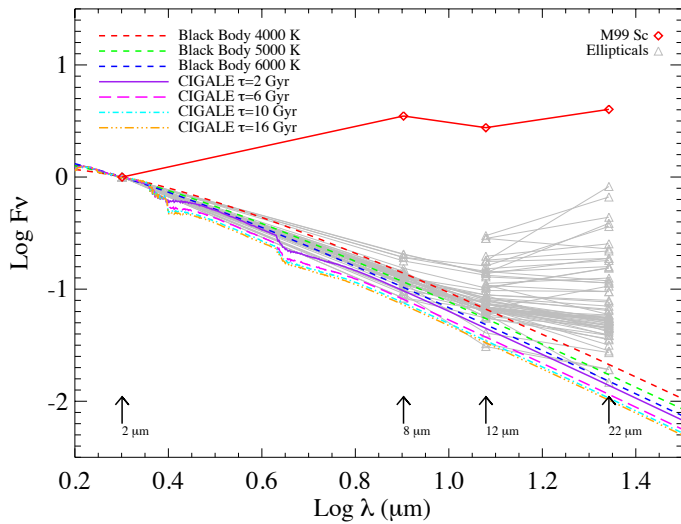

Fig. B.2. SED decomposition. Red diamonds are flux densities of the late type galaxy M 99 normalized to $2\,\mu m$. Grey triangles are flux densities of all HRS early-type galaxies normalized to $2\,\mu m$. Dashed red, green, and blue lines represents black body laws with different temperatures. Purple, magenta, cyan and orange lines represents models from Maraston (2005) convolved by CIGALE with an exponentially decreasing SFH for different e-foldings τ.

Depending on their morphological types, the stellar populations of galaxies have very different characteristics. The elliptical and lenticular galaxies (ETG) are dominated by an old stellar population emitting in NIR whereas stellar populations of late-type galaxies are younger, emitting in UV. To properly remove the stellar contribution from the MIR emission, we need to take these differences into account.

Here, we consider an SFH with a decreasing exponential shape and an e-folding time τ. If the e-folding time of the SFH is very small (1−2 Gyr) then all of the stars are created in a very short time and evolve to become, at the age of the Universe, a very old population. On the contrary, a large e-folding ($\approx$10−20 Gyr) corresponds to a quasi-constant SFR and stars are still being created at the age of the Universe.

To understand the impact of the choice of τ on MIR colors, we show on Fig. B.1 the variation of MIR flux densities

from the models normalized to $2\,\mu m$ with τ. Strong variations are seen for the 8 to $2\,\mu m$ flux density ratios and the 12 to $2\,\mu m$ flux density ratios (36% and 40%, respectively), whereas a very weak variation is seen at $22\,\mu m$. These variations stress the fact that estimates of the stellar emission in MIR strongly depends on the SFH of the galaxy and thus on its morphological type. Small values of τ correspond to a high $S_{8\,\mu m}/S_{2\,\mu m}$ ratio, which is consistent with an important old stellar population. Thus, choosing a τ of 2 Gyr would lead to a SFH compatible with ETGs. With $\tau = 10$ Gyr, there is less variation in the 8 to $2\,\mu m$ flux density ratio. This smaller ratio implies a smaller flux density at $8\,\mu m$, which is what we expect for late-type galaxies.

To estimate the counterpart of the MIR emission due to stars in a late-type galaxy, Helou et al. (2004) used the stellar population models of Starburst 99 (Leitherer et al. 1999). Assuming that the $3.6\,\mu m$ emission was purely stellar, they obtained stellar contribution factors of 0.596, 0.399, 0.232, and 0.032 at 4.5, 5.8, 8.0 and $24.0\,\mu m$, respectively. Draine et al. (2007) proposed similar values obtained from a blackbody emission with a temperature of 5000 K (0.260, 0.0326 at 8.0, and $24.0\,\mu m$, respectively). We use blackbodies of different temperatures and stellar population models computed from CIGALE and present the resulting stellar emission normalized at $2\,\mu m$ in Fig. B.2. For comparison, we show the normalized observed flux densities of all the early-type galaxies of the HRS as well as those of M 99, a typical late-type galaxy of our sample. Differences in the stellar contributions are seen depending on the model (blackbody or models from CIGALE) and on the assumption on the temperature or the e-folding time. Both methods, blackbody or more complex models, pull uncertainties due to the assumption on the parameters (temperature or e-folding time). However, using the models from CIGALE allows us to take the observed differences between the stellar populations of the ETGs and LTGs into account. We thus decide to use the stellar population models computed by CIGALE, with a population aged of 13 Gyr, and consider these differences by using different e-folding times: $\tau = 2$ Gyr for the ETGs and $\tau = 10$ Gyr for the LTGs. In Table B.1, we calculate the coefficients and the associated errors corresponding to the stellar contribution for several NIR and MIR bands (from J to IRAS $60\,\mu m$), normalized to different bands (from J to IRAC 1). Our coefficients are in good agreement with those of Helou et al. (2004) and Draine et al. (2007), i.e., 0.589, 0.396, 0.244, and 0.044 at 4.5, 5.8, 8.0, and $24.0\,\mu m$, respectively, for the late-type galaxies.

Appendix C: Draine & Li (2007) parameters of the HRS galaxies

Even if this work is focused on the study of the dust properties of a subsample of gas-rich galaxies from the HRS, we apply the SED fitting procedure presented in Sect. 4.4 to all of the HRS galaxies. First, we removed the MIR stellar emission using the coefficients presented in Appendix B. In order to have fiducial corrected MIR flux densities, we impose the following criterion. If a galaxy has a corrected flux density lower than 2σ at 8 or $12\,\mu m$, then this galaxy is removed from the sample. At longer wavelengths, the contribution from the stellar populations to the IR emission is considered negligible.

Of the 322 HRS galaxies, 270 fulfill this criterion. However, from these 270 galaxies, we remove five that were not detected in PACS and SPIRE bands, thus having no constraints on the FIR and submm part of the SED: HRS 90, HRS 155, HRS 240, HRS 291, and HRS 316. We run our fitting procedure

Table B.1. Stellar contribution in NIR and MIR bands for early-type galaxies (ETG) and late-type galaxies (LTG).

	Band	λ (μm)	Normalisation			
			to 1.2 μm (J)	to 1.6 μm (H)	to 2.2 μm (K)	to 3.6 μm (IRAC 1)
ETG	J	1.2	1.	–	–	–
	H	1.6	$1.177^{+0.003}_{-0.004}$	1.	–	-
	K	2.2	$0.858^{+0.002}_{-0.005}$	$0.728^{+0.0}_{-0.007}$	1.	–
	IRAC1	3.6	$0.414^{+0.007}_{-0.036}$	$0.352^{+0.005}_{-0.029}$	$0.483^{+0.007}_{-0.044}$	1.
	IRAC2	4.5	$0.247^{+0.005}_{-0.023}$	$0.210^{+0.004}_{-0.018}$	$0.288^{+0.005}_{-0.028}$	$0.596^{+0.002}_{-0.004}$
	IRAC3	5.8	$0.167^{+0.004}_{-0.016}$	$0.142^{+0.003}_{-0.013}$	$0.194^{+0.004}_{-0.019}$	$0.402^{+0.001}_{-0.003}$
	IRAC4	8	$0.103^{+0.002}_{-0.010}$	$0.088^{+0.002}_{-0.008}$	$0.120^{+0.002}_{-0.012}$	$0.249^{+0.001}_{-0.002}$
	WISE3	12	$0.083^{+0.002}_{-0.008}$	$0.071^{+0.001}_{-0.006}$	$0.097^{+0.002}_{-0.010}$	$0.201^{+0.001}_{-0.002}$
	WISE4	22	$0.018^{+0.0004}_{-0.002}$	$0.015^{+0.0003}_{-0.001}$	$0.021^{+0.0004}_{-0.002}$	$0.044^{+0.0002}_{-0.001}$
	MIPS1	24	$0.019^{+0.0004}_{-0.002}$	$0.016^{+0.0003}_{-0.002}$	$0.022^{+0.0005}_{-0.002}$	$0.046^{+0.0002}_{-0.001}$
	IRAS	60	$0.004^{+0.0001}_{-0.0004}$	$0.003^{+0.0001}_{-0.0003}$	$0.004^{+0.0001}_{-0.0005}$	$0.009^{+0.00006}_{-0.0001}$
LTG	J	1.2	1.	–	–	–
	H	1.6	$1.171^{+0.001}_{-0.001}$	1.	–	–
	K	2.2	$0.875^{+0.009}_{-0.005}$	$0.747^{+0.008}_{-0.004}$	1.	–
	IRAC1	3.6	$0.333^{+0.032}_{-0.016}$	$0.284^{+0.027}_{-0.014}$	$0.380^{+0.041}_{-0.020}$	1.
	IRAC2	4.5	$0.196^{+0.020}_{-0.010}$	$0.167^{+0.017}_{-0.008}$	$0.224^{+0.025}_{-0.012}$	$0.589^{+0.002}_{-0.001}$
	IRAC3	5.8	$0.132^{+0.013}_{-0.007}$	$0.113^{+0.011}_{-0.006}$	$0.151^{+0.017}_{-0.008}$	$0.396^{+0.002}_{-0.001}$
	IRAC4	8	$0.081^{+0.008}_{-0.004}$	$0.070^{+0.007}_{-0.004}$	$0.093^{+0.011}_{-0.005}$	$0.244^{+0.002}_{-0.001}$
	WISE3	12	$0.066^{+0.007}_{-0.003}$	$0.056^{+0.006}_{-0.003}$	$0.075^{+0.009}_{-0.004}$	$0.197^{+0.002}_{-0.001}$
	WISE4	22	$0.014^{+0.002}_{-0.001}$	$0.012^{+0.001}_{-0.001}$	$0.016^{+0.002}_{-0.001}$	$0.043^{+0.001}_{-0.0003}$
	MIPS1	24	$0.015^{+0.002}_{-0.001}$	$0.013^{+0.001}_{-0.001}$	$0.017^{+0.002}_{-0.001}$	$0.044^{+0.0005}_{-0.0003}$
	IRAS	60	$0.003^{+0.0003}_{-0.0002}$	$0.002^{+0.0003}_{-0.0001}$	$0.003^{+0.0004}_{-0.0002}$	$0.009^{+0.0001}_{-0.00006}$

on 265 galaxies: 20 early-type galaxies and 245 late-type galaxies.

We present the results from the fits of the galaxies not analyzed in this work (20 early-type galaxies and 99 H I-deficient galaxies) in Table C.1.

Appendix D: Comparison between the properties of the gas-rich galaxies and the output of DL07 models

While we describe the main results of the comparison between the output parameters of DL07 and the properties of the gas-rich galaxy sample in Sect. 5, we describe here, for each output parameters, the relations with these properties. These relations are presented in Fig. D.1. The Spearman coefficient is provided for every relation. With a number of objects larger than 100, a

correlation is expected to be real with a Spearman correlation coefficient larger than 0.40.

D.1. PAH emission

The fraction of PAH correlates with all of the parameters, except the birthrate parameter, with ρ ranging from 0.45 to 0.73. The relation between the fraction of PAH, the metallicity, and the stellar mass is described in Sect. 5.

There is a weak relation between the fraction of PAH contributing to the total IR luminosity and the SFR ($\rho = 0.45$). We would expect a tighter correlation as PAHs are often used as SFR indicators although many caveats on this assumption have been discussed in the literature (Boselli et al. 2004; Wu et al. 2005; Calzetti et al. 2007; Zhu et al. 2008; Kennicutt et al. 2009). Indeed, the destruction of PAH in regions where the ISRF is too intense, such as PDRs, can affect the relation between the SFR and 8 μm luminosity. This leads to a weak

Table C.1. Estimated parameters.

HRS	CGCG	VCC	UGC	NGC	IC	Type	U_{min}	q_{PAH} (%)	γ (%)	$\log(L_{IR}/L_\odot)$	$\log(M_{dust}/M_\odot)$
1	123035	–	–	–	–	pec	2.23 ± 0.83	4.14 ± 0.61	0.66 ± 0.67	8.48 ± 0.04	6.01 ± 0.12
3	94026	–	5617	3226	–	E	2.38 ± 0.41	4.46 ± 0.27	0.18 ± 0.09	8.49 ± 0.02	6.02 ± 0.06
4	94028	–	5620	3227	–	Sa	2.18 ± 0.40	4.58 ± 0.02	5.60 ± 1.06	10.03 ± 0.01	7.37 ± 0.05
5	94052	–	–	–	610	Sc	2.64 ± 0.41	4.05 ± 0.42	0.37 ± 0.29	9.23 ± 0.03	6.67 ± 0.05
6	154016	–	5662	3245	–	Sb	0.27 ± 0.24	3.02 ± 1.27	1.10 ± 0.80	8.24 ± 0.07	6.80 ± 0.22
7	154017	–	5663	3245	–	S0	7.41 ± 1.29	1.55 ± 0.50	2.79 ± 0.76	9.29 ± 0.04	6.22 ± 0.04
9	154026	–	5731	3277	–	Sab	2.51 ± 0.85	4.40 ± 0.34	0.82 ± 0.87	9.12 ± 0.03	6.58 ± 0.10
14	124045	–	5767	3301	–	S0/Sa	7.21 ± 5.67	3.08 ± 1.07	4.93 ± 10.04	8.52 ± 0.06	5.50 ± 0.28
18	155015	–	5906	3380	–	Sa	2.43 ± 0.73	4.44 ± 0.29	0.70 ± 0.64	9.14 ± 0.03	6.60 ± 0.09
21	155028	–	5958	–	–	Sbc	0.94 ± 0.65	3.69 ± 0.78	0.45 ± 0.49	8.35 ± 0.09	6.34 ± 0.19
32	95065	–	6030	3457	–	Sb	0.25 ± 0.19	3.41 ± 1.16	7.21 ± 8.87	7.72 ± 0.10	6.02 ± 0.21
35	267037	–	6115	3499	–	pec	6.43 ± 2.38	4.52 ± 0.19	0.24 ± 0.15	8.42 ± 0.03	5.54 ± 0.15
36	155049	–	6118	3504	–	Sab	6.22 ± 1.45	3.54 ± 0.39	5.25 ± 1.36	10.46 ± 0.03	7.39 ± 0.05
45	291054	–	6330	3619	–	S0	1.12 ± 0.34	4.25 ± 0.51	0.53 ± 0.54	9.12 ± 0.04	6.94 ± 0.10
46	96029	–	6343	3626	–	S0	5.34 ± 1.21	4.00 ± 0.44	0.64 ± 0.45	9.50 ± 0.03	6.65 ± 0.05
57	96049	–	6460	3686	–	Sbc	2.36 ± 0.36	4.58 ± 0.04	0.73 ± 0.33	9.78 ± 0.02	7.25 ± 0.05
58	96050	–	6464	3691	–	Sb	2.15 ± 0.51	4.16 ± 0.51	0.52 ± 0.48	8.83 ± 0.04	6.36 ± 0.07
71	292042	–	6860	3945	–	S0	0.70 ± 1.93	3.26 ± 1.10	2.69 ± 5.56	8.89 ± 0.09	7.12 ± 0.52
80	69027	–	7002	4037	–	Sb	0.62 ± 0.38	3.86 ± 0.80	2.99 ± 3.88	8.72 ± 0.04	6.97 ± 0.19
82	98037	–	–	–	–	Sab	4.05 ± 1.15	4.46 ± 0.26	0.45 ± 0.29	8.61 ± 0.03	6.12 ± 0.10
83	41031	–	7035	–	–	Sa	1.67 ± 1.33	2.42 ± 1.25	3.77 ± 6.26	8.42 ± 0.08	6.05 ± 0.24
87	69058	–	7117	4119	–	S0	2.26 ± 0.92	3.92 ± 0.59	0.62 ± 0.63	8.79 ± 0.04	6.25 ± 0.15
93	187029	–	7256	4203	–	S0	1.69 ± 0.63	4.08 ± 0.56	0.52 ± 0.37	8.96 ± 0.03	6.46 ± 0.15
97	69112	167	7284	4216	–	Sb	0.80 ± 0.12	4.57 ± 0.10	0.38 ± 0.27	9.97 ± 0.02	7.87 ± 0.05
99	69123	213	7305	–	3094	Sb	2.93 ± 0.62	4.56 ± 0.12	1.23 ± 0.73	8.76 ± 0.02	6.05 ± 0.06
100	98130	226	7315	4237	–	Sbc	2.77 ± 0.25	4.57 ± 0.07	0.21 ± 0.10	9.72 ± 0.01	7.08 ± 0.03
103	42015	341	7361	4260	–	Sa	1.01 ± 0.26	3.42 ± 0.97	0.47 ± 0.35	8.84 ± 0.03	6.65 ± 0.09
106	42032	393	7385	4276	–	Sc	1.31 ± 0.65	3.76 ± 0.92	1.13 ± 1.71	9.17 ± 0.05	6.85 ± 0.16
108	42037	434	–	4287	–	Sc	3.24 ± 1.65	3.82 ± 0.68	0.61 ± 0.63	8.95 ± 0.07	6.29 ± 0.13
112	42044	492	7413	4300	–	Sa	2.00 ± 0.84	2.48 ± 1.29	0.73 ± 0.80	8.85 ± 0.07	6.39 ± 0.12
113	99027	497	7418	4302	–	Sc	1.21 ± 0.08	4.57 ± 0.07	0.17 ± 0.07	9.96 ± 0.01	7.72 ± 0.02
115	42047	517	7422	–	–	Sab	1.99 ± 0.95	2.80 ± 1.26	2.69 ± 2.89	8.71 ± 0.05	6.12 ± 0.12
117	70029	524	7431	4307	–	Sb	1.15 ± 0.18	4.47 ± 0.26	0.32 ± 0.25	9.61 ± 0.02	7.37 ± 0.05
119	99029	559	7442	4312	–	Sab	3.01 ± 0.55	4.58 ± 0.00	0.35 ± 0.19	9.55 ± 0.01	6.88 ± 0.08
120	70034	570	7445	4313	–	Sab	1.28 ± 0.24	4.53 ± 0.19	0.45 ± 0.26	9.34 ± 0.02	7.03 ± 0.07
123	42063	613	7451	4324	–	S0	1.02 ± 0.31	3.91 ± 0.76	0.58 ± 0.59	8.94 ± 0.04	6.75 ± 0.10
124	70039	630	7456	4330	–	Scd	0.88 ± 0.20	4.34 ± 0.41	0.37 ± 0.25	9.21 ± 0.03	7.07 ± 0.09
127	42070	656	7465	4343	–	Sb	1.70 ± 0.30	4.47 ± 0.26	0.36 ± 0.24	9.60 ± 0.03	7.18 ± 0.05
128	42072	667	7469	–	3259	Sdm−Sd/S	0.71 ± 0.25	4.05 ± 0.67	1.06 ± 1.12	8.89 ± 0.04	6.84 ± 0.11
129	99038	685	7473	4350	–	S0	7.60 ± 1.67	3.66 ± 0.89	0.42 ± 0.34	8.61 ± 0.04	5.55 ± 0.06
130	70045	692	7476	4351	–	Sab	1.72 ± 0.50	4.09 ± 0.59	0.37 ± 0.26	8.98 ± 0.03	6.57 ± 0.10
131	42079	697	7474	–	3267	Scd	0.96 ± 0.63	2.73 ± 1.36	6.03 ± 10.39	8.97 ± 0.08	6.65 ± 0.17
134	70048	713	7482	4356	–	Sc	1.09 ± 0.31	3.63 ± 0.67	2.45 ± 0.79	9.17 ± 0.03	6.84 ± 0.10
136	42089	758	7492	4370	–	Sa	2.21 ± 0.35	2.95 ± 0.41	0.16 ± 0.07	9.33 ± 0.02	6.83 ± 0.05
141	70061	792	7503	4380	–	Sb	0.74 ± 0.13	4.45 ± 0.29	0.33 ± 0.20	9.56 ± 0.02	7.49 ± 0.08
144	70068	836	7520	4388	–	Sb	2.73 ± 0.74	3.97 ± 0.43	11.23 ± 3.09	10.12 ± 0.02	7.17 ± 0.06
147	42099	859	7522	–	–	Sd	0.69 ± 0.19	3.77 ± 0.94	0.59 ± 0.63	9.02 ± 0.05	7.02 ± 0.08
149	70071	873	7528	4402	–	Sb	2.38 ± 0.26	4.58 ± 0.04	0.33 ± 0.20	10.00 ± 0.02	7.43 ± 0.03
152	42104	921	7536	4412	–	Sb	4.63 ± 1.19	3.76 ± 0.51	2.82 ± 0.76	9.53 ± 0.02	6.59 ± 0.06
153	42105	938	7541	4416	–	Scd	1.71 ± 0.41	4.35 ± 0.41	0.44 ± 0.28	9.21 ± 0.03	6.78 ± 0.08
156	99054	958	7551	4419	–	Sa	3.05 ± 0.60	3.78 ± 0.42	4.01 ± 0.93	9.96 ± 0.02	7.14 ± 0.05
159	70090	979	7561	4424	–	Sa	4.90 ± 1.33	3.56 ± 0.43	2.01 ± 0.61	9.76 ± 0.03	6.82 ± 0.08
160	42111	1002	7566	4430	–	Sb	1.27 ± 0.34	3.66 ± 1.01	0.53 ± 0.50	9.60 ± 0.04	7.29 ± 0.08
161	70093	1003	7568	4429	–	S0	3.30 ± 0.53	3.34 ± 0.56	1.27 ± 0.48	9.16 ± 0.03	6.42 ± 0.04
162	70098	1030	7575	4435	–	S0	4.83 ± 1.89	1.45 ± 0.43	0.79 ± 0.33	9.26 ± 0.03	6.39 ± 0.13
167	70104	1086	7587	4445	–	Sab	1.04 ± 0.19	4.16 ± 0.58	0.26 ± 0.17	9.05 ± 0.02	6.83 ± 0.07
170	99062	1110	7594	4450	–	Sab	0.96 ± 0.30	4.16 ± 0.50	0.25 ± 0.17	9.54 ± 0.03	7.38 ± 0.14
171	70111	1118	7600	4451	–	Sbc	4.29 ± 0.60	4.55 ± 0.14	0.38 ± 0.22	9.60 ± 0.02	6.79 ± 0.05
172	99065	1126	7602	–	3392	Sb	2.37 ± 0.42	4.58 ± 0.05	0.32 ± 0.19	9.28 ± 0.02	6.71 ± 0.08
173	42124	1145	7609	4457	–	Sb	4.35 ± 0.67	4.48 ± 0.24	0.68 ± 0.36	9.70 ± 0.02	6.85 ± 0.05
174	70116	1154	7614	4459	–	S0	7.68 ± 0.75	4.26 ± 0.41	0.24 ± 0.15	9.27 ± 0.02	6.23 ± 0.03
176	70121	1190	7622	4469	–	S0/Sa	2.16 ± 0.43	3.08 ± 1.06	0.43 ± 0.29	9.38 ± 0.03	6.89 ± 0.06
184	70140	1326	7657	4491	–	Sa	9.64 ± 4.40	0.85 ± 0.45	7.04 ± 2.25	9.23 ± 0.03	5.90 ± 0.15
185	42141	1330	7656	4492	–	Sa	0.57 ± 0.17	4.28 ± 0.45	0.78 ± 0.43	8.71 ± 0.03	6.75 ± 0.11
189	99077	1393	7676	–	797	Sc	2.06 ± 0.46	4.42 ± 0.31	0.42 ± 0.26	9.03 ± 0.03	6.52 ± 0.07

Table C.1. continued.

HRS	CGCG	VCC	UGC	NGC	IC	Type	U_{min}	q_{PAH} (%)	γ (%)	$\log(L_{IR}/L_\odot)$	$\log(M_{dust}/M_\odot)$
190	99076	1401	7675	4501	–	Sb	2.16 ± 0.25	4.58 ± 0.01	0.30 ± 0.14	10.58 ± 0.01	8.08 ± 0.03
191	99078	1410	7677	4502	–	Scd	1.31 ± 1.06	2.12 ± 1.19	5.65 ± 10.15	8.43 ± 0.06	6.06 ± 0.25
192	70152	1419	7682	4506	–	Sa	2.39 ± 0.81	3.05 ± 1.22	0.41 ± 0.34	8.30 ± 0.03	5.78 ± 0.13
193	70157	1450	7695	–	3476	Im(Im/S)	1.77 ± 0.62	4.15 ± 0.43	1.41 ± 0.59	9.21 ± 0.04	6.74 ± 0.10
197	70168	1516	7711	4522	–	Scd	1.69 ± 0.36	4.38 ± 0.35	0.48 ± 0.30	9.33 ± 0.03	6.92 ± 0.06
199	99090	1532	7716	–	800	Sc	2.15 ± 1.03	3.81 ± 0.88	0.51 ± 0.40	8.77 ± 0.04	6.25 ± 0.18
200	42155	1535	7718	4526	–	S0	3.92 ± 0.32	2.49 ± 0.11	0.19 ± 0.09	9.81 ± 0.02	7.02 ± 0.02
204	42159	1555	7727	4535	–	Sc	1.25 ± 0.22	4.54 ± 0.16	1.26 ± 0.40	10.32 ± 0.02	7.99 ± 0.06
206	42162	1575	7736	–	3521	Sm/BCD	2.35 ± 1.07	3.26 ± 1.01	2.00 ± 2.07	9.11 ± 0.05	6.48 ± 0.12
207	99093	1588	7742	4540	–	Scd	2.04 ± 0.36	4.50 ± 0.22	0.32 ± 0.23	9.42 ± 0.03	6.94 ± 0.05
208	99096	1615	7753	4548	–	Sb	0.80 ± 0.19	4.37 ± 0.39	0.38 ± 0.26	9.80 ± 0.03	7.72 ± 0.11
215	70189	1673	7777	4567	–	Sbc	3.99 ± 0.08	4.58 ± 0.00	0.19 ± 0.08	9.95 ± 0.00	7.18 ± 0.00
216	70188	1676	7776	4568	–	Sbc	4.99 ± 0.10	3.90 ± 0.05	0.13 ± 0.04	10.45 ± 0.01	7.60 ± 0.03
217	70192	1690	7786	4569	–	Sab	1.98 ± 0.38	4.57 ± 0.07	1.46 ± 0.45	10.21 ± 0.02	7.67 ± 0.07
220	70197	1727	7796	4579	–	Sb	1.32 ± 0.31	4.49 ± 0.24	0.36 ± 0.23	10.08 ± 0.02	7.76 ± 0.10
221	42183	1730	7794	4580	–	Sa	1.53 ± 0.23	4.44 ± 0.27	0.29 ± 0.16	9.36 ± 0.02	6.98 ± 0.04
222	70199	1757	7803	4584	–	Sa	0.78 ± 0.51	2.57 ± 0.89	15.16 ± 12.24	8.59 ± 0.04	6.24 ± 0.21
223	42186	1758	7802	–	–	Sdm−Sd/S	0.50 ± 0.44	2.48 ± 1.38	4.80 ± 7.01	8.30 ± 0.12	6.41 ± 0.20
224	42187	1760	7804	4586	–	Sa	0.87 ± 0.28	4.24 ± 0.42	0.47 ± 0.52	8.96 ± 0.03	6.83 ± 0.13
226	42191	1780	7821	4591	–	Sb	1.89 ± 0.50	4.41 ± 0.30	0.48 ± 0.37	8.96 ± 0.03	6.48 ± 0.08
230	99106	1811	7826	4595	–	Sb	2.21 ± 0.48	4.46 ± 0.27	0.35 ± 0.26	9.20 ± 0.03	6.68 ± 0.07
232	70213	1859	7839	4606	–	Sa	2.99 ± 0.69	4.52 ± 0.20	0.45 ± 0.27	9.09 ± 0.02	6.42 ± 0.09
233	70216	1868	7843	4607	–	Sb	2.43 ± 0.46	4.29 ± 0.35	0.45 ± 0.28	9.58 ± 0.03	6.99 ± 0.07
239	99112	1932	7875	4634	–	Scd	3.42 ± 0.57	4.45 ± 0.26	0.25 ± 0.12	9.74 ± 0.03	7.04 ± 0.04
243	15008	–	7895	4643	–	S0/Sa	0.47 ± 0.25	3.47 ± 1.12	1.83 ± 2.24	9.08 ± 0.05	7.21 ± 0.14
244	71015	1972	7896	4647	–	Sc	3.76 ± 0.43	4.58 ± 0.00	0.35 ± 0.23	10.03 ± 0.02	7.25 ± 0.03
253	15019	–	7951	4684	–	S0	16.48 ± 5.61	0.91 ± 0.51	8.46 ± 3.68	9.30 ± 0.03	5.71 ± 0.07
254	71043	2058	7965	4689	–	Sbc	1.40 ± 0.33	4.57 ± 0.07	0.50 ± 0.29	9.84 ± 0.02	7.48 ± 0.10
256	15023	–	–	4691	–	Sa	8.30 ± 1.57	3.11 ± 0.23	5.25 ± 0.76	10.03 ± 0.03	6.83 ± 0.04
260	100011	–	7980	4710	–	S0	3.15 ± 0.60	2.54 ± 0.31	1.34 ± 0.42	9.78 ± 0.03	7.06 ± 0.05
261	43040	–	7982	–	–	Sd	0.50 ± 0.20	3.71 ± 0.99	0.71 ± 0.80	8.77 ± 0.04	6.97 ± 0.13
264	15027	–	7991	–	–	Sd	0.39 ± 0.25	2.06 ± 1.18	5.53 ± 5.66	8.55 ± 0.06	6.68 ± 0.15
265	–	–	–	4720	–	pec	3.60 ± 1.24	3.29 ± 0.81	0.87 ± 0.85	9.11 ± 0.05	6.42 ± 0.09
270	15029	–	8009	4753	–	pec	1.98 ± 0.60	4.23 ± 0.48	0.42 ± 0.42	9.57 ± 0.04	7.16 ± 0.10
273	15031	–	8020	4771	–	Sd	0.86 ± 0.26	4.32 ± 0.45	0.81 ± 0.80	9.36 ± 0.04	7.22 ± 0.09
276	71068	–	8022	4779	–	Sbc	2.26 ± 0.77	4.19 ± 0.46	2.08 ± 1.30	9.36 ± 0.03	6.74 ± 0.10
277	43060	–	–	4791	–	BCD	2.56 ± 3.05	2.55 ± 1.38	8.47 ± 16.35	8.94 ± 0.11	5.71 ± 0.29
278	71071	–	8032	–	–	Sb	1.54 ± 0.84	3.96 ± 0.64	0.37 ± 0.35	8.61 ± 0.07	6.33 ± 0.15
280	43066	–	8043	4799	–	Sb	3.07 ± 0.61	4.50 ± 0.23	0.57 ± 0.41	9.23 ± 0.03	6.55 ± 0.05
285	15049	–	8078	4845	–	Sab	2.86 ± 0.47	3.19 ± 0.33	0.48 ± 0.26	10.00 ± 0.03	7.34 ± 0.04
286	71092	–	8102	4866	–	S0	0.61 ± 0.91	2.32 ± 1.32	3.44 ± 5.03	8.68 ± 0.09	6.81 ± 0.28
288	–	–	–	4941	–	Sab	0.65 ± 0.19	4.40 ± 0.35	4.38 ± 1.32	9.38 ± 0.02	7.28 ± 0.08
294	246017	–	8593	–	902	Sb	1.75 ± 0.48	4.41 ± 0.31	0.57 ± 0.48	9.36 ± 0.03	6.96 ± 0.07
296	190041	–	8675	5273	–	S0	5.45 ± 3.30	3.36 ± 0.76	6.64 ± 6.50	8.67 ± 0.04	5.67 ± 0.19
300	218058	–	8756	–	–	Sab	1.76 ± 1.03	4.07 ± 0.60	1.00 ± 1.28	8.62 ± 0.04	6.24 ± 0.19
303	295024	–	8843	5372	–	Sb	9.81 ± 2.14	4.44 ± 0.28	1.07 ± 0.53	9.65 ± 0.03	6.50 ± 0.07
304	46001	–	8831	5356	–	Sbc	0.97 ± 0.18	4.57 ± 0.09	0.47 ± 0.34	9.32 ± 0.02	7.18 ± 0.05
305	46003	–	8838	5360	958	pec	0.97 ± 1.26	2.61 ± 1.37	15.75 ± 22.02	8.29 ± 0.08	6.08 ± 0.29
306	46007	–	8847	5363	–	pec	2.48 ± 0.76	4.38 ± 0.36	0.26 ± 0.17	9.22 ± 0.03	6.73 ± 0.13
307	46009	–	8853	5364	–	Sbc	0.63 ± 0.20	4.55 ± 0.13	1.61 ± 1.14	9.90 ± 0.03	7.92 ± 0.09
308	46011	–	8857	–	–	Sb	1.00 ± 0.67	2.82 ± 1.34	8.38 ± 15.99	7.66 ± 0.12	5.38 ± 0.17
310	47010	–	9172	5560	–	Sb	2.50 ± 0.69	4.47 ± 0.26	1.28 ± 0.85	9.67 ± 0.02	7.09 ± 0.09
311	47012	–	9175	5566	–	Sab	0.64 ± 0.22	4.45 ± 0.29	1.28 ± 1.31	9.69 ± 0.03	7.70 ± 0.10
313	47022	–	9187	5577	–	Sbc	0.82 ± 0.18	4.47 ± 0.27	0.32 ± 0.21	9.28 ± 0.04	7.24 ± 0.08

anticorrelation with the birthrate parameter as well, and a moderate relation with the Hα surface brightness that directly probes star formation. It seems that galaxies experiencing a star formation episode, i.e., with higher b, have lower q_{PAH}. Indeed, previous works found that the PAH emission is inhibited within star-forming regions relative to other star formation tracers (e.g., Helou et al. 2004; Calzetti et al. 2005; Bendo et al. 2006, 2008; Pérez-González et al. 2006; Gordon et al. 2008). Another relation is found between q_{PAH} and the *H*-band surface brightness, linked to what was previously noticed by Calzetti et al. (2007) and Bendo et al. (2008) who showed that 8 µm emission is also contributed by dust heated by the diffuse nonionizing stellar component. A correlation is also found between the fraction of PAH and the FUV attenuation ($\rho = 0.58$). However, the trend seen on the related panel is difficult to interpret, as the relation, if real, appears to be nonlinear.
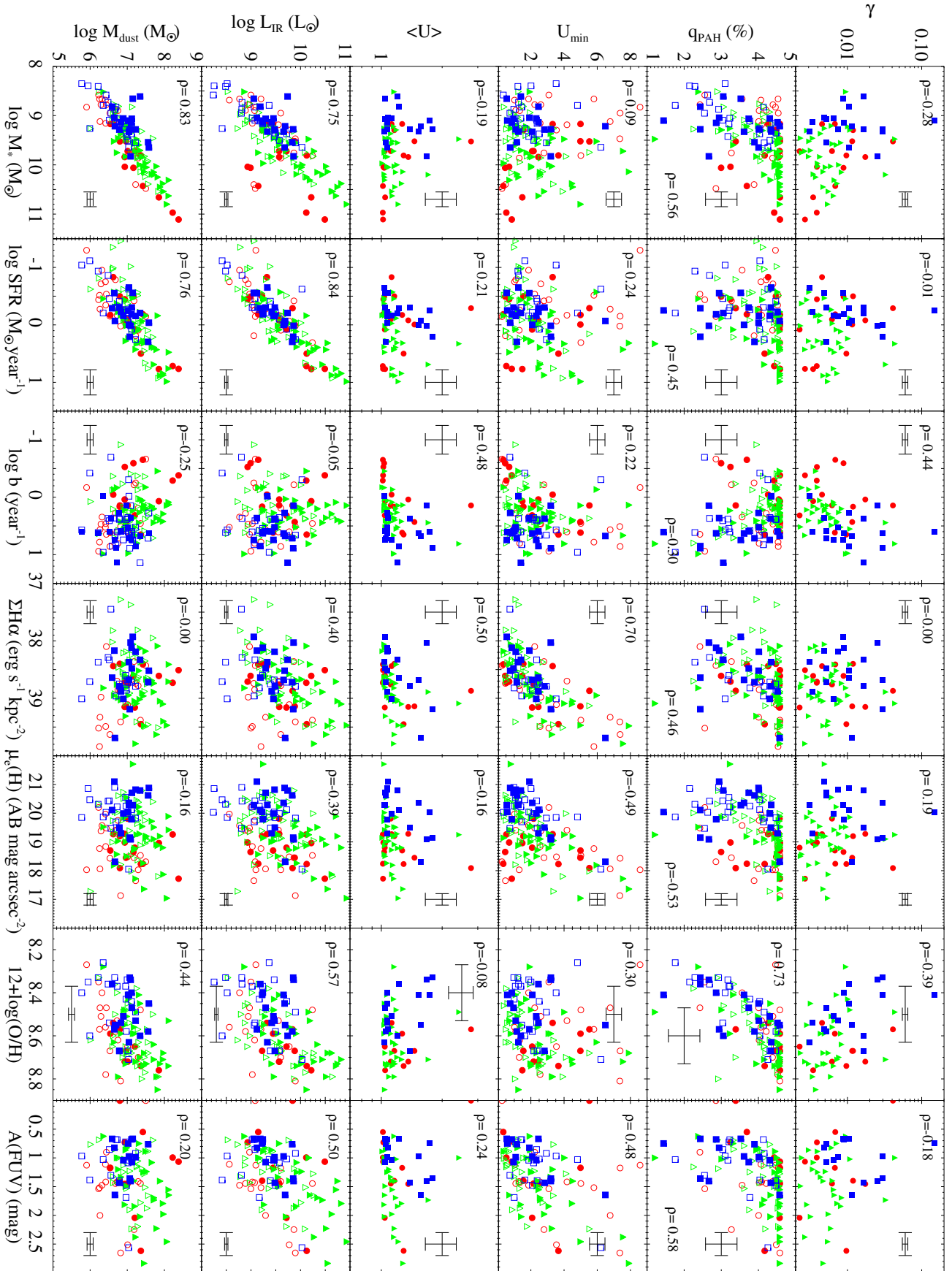
Fig. D.1. Comparison between the output parameters of the Draine & Li (2007) models and different physical variables. Galaxies are color-coded according their morphological type. In red: the Sa, Sab, Sb; in green: the Sbc, Sc, Scd, and in blue: the Sd, Im and BCD. The Spearman correlation coefficient of each relation is provided. Galaxies with a 24 μm measurement are represented by filled symbols, galaxies with 22 μm with empty symbols.

D.2. Relative contribution of PDR and diffuse regions

Here we only consider galaxies for which MIPS 24 μm measurements are available (filled symbols on Fig. D.1) to have the strongest constraint on γ (see Sect. 4.3). There is a moderate relation between γ and the birthrate parameter ($\rho = 0.44$). When γ increases, the contribution of the PDR to the emission of the IR SED increases. As b is linked to the hardness of the UV radiation field, both quantities are correlated. Although weak, these relations between γ and b, and γ and the metallicity are consistent as the most metal poor objects are also the most star forming. We also notice a trend between γ and the metallicity, with a Spearman correlation coefficient of $\rho = -0.39$. The PDR contribution to the IR SED increases when the metallicity decreases. This confirms the tendency between γ and the stellar mass already noticed from the shape of the IR SED in Fig. 4. Furthermore, when γ increases, the IR peaks widen (Fig. 4). These two points confirm the results of Smith et al. (2012a) who performed a panchromatic analysis of the SED of a 250 μm selected sample of galaxies and found that low-mass galaxies have broader IR peaks. This relation also implies that the IR SED of the most massive galaxies is dominated by the emission of the diffuse component.

D.3. Interstellar radiation field

The ISRF is characterized by the parameters $U_{\min}$, which quantifies the ISRF of the diffuse stellar component, and $\langle U \rangle$, the dust heating rate parameter, which is calculated from $U_{\min}$, γ, and $U_{\max}$ (fixed to 10^6). Relations between $\langle U \rangle$ and the integrated properties of the galaxies are thus linked to the relations between $U_{\min}$, γ, and these properties.

The relation between the intensity of the diffuse ISRF and the Hα and H-band surface brightnesses are discussed in Sect. 5. A weak correlation is observed between the birthrate parameter b and $\langle U \rangle$, with $\rho = 0.48$. The dust heating parameter $\langle U \rangle$ provides a direct measurement of the mean interstellar radiation field of the galaxy. This confirms the results of Boselli et al. (2010b) and Boselli et al. (2012) who found a correlation between b and the S_{60}/S_{100} flux density ratio, sensitive to the dust temperature.

D.4. Infrared luminosity

An expected trend is seen between the $L_{\rm IR}$ and M_* as the most massive galaxies are also the most luminous as a scale effect (Kennicutt 1990). We recover the strong relation between the $L_{\rm IR}$ and the SFR as well (Devereux & Young 1990; Devereux et al. 1995; Buat & Xu 1996; Kennicutt et al. 2009). Indeed, the $L_{\rm IR}$ is widely used as a proxy for the SFR (e.g., Scoville & Young 1983; Buat & Xu 1996; Kennicutt 1998; Kennicutt et al. 2009; Kennicutt & Evans 2012).

We observe a moderate relation between the $L_{\rm IR}$ and the metallicity ($\rho = 0.58$). Finally, there is also a moderate trend between the $L_{\rm IR}$ and the FUV attenuation ($\rho = 0.50$). The energy absorbed in UV is reemitted by the dust in IR, one would expect to find a tighter relation between these two properties. Indeed, Smith et al. (2012a) found that the FIR/optical ratio increases with the $L_{\rm IR}$ indicating that the galaxies with the higher IR luminosities are also the most obscured. However, by definition, A(FUV) is the infrared to UV luminosity ratio. These two quantities are thus not independent.

D.5. Dust mass

As expected, the dust mass and the stellar mass are tightly linked with a Spearman correlation coefficient of 0.83, as a scaling effect. There is also a strong correlation between the dust mass and the SFR. A weak global trend appears with the metallicity ($\rho = 0.44$). Indeed, the dust mass is larger in the most massive galaxies that are also the most metal-rich (Tremonti et al. 2004).

From Fig. D.1, we conclude that all of the integrated properties, except the FUV attenuation, correlate moderately to strongly with at least one of the output of Draine & Li (2007) models: the stellar mass to the fraction of PAH, the SFR to the fraction of PAH, the birthrate parameter moderately with γ and $\langle U \rangle$, ΣHα and $\mu_{\rm e}$(H) with $U_{\min}$ and $q_{\rm PAH}$, and the metallicity with $q_{\rm PAH}$ and moderately with γ. All of these properties drive the shape of the IR SED. We confirm the results of Boselli et al. (2012) who found that the metallicity, the intensity of the ionizing and nonionizing radiation field, and the birthrate parameter are key parameters in the dust emission observed in the FIR.